4-9-2024

All-Optical Probes of Particle-Like Charge Migration Dynamics

Kyle A. Hamer
Louisiana State University

ALL-OPTICAL PROBES OF PARTICLE-LIKE CHARGE MIGRATION DYNAMICS

A Dissertation

Submitted to the Graduate Faculty of the
Louisiana State University and
Agricultural and Mechanical College
in partial fulfillment of the
requirements for the degree of
Doctor of Philosophy

in

The Department of Physics and Astronomy

by
Kyle Alexander Hamer
B.S., Louisiana State University, 2019
May 2024

Acknowledgments

This work was supported by the U.S. Department of Energy, Office of Science, Office of Basic Energy Sciences, under Award No. DE-SC0012462. Portions of this research were conducted with high performance computational resources provided by Louisiana State University (`http://www.hpc.lsu.edu`) and the Louisiana Optical Network Infrastructure (`http://www.loni.org`).

First, I would like to thank my advisors: François Mauger, Mette Gaarde, and Kenneth Schafer, for eight years' worth of patience, compassion, knowledge, and guidance, as I navigated my way through my undergraduate and graduate education at LSU. With their expertise, my passion for science was crystallized into the work I proudly show here.

I would also like to thank my colleagues, from both the physics and chemistry departments at LSU, of which there have been many over the years, including Austin, Chris, Imam, Jason, Jens, Kalyani, Ken L., Lun, Manik, Marie, Nils, Paul, Seth, Simi, Steph, and Sucharita. All of them have had a part to play in making my time at LSU a more enjoyable endeavor, and on bringing a fresh perspective to this work. In addition, I thank my experimental collaborators, led by Lou DiMauro at The Ohio State University and Bob Jones at the University of Virginia, who also provided valuable feedback on this work.

Lastly, I would like to thank my friends and family, who were of course instrumental in my success; in particular, my parents, who made sure that my passion for knowledge was nurtured from a young age, and gave me the tools and support I needed to face the many challenges along the way.

Table of Contents

Abstract

Particle-like charge migration (CM) is the coherent, back-and-forth motion of a positively-charged electron hole along the backbone of a molecule following a sudden ionization. CM in small molecules generally occurs on an Angstrom (10^{-10} m) spatial scale and an attosecond (10^{-18} s) timescale. I use time-dependent density-functional theory (TDDFT) to simulate CM modes in organic molecules, and to explore all-optical probes of this attosecond electron dynamics using high-harmonic spectroscopy (HHS). By leveraging my results from previous studies of two-center interferences in carbon dichalcogens, in which I separated the harmonic signal into contributions from individual Kohn-Sham orbitals, I first develop high-harmonic sideband spectroscopy (HHSS) as a robust, background-free, and all-optical probe of particle-like CM dynamics. The CM manifests in the high-order harmonic signal as a beat in the time domain and as sidebands in the frequency domain and over several laser cycles. By varying the driving laser wavelength, I am able to extract the characteristic frequency of the relevant CM mode. Then, by exploiting the inherent time-resolution of the high-harmonic generation process (the attochirp), I develop frequency-matched strobo-spectroscopy (FMSS). Here, I vary the delay between the initiation of the CM dynamics and a few-cycle laser pulse in order to track the location of the electron hole along the molecular backbone as a function of time.

Chapter 1. Introduction

In this chapter, I first introduce the field of attosecond physics (Sec. 1.1), which raises the possibility of investigating the dynamics of electrons on their natural timescale. I then discuss two such ultrafast processes, charge migration (Sec. 1.2) and high-harmonic generation (Sec. 1.3).

1.1. Attosecond Physics

On a microscopic scale, many disparate scientific fields, such as biology, chemistry, and physics, blur together, as they are all initially governed by the motion of electrons within atoms and molecules. The typical timescale for electronic motion is given by the period of an electron circling the first Bohr orbit divided by 2π; this is the atomic time unit, equal to about 2.4×10^{-17} seconds, or 24 attoseconds. The most common anecdote for the incredibly short timescales being studied here is that there are more attoseconds in one second than there are seconds in the age of the universe – having done the math, I am happy to report that ultrafast physicists will be able to continue using this fun fact until long after the Sun has died out.

Since the invention of the laser in the early 1960s, the need for higher spatial and temporal resolution has been persistent in the field of atomic physics. In Figure 1.1, I show the history of pulse duration and intensity of once-cutting-edge laser systems. Notably, there was a time, between the late 1980s and the early 2000s, when laser systems struggled to pass the so-called "femtosecond barrier". Despite this hurdle, studies of time-resolved chemical bond formation and dissociation performed using these technologies was crucial to our understanding of these processes [1], ultimately leading to the Nobel Prize

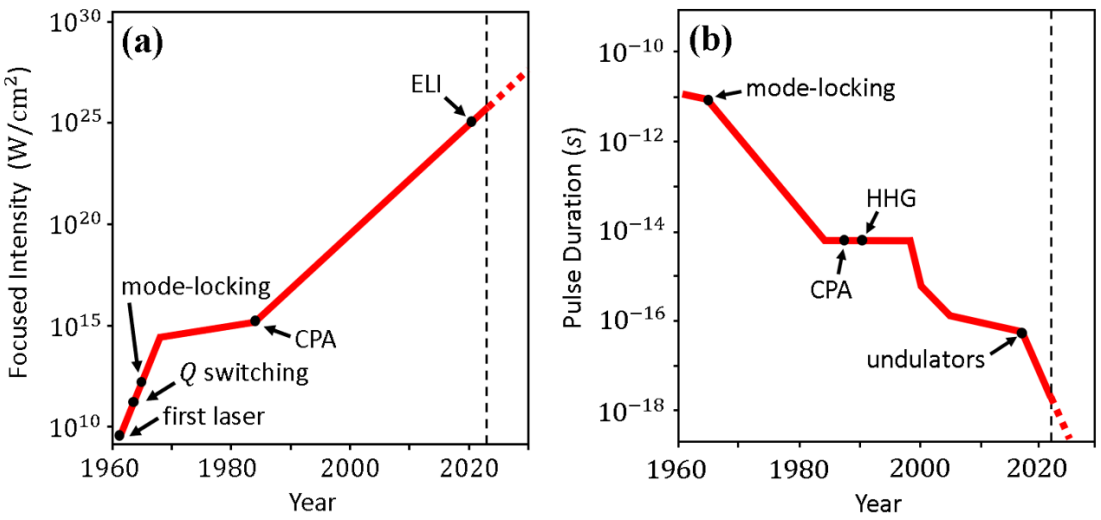

Figure 1.1: History of (a) laser pulse intensity, in W/cm^2, and (b) pulse duration [11], in seconds. Notable advancements in laser technology have been indicated.

in Chemistry for A. H. Zewail in 1999 [2]. Not long after, the discovery of high-order harmonic generation [3, 4] and its ability to create a train of coherent attosecond pulses [5, 6] ushered in the era of "attosecond physics" [1, 7–10], which aims to image, understand, and eventually control electronic motion in atoms and molecules.

In October 2023, three prominent members of the attosecond physics community – Pierre Agostini, Ferenc Krausz, and Anne L'Huillier – were awarded the Nobel Prize in physics "for experimental methods that generate attosecond pulses of light for the study of electron dynamics in matter" [12]. The Royal Swedish Academy of Sciences recognized the monumental amount of work that had been done since the early 1980s, and the myriad of potential applications of the control of ultrafast processes. To quote Nobel laureate Ferenc Krausz, "What are the most efficient ways of putting atoms into highly excited states that allow X-ray light amplification and thus creation of X-ray compact lasers? Can the function of biomolecules be manipulated and novel molecular structures be formed by steering electrons in chemical bonds? How does charge transfer occur in molecules assembled on

surfaces and how can it be optimized for more efficient solar cells or for fighting radiation damage during biological imaging? What are the ultimate size and speed limits of electronic information processing and magnetic information storage, and how can we approach these limits? How can energy be most efficiently transported into high-density matter to ignite nuclear fusion? Answers to these scientific and technological questions will require insight into and possibly control of microscopic electron motion." [7]

1.2. Molecular Movies of Charge Migration

The quest to make shorter and more intense laser pulses has long been the cornerstone of ultrafast physics – see again Fig. 1.1. Using these extremely short laser pulses, we are able to image electron dynamics on its natural timescale, in the range of tens of attoseconds. One example of this ultrafast dynamics, charge migration (CM), has attracted significant interest in the atomic, molecular, and optical (AMO) community [8, 9, 13–15]. This is in part because CM can be a precursor to many downstream processes such as chemical reactions, photosynthesis, and photovoltaics; therefore, it is a means of understanding and perhaps steering these processes with the goal of charge-directed reactivity [16–18]. Traditionally, CM is defined as "a time-dependent oscillation of the charge density in a molecule, which is driven by the electronic coherence of a superposition state" (taken from Ref. [15]). Throughout this report, however, I will use a more stringent definition: after a localized ionization in a molecule, CM is the subsequent motion of a positively-charged hole along the molecular backbone in a coherent, particle-like manner. This back-and-forth motion of the electron hole, with a well-defined CM frequency, is called a CM *mode* [18, 19].

Before the advent of CM, chemical reactivity was described by the Rice-Ramsperger-Kassel-Marcus (RRKM) theory [20–22], in which it is assumed that any excess energy is rapidly equipartitioned amongst all of the molecular degrees of freedom. Thus, according to RRKM theory, larger molecules with more degrees of freedom are much slower to dissociate, since there is a much lower probability that there will be a localized fluctuation in the electron density which would cause a bond to break [23]. However, in 1997, Weinkauf *et al.* [24] observed that ions of small and medium-sized peptides dissociated much faster than would be predicted by RRKM theory. Furthermore, they demonstrated that these peptides could dissociate at a site far away from the initial site-specific ionization, and attributed their observations to "charge migration along the peptide backbone, like a beaded chain" (taken from Ref. [24]).

The first theory of CM was formulated in 1999 by Cederbaum and Zobeley [25], in which they ascribe CM to the correlation between electrons, saying that "in the absence of electron correlation the hole stays in the orbital in which it has been initially created and does not migrate". In other words, if an electron is removed from the system is such a way that the remaining ion is in a stationary eigenstate of the cation, then there will be no CM. In this picture, the simplest CM motion is caused by a beating between two cationic eigenstates, producing an oscillating electron hole density with a characteristic frequency equal to the difference of the energies of the two states involved (see Refs. [26, 27]). However, analyzing CM as a beating of molecular orbitals quickly becomes extremely complicated when more than a few orbitals are involved [28–31]. Furthermore, molecular orbitals cannot be probed directly in an experiment; instead, experiments rely on various forms of spectroscopy to measure CM [32–34]. In this report, I will discuss a more intuitive way to

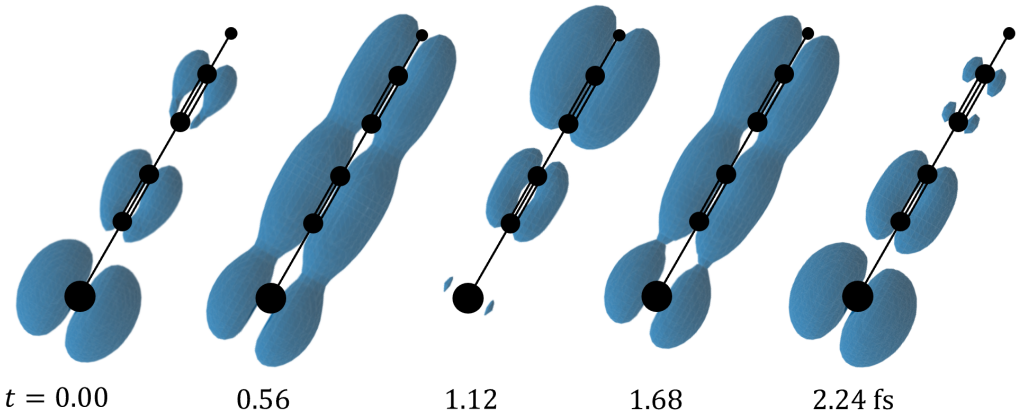

Figure 1.2: Ultrafast electron dynamics after the sudden removal of an electron from bromobutadiyne (BrC_4H).

look at the problem, involving only the one-body electron density [18, 19, 35], which is a physical and (in principle) measurable quantity.

Since its inception, the theory of CM has experienced a golden age [18, 23, 35–46]. In addition, there have been many combined experiment/theory efforts to explain CM in specific molecules, such as glycine [47–50], PENNA [51–54], and other biologically-relevant systems [33, 55–61]. Such a myriad of perspectives on the subject has fostered a vibrant ecosystem for studying CM, likely due to the many possible benefits of being able to understand and control this phenomenon.

1.3. High-Harmonic Generation

The interaction between light and matter is at the heart of AMO physics. As an example, high-harmonic generation (HHG) is a process in which the target matter responds to an intense laser field in an extremely nonlinear manner, emitting high-energy photons with frequencies which are multiples (harmonics) of the incident laser. Due to its inherent sub-femtosecond resolution, HHG has been developed over the past two decades as a powerful spectroscopic tool, used to probe both structural and dynamical features

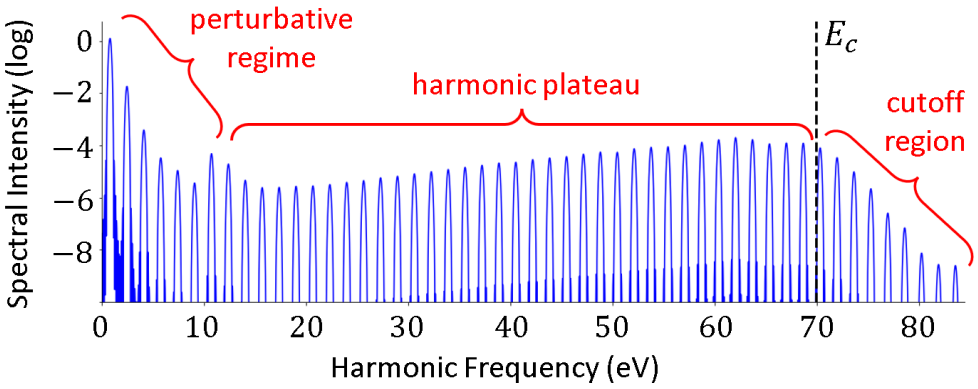

Figure 1.3: Example of a HHG spectrum, taken from a 1D atomic single-active-electron (SAE) calculation in Octopus, for $\lambda = 1500\,\text{nm}$ and $I_\circ = 75\,\text{TW/cm}^2$. The spectrum is divided into three regions: the perturbative regime, the harmonic plateau, and the cutoff region.

in atomic, molecular, and condensed-phase systems [8, 15, 62–64], including CM [34, 65–69]. HHG was first observed in 1987 simultaneously by Ferray *et al.* in Paris [3] and by McPherson *et al.* in Chicago [4], and over the next few years, theory made great strides towards explaining this phenomenon [70–75]. HHG has two important applications: in the early 2000s, it was discovered that HHG could generate coherent attosecond pulses [5, 76–80]. Second, HHG was also developed as a spectroscopic tool used to measure the structure and dynamics of matter, which will be the main focus here. Since then, HHG has been used to recover internuclear distances [81, 82] and perform molecular tomography [83–86], among many other applications [66, 87–91].

As a demonstration, I apply an intense laser field to a gas-phase target (in simulations, modeled by a single atom or molecule) in order to induce HHG. Consider a laser pulse, described mathematically by

$$\vec{E}(t) = E_\circ \sin^2\left(\frac{\pi t}{T_p}\right) \cdot \cos\left(\omega_L t\right) \hat{x}\ , \quad 0 \leq t \leq T_p \tag{1.1}$$

where ω_L is the driving laser frequency and T_p is the pulse width. Under these condi-

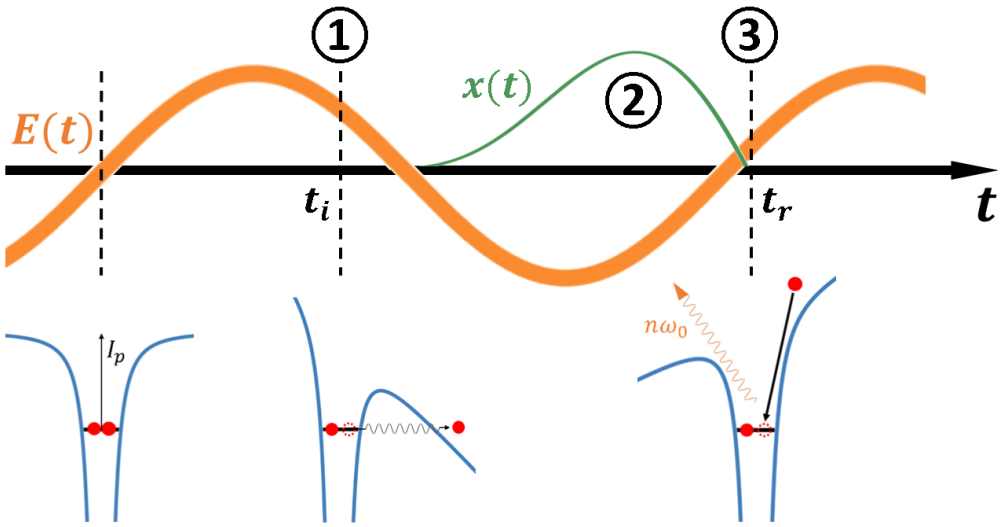

Figure 1.4: Schematic of the three-step model of high-order harmonic generation (HHG) in the gas phase. An electron is released into the continuum via tunnel ionization (1), accelerates under the influence of the laser field (2), until it recombines with its parent ion and emits a high-energy photon (3).

tion, a typical high-harmonic spectrum is shown in Figure 1.3, calculated from the Fourier transform of the time-dependent dipole moment induced in a one-dimensional atomic-like system by an intense laser pulse. Within the spectrum, there are dozens of peaks corresponding to the odd-integer harmonics $n\omega_L$ (odd $n \in \mathbb{Z}$) of the fundamental laser frequency ω_L. For a one-color laser field acting on an inversion-symmetric system, the even harmonic orders will be suppressed in the harmonic spectrum. Within the harmonic spectrum, there are three distinct regions: (1) the perturbative regime, with rapidly-decreasing harmonic intensities; (2) the harmonic plateau, in which the intensity of a particular odd-harmonic peak is roughly frequency-independent; and (3) the cutoff region, where again the harmonic peaks' intensity goes down exponentially. The cutoff energy E_c is given by

$$E_c = I_p + 3.17U_p \ , \quad \text{where } U_p = \frac{E_\circ^2}{4\omega_L^2} \tag{1.2}$$

where U_p is the ponderomotive energy [71, 72].

The HHG process is often described by the semi-classical three-step model [72–75], pictured in Figure 1.4. Here, the atom is represented by a potential energy curve, shown on the bottom left of the figure, which is to be distorted by the applied laser field. In the first step, an electronic wave packet (EWP) is released into the continuum, with zero kinetic energy, at a time t_i either by multi-photon ionization or by tunnelling through the barrier created by the combined Coulomb and laser potentials (1). Once the EWP is liberated, it is affected only by the Lorentz force due to the laser field, not the Coulomb force due to the remaining ion. Thus, the EWP accelerates (2) under the influence of $E(t)$, governed by the equation of motion

$$\ddot{x}(t) = -\vec{E}(t) \cdot \hat{x} = -E_\circ \cos \omega_L t \tag{1.3}$$

where, assuming that the pulse length $T_p \gg 1$, the effect of the pulse envelope can be neglected. The EWP follows a particular trajectory $x(t)$, until it recombines (3) with its parent ion at a time t_r. Upon recombination, a high-energy photon is released, with an energy equal to the kinetic energy of the returning EWP plus the ionization potential I_p.

Integrating the equation of motion in Eq. 1.3, using the initial conditions $x(t_i) = \dot{x}(t_i) = 0$, one obtains

$$\dot{x}(t) = -\frac{E_\circ}{\omega_L} \left[\sin(\omega_L t) - \sin(\omega_L t_i)\right] \tag{1.4}$$

$$x(t) = \frac{E_\circ}{\omega_L^2} \left[\cos(\omega_L t) - \cos(\omega_L t_i) + \omega_L (t - t_i) \cdot \sin(\omega_L t_i)\right] \tag{1.5}$$

By solving Eq. 1.5 numerically, one finds that there are two distinct pathways – two sets of related ionization/recombination times (t_i, t_r) – that correspond to the same return kinetic energy, giving rise to harmonic emissions that can interfere with each other; this is

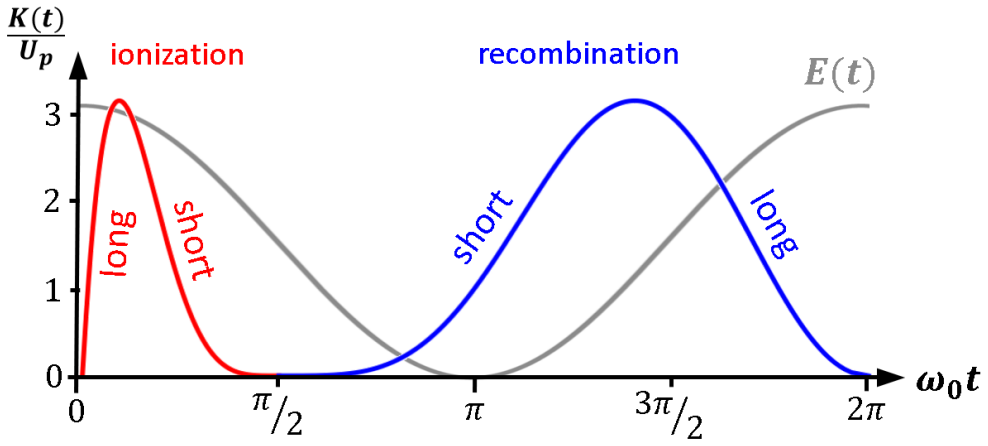

Figure 1.5: Kinetic energy of the returning electron, for different ionization and recombination phases. There are two valid ionization/recombination phases for each value of the return kinetic energy, corresponding to the *short*- and *long*-trajectory pathways.

shown in Figure 1.5. For instance, an EWP which is released at $t = \pi T_L/4$ will return near $t = \pi T_L$ with a kinetic energy of $1.5U_p$. Similarly, an electron ionized near $t = 0.1\pi T_L$ will return at $t = 7\pi T_L/8$, with the same kinetic energy but having taken longer to make the trip. These two pathways are called "short" and "long" quantum orbits, or trajectories [73, 92, 93], respectively. In most experiments, phase matching conditions strongly favor the short-trajectory contributions [94–98]. As a consequence, in most of the calculations shown in Chapters 3 and 4, I therefore also consider mainly the short-trajectory contributions. Finally, the slope of the return kinetic energy (the derivative of the blue curve in Fig. 1.5, $U_p^{-1}\partial_t K(t)$) is called the *attochirp* [93, 99] – more formally, the group delay dispersion – and reflects the fact that different photon energies are emitted at different times. The attochirp is positive for short trajectories, and negative for long trajectories.

Chapter 2. Theoretical Methods

In this chapter, I discuss the theoretical and numerical methods used in order to simulate and subsequently characterize the structure and dynamics of molecules, including charge migration. After an introduction to atomic units (Sec. 2.1), I explore the method of time-dependent density-functional theory (TDDFT) from a user's perspective in Sec. 2.2. Finally, I formalize the discussion of high-harmonic spectroscopy from the previous chapter in Sec. 2.3, with the aim of computing the high-harmonic spectrum within real-spaced TDDFT.

2.1. Atomic Units

When studying atomic physics, it is often convenient to work in atomic units (a.u.) [100], in which the reduced Planck constant $\hbar$, the mass of the electron m_e, the fundamental electronic charge e, and the Bohr radius $a_\circ$ are all taken to equal 1, and all other quantities are derived. This system of units is closely related to Bohr's model of the hydrogen atom, pictured in Fig. 2.1. Here, the orbital angular momentum of the electron $l = m_e v r$ is quantized: $l = n\hbar$. In the hydrogenic ground state (the first Bohr orbit, $n = 1$), an electron of mass m_e and charge $-e$ orbits the nucleus at a radius $a_\circ$, at a rate such that it travels a distance subtended by 1 radian in 1 atomic time unit, and a photon with energy $E = 0.5\,\mathrm{H} = 1\,\mathrm{Ry}$ (atomic energy unit) is needed in order to ionize this electron. Using atomic units, the time-dependent Schrödinger equation (TDSE) simplifies to

$$i\frac{\partial}{\partial t}\Psi(\vec{r},\,t) = \left[-\frac{\nabla^2}{2} + V(\vec{r},t)\right]\Psi(\vec{r},t) \tag{2.1}$$

where V is the total potential energy and Ψ is the time-dependent wavefunction. Atomic units will be used throughout, unless otherwise stated.

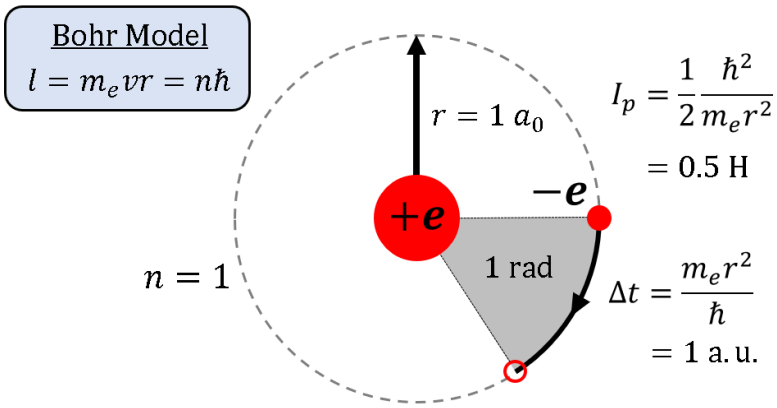

Figure 2.1: Bohr model for the hydrogen atom.

2.2. Time-Dependent Density Functional Theory

Despite looking simple enough, the time-dependent Schrödinger Equation (TDSE) $\hat{\mathcal{H}}\,|\psi\rangle = i\partial_t\,|\psi\rangle$ of Eq. 2.1 can be extremely complicated, even using numerical methods, when considering systems with several electronic and nuclear degrees of freedom, such as molecules [101–104] (even small ones). Even after applying the frozen-nuclei approximation, in which the electrons are assumed to be moving in the potential created by fixed-in-space nuclei, the N-electron Hamiltonian is quite formidable:

$$\hat{\mathcal{H}}_{\text{elec}} = -\sum_{i=1}^{N}\frac{1}{2}\nabla_i^2 - \sum_{i=1}^{N}\sum_{A=1}^{M}\frac{Z_A}{r_{iA}} + \sum_{i=1}^{N}\sum_{j>i}^{N}\frac{1}{r_{ij}} \tag{2.2}$$

where the index A denotes a nucleus and the indices i and j denote electrons. Here, Z_A is the charge of the A^{th} nucleus, r_{iA} is the distance between the i^{th} electron and the A^{th} nucleus, and r_{ij} is the distance between the i^{th} and j^{th} electrons. This level of complexity renders the TDSE analytically and computationally intractable for systems with more than just a few electrons [101–103]. In particular, for my studies of correlation-driven multi-electron quantum dynamics (*e.g.* CM), the exponential scaling of the N-electron Hamiltonian in Eq. 2.2 is untenable.

As an alternative, I use time-dependent density-functional theory (TDDFT), which is a formally-exact, computationally-tractable theoretical approach to the quantum many-body problem [102, 104–107]. The primary appeal of TDDFT is to be able to replace the time-dependent many-body wave function $\Psi(\vec{r}_1, \vec{r}_2, \ldots, \vec{r}_N, t)$ of $3N + 1$ variables (where N is the number of electrons in the system) with a one-body density $n(\vec{r}, t)$, which depends on only 4 variables (three for space and one for time). This is depicted in Figure 2.2. Mathematically, the one-body density is defined by

$$n(\vec{r}, t) = N \int \mathrm{d}^3\vec{r}_2 \cdots \int \mathrm{d}^3\vec{r}_N \left|\Psi(\vec{r}, \vec{r}_2, \ldots, \vec{r}_N, t)\right|^2 \tag{2.3}$$

Here, the N-electron wavefunction is integrated over all electron coordinates except one – note that the choice of which electrons' coordinates to integrate over is arbitrary. The central theorem of TDDFT (called the Runge-Gross theorem) states, for many-body systems evolving from a fixed initial state, that there is a one-to-one correspondence between the above-defined electron density $n(\vec{r}, t)$ and the time-dependent external potential $V_{\mathrm{ext}}(\vec{r}, t)$ which produces that density [104, 105]. Thus, if we can find a potential – any potential – that reproduces the electron density of Eq. 2.3, then the full time evolution of the system can be determined using that potential.

The goal of TDDFT is to design a fictitious system of non-interacting electrons which reproduces the electron density of the fully interactive system [102], following the procedure laid out by Kohn and Sham [108, 109] twenty years earlier in the case of ground-state density-functional theory (DFT). In the Kohn-Sham (KS) formalism, the TDDFT equations are given by

$$\left(-\frac{\nabla^2}{2} + V_{\mathrm{KS}}[n](\vec{r}, t)\right)\phi_i(\vec{r}, t) = i\frac{\partial}{\partial t}\phi_i(\vec{r}, t) \tag{2.4}$$

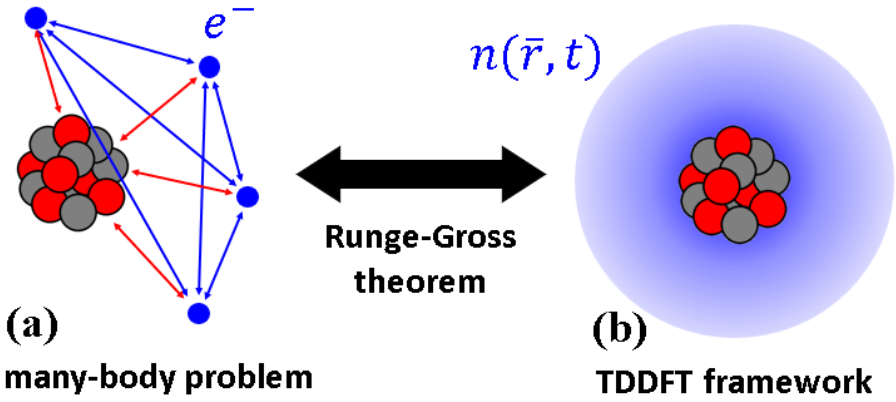

Figure 2.2: (a) Depiction of the quantum many-body problem: here, each electron must interact with every other electron and the nucleus. (b) Depiction of the TDDFT framework: the electrons are replaced by a density $n(\vec{r},t)$ which, via the Runge-Gross theorem, proceeds identically to the many-body description.

Here, $V_{\mathrm{KS}}(\vec{r},t)$ is the KS potential, and $\{\phi_i(\vec{r},t)\}$ is the set of N orthonormal single-particle Kohn-Sham orbitals. Though these orbitals have not been mathematically proven to be physical quantities, they are often a good starting point for the qualitative interpretation of molecular orbitals [110–112]. These Kohn-Sham orbitals generate the time-dependent density of Eq. 2.3:

$$n(\vec{r},t) = \sum_{i=1}^{N} n_i(t)\left|\phi_i(\vec{r},t)\right|^2 , \tag{2.5}$$

where $n_i(t)$ are the time-dependent orbital occupation numbers. The density in Eq. 2.5 is equal to the one-body density of the interacting system from Eq. 2.3. These equations, known as the time-dependent Kohn-Sham equations, would be equivalent to the TDSE in Eq. 2.1 *if* we knew the exact form of the Kohn-Sham potential V_{KS} in Eq. 2.4.

The time-dependent Kohn-Sham potential $V_{\mathrm{KS}}(\vec{r},t)$ is traditionally decomposed

into three parts [102, 104, 106]:

$$V_{\mathrm{KS}}[n](\vec{r},t) = V_{\mathrm{ext}}(\vec{r},t) + V_{\mathrm{H}}[n](\vec{r},t) + V_{\mathrm{xc}}[n](\vec{r},t)\ , \quad \text{where } V_{\mathrm{H}}[n](\vec{r},t) = \int \mathrm{d}^3\vec{r}\,' \ \frac{n(\vec{r}\,',t)}{|\vec{r}-\vec{r}\,'|} \tag{2.6}$$

The first term is the time-dependent external potential V_{ext}, and the second term is the electrostatic potential due to the electron density, called the Hartree potential V_H, defined explicitly in Eq. 2.6. Finally, the last term is the exchange-correlation (XC) potential V_{xc} [113–115], which contains all of the information about non-classical interactions (*e.g.* the Pauli principle) within the original many-body system. Though there is no closed-form analytical expression for the XC potential in terms of the one-body density, there are many good approximations (of varying computational costs) to choose from.

For my purposes, TDDFT is a good choice for studies of HHS of charge migration because (1) it has the ability to systematically handle large molecules with many active and correlated electrons [18, 101–104], and (2) the one-body density $n(\vec{r},\, t)$ defined by Eq. 2.3 above is the physical observable for CM [35]. Furthermore, TDDFT is also designed to simulate time-dependent laser-matter interactions, making it ideal for performing high-harmonic spectroscopy on various molecules [110, 116]. Though there have been recent attempts to perform high-harmonic spectroscopy using Gaussian basis-set TDDFT [117], grid-based TDDFT [118–120] is the more natural choice for HHS because one needs to be able to accurately describe the electron dynamics far away from the molecule.

2.2.1. Necessary Approximations

As a practitioner of TDDFT, there are a few (often inconsequential, but nonetheless present) approximations inherent to the framework that one should be mindful of

when performing simulations and analyzing their results:

1. **adiabatic approximation**: Formally, the functional dependence of V_{xc} involves the full history of the electron density $n(\vec{r},t)$ and the initial condition; in practice, I instead assume an adiabatic (local-in-time) approximation to the XC functional, described by $V_{xc}[n](\vec{r},t) = \tilde{V}_{xc}[n](\vec{r})|_{n=n(t)}$ [102, 107, 121, 122].

2. **local-density-approximation XC functional**: I also use a local-density-approximation (LDA) XC functional [123–125], in which $V_{xc}(\vec{r}_\circ,t)$ depends only on $n(\vec{r}_\circ,t)$ for every $r_\circ$ within the simulation domain (as opposed to the electron density and its spatial derivatives). Using this type of functional and the adiabatic approximation above, $V_{xc}(\vec{r},t)$ is equal to the XC potential of a static (frozen at each time t) homogeneous electron gas of density $n(\vec{r},t)$ [102].

3. **spin-restricted**: In principle, the N-electron Hamiltonian in Eq. 2.4 could differ for spin-up and spin-down Kohn-Sham orbitals [102, 107] (especially for open-shell systems). For my simulations, I use a spin-restricted system, where the spin-up and spin-down channels are identical.

4. **average-density self-interaction correction (ADSIC)**: Since electrons are indistinguishable from one another within the electron density $n(\vec{r},t)$, I must use a self-interaction correction which removes electrons' interactions with themselves [126–128]. Here, I use an average-density self-interaction correction (ADSIC).

5. **dipole approximation**: I neglect the spatial variation of the applied electromagnetic field over the simulation region: $\vec{E}(\vec{r},t) = \vec{E}(t)|_{\vec{r}=0}$. This is known as the dipole approximation [122].

The second class of approximations that I consider are due to the implementation of TDDFT on a real-spaced grid. For my TDDFT calculations, I use the open-source code Octopus [118–120, 129, 130], which solves the Kohn-Sham equations on a user-defined Cartesian grid.

1. **pseudopotentials**: Even with the approximations noted above, TDDFT simulations which explicitly include all electrons are often not feasible on a real-spaced grid. The core orbitals are extremely localized on a single atomic site, meaning that an exceedingly small spacing would be needed to accurately capture the specifics of those core orbitals [131], while interactions with a strong laser field often require relatively large box sizes due to the need to simulate electron density far away from the core (e.g. the HHG process) [110]. Instead, I represent an atom's nucleus and its core electrons – all but the relatively-delocalized valence electrons – by a pseudopotential. Here, atoms are represented by either PSF-type [132–136] or HGH-

type [137] pseudopotentials.

2. **time propagation**: I want to take the initial state of the system $\{\phi_i(\vec{r}, t_\circ)\}$ and propagate it forward in time until it reaches a final time t. For this purpose, the time-dependent Kohn-Sham equations of Eq. 2.4 can be rewritten as:

$$\phi_i(\vec{r}, t) = \hat{U}(t, t_\circ)\, \phi_i(\vec{r}, t_\circ) \ , \quad \text{where } \hat{U}(t, t_\circ) = \hat{\mathcal{T}} \exp\left[-i \int_{t_\circ}^{t} \mathrm{d}t' \ \left(-\frac{\nabla^2}{2} + V_{\mathrm{KS}}(\vec{r}, t')\right)\right] \tag{2.7}$$

where the time-ordering operator $\hat{\mathcal{T}}$ is important since the Kohn-Sham potential V_{KS} is time-dependent [102, 107]. Due to this time-ordering operator, the expression in Eq. 2.7 is too complicated to apply directly, and so $\hat{U}(t, t_\circ)$ must be approximated instead. For my simulations, I use the enforced time-reversal symmetry (ETRS) scheme, or its approximated form (AETRS), both of which have been extensively tested [121, 138]. Both of these propagators assert that the system is time-reversible:

$$\exp\left[i\left(\frac{\delta t}{2}\right)\hat{\mathcal{H}}(t+\delta t)\right]\ \phi(t+\delta t) = \exp\left[-i\left(\frac{\delta t}{2}\right)\hat{\mathcal{H}}(t)\right]\ \phi(t) \tag{2.8}$$

The approximation then lies in determining $\hat{\mathcal{H}}(t+\delta t)$, which defines the difference between ETRS and AETRS.

2.3. High-Harmonic Spectroscopy

High-harmonic spectroscopy (HHS) is the application of HHG, discussed in Sec. 1.3, to study a wide range of static and dynamic properties of atomic, molecular, and condensed-phase systems (see Refs. [77, 82–84, 90], among many others). Since the underlying HHG process relies on ultrashort laser pulses, HHS is ideal for investigating the fastest electronic processes, such as charge migration. Here, the returning electron wave packet (EWP) coherently probes the remaining cation with sub-laser-cycle resolution (see again the discussion around Fig. 1.5) [67]. The primary goal of HHS is to access the dipole matrix element between this recombining EWP in the continuum and the bound molecular orbital, called the recombination dipole matrix element, or RDME; this information is imprinted in the frequency-dependent amplitude and phase of the harmonic radiation [110].

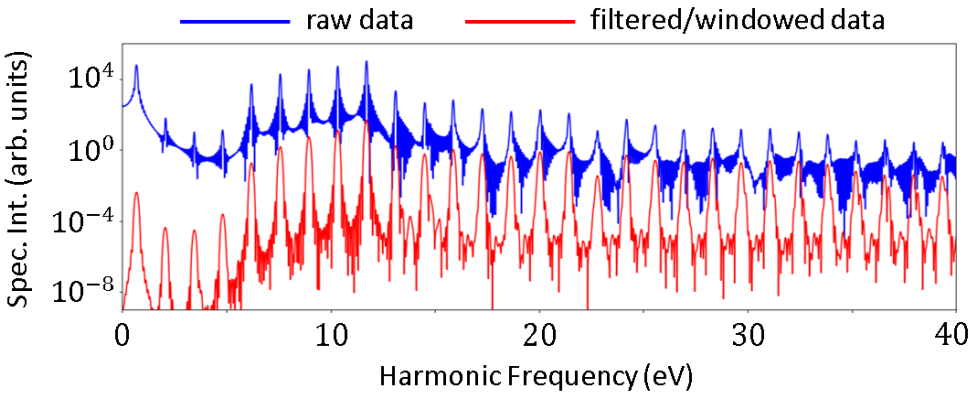

Figure 2.3: Comparison of calculated high-harmonic spectra for the filtered and windowed dipole acceleration (red) and the raw data (blue). Data taken from a TDDFT simulation of bromobutadiyne (BrC_4H) using a laser with a wavelength of 1800 nm, and an intensity of 60 TW/cm^2.

From my TDDFT simulations, I obtain the dipole moment $\vec{d}(t) = \langle\Psi|\vec{r}|\Psi\rangle$ and/or the dipole acceleration $\vec{a}(t) = \frac{\mathrm{d}^2}{\mathrm{d}t^2}\vec{d}(t) = -\langle\Psi|\vec{\nabla}V|\Psi\rangle$, from which I can extract both amplitude and phase information:

$$S_{\mathrm{tot}}(\omega) = \sum_{i=1}^{3} S_i(\omega) = \sum_{i=1}^{3} \left|D_i(\omega)\right|^2 \quad \text{(spectral intensity)} \tag{2.9}$$

$$\varphi_{\mathrm{tot}}(\omega) = \frac{\sum_{i=1}^{3}[S_i(\omega)\,\varphi_i(\omega)]}{S_{\mathrm{tot}}(\omega)}\,, \quad \text{where } \varphi_i(\omega) = \arg\left(\frac{D_i(\omega)}{D_{\mathrm{ref}}(\omega)}\right) \quad \text{(phase)} \tag{2.10}$$

where $D_i(\omega)$ is the complex dipole signal in the frequency domain along the i^{th} Cartesian direction, which has been windowed using $W(t)$ and (optionally) high-pass-filtered using $F(t)$:

$$D_i(\omega) = \mathcal{F}[W(t)\,\tilde{a}_i(t)](\omega), \quad \tilde{a}_i(t) = [F * (\vec{a}\cdot\hat{x}_i)](t) \tag{2.11}$$

where ω is the frequency of the emitted high-harmonic light and $*$ denotes the convolution operator. Because the harmonic phase accumulates very rapidly even in the absence of any distinguishing features (for instance, HHG from a single atom), I normalize the complex dipole signal in Eq. 2.10 by a reference signal $D_{\mathrm{ref}}(\omega)$ which is essentially featureless

in the spectral region of interest. This reference signal can be obtained, for instance, by computing the dipole signal from a one-dimensional atomic-like system with the same ionization potential as the full molecular system.

For the complex dipole signal in Eq. 2.11 above, I apply a high-pass filter F with a cutoff frequency $\omega_c = 20\,\text{eV}$, which removes intense low-frequency components in the dipole signal found in the perturbative region of the harmonic spectrum that would bleed into higher frequencies when I apply the short time-selection window $W(t)$. The window function $W(t)$ has two purposes: first, it forces the harmonic signal to go to zero at both ends, eliminating high-frequency artifacts in the Fourier transform which are unphysical and therefore unwanted. Second, it allows me to select the time-dependent response from one or multiple half-cycles of the laser field. In general, $W(t)$ is defined as

$$W[t_\circ, \tau, p](t) = \begin{cases} \cos^{2p}\left(\frac{\pi(t-t_\circ)}{\tau}\right), & t_\circ - \frac{\tau}{2} \leq t \leq t_\circ + \frac{\tau}{2} \\ 0, & \text{otherwise} \end{cases} \tag{2.12}$$

where $t_\circ$ is the central time, τ is the window width, and p is a positive integer which determines the steepness of the window (usually $p = 1$ or 2). The effects of filtering and windowing on an example harmonic spectral intensity is shown in Figure 2.3.

Another useful tool for analyzing the harmonic emission is the Gabor transform, or spectrogram. This time- and harmonic-frequency-dependent signal is constructed by taking many windowed spectra, using small windows with $\tau \approx 50\,\text{a.u.}$, centered around different times. Examples of spectrograms are given in Figure 2.4, for a one-dimensional atomic-like potential. A spectrogram is used to map out which harmonic frequencies were emitted at what time within the laser cycle, providing an observation of the blue curve

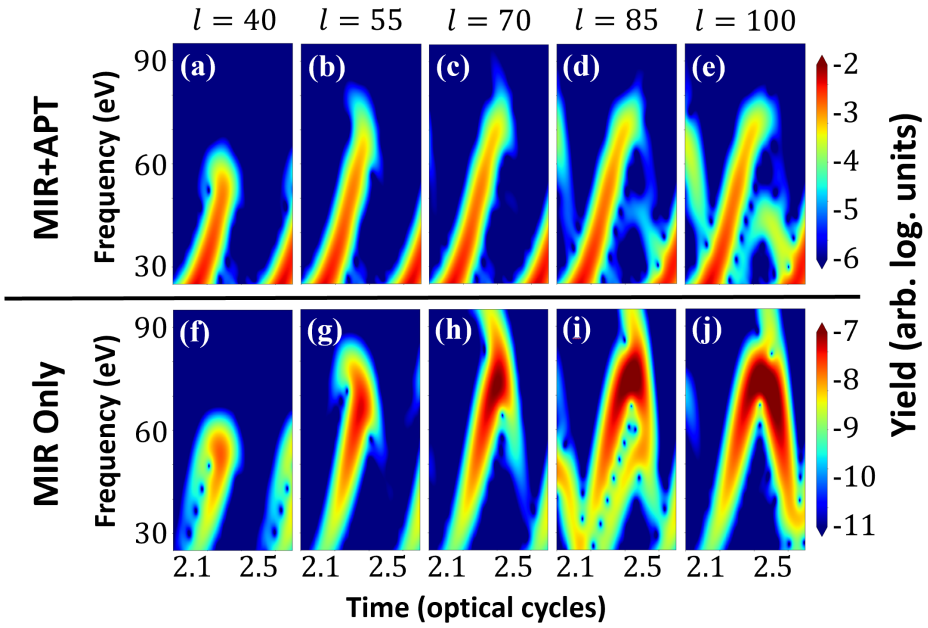

Figure 2.4: Gabor transforms of 1D HHG simulations in Octopus, for (a-e) an APT-seeded and a (f-j) MIR-only driving laser, for five different simulation box lengths. As l increases, the long-trajectory contribution to the dipole signal increases.

in Fig. 1.5. Constructing the spectrogram requires access to the time-dependent dipole signal; thus, both amplitude and phase information is necessary.

In Sec. 2.2.3.1, I discuss the above-mentioned methods for enhancing the short-trajectory contribution to the harmonic signal. In Sec. 2.2.3.2, I derive a method for determining the isotropic (orientation-averaged) harmonic spectrum from relatively few calculations, and in Sec. 2.2.3.3, I discuss how to isolate the contributions of individual Kohn-Sham orbitals to the harmonic signal in order to further refine my future analyses.

2.3.1. Short-Trajectory Selection

In an experiment, the short-trajectory contribution dominates, due to macroscopic effects (*e.g.* phase matching) in the laser focal volume [94–97]. In my grid-based TDDFT simulations, which are done for a single molecule, there are no such macroscopic effects, and the interference between the short- and long-trajectory contributions of Fig. 1.5 yields

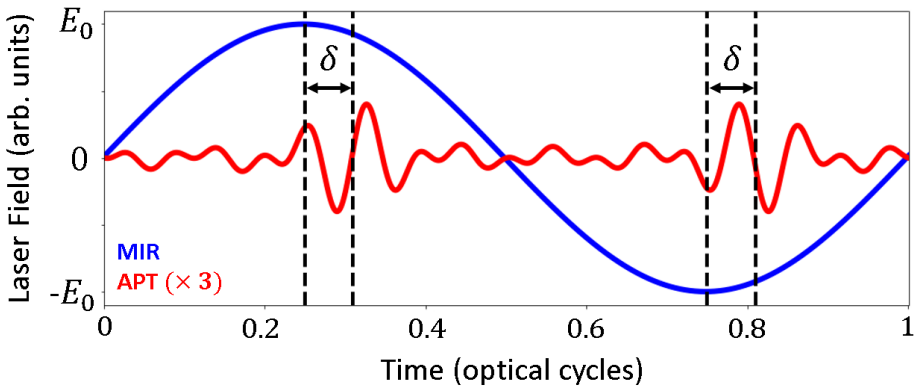

Figure 2.5: An illustration of the laser fields used to select the short-trajectory contribution to the HHG signal in TDDFT computations. The APT (red) is synchronized with the mid-infrared (MIR) HHG-driving laser field (blue).

a complicated harmonic spectrum. Thus, I attempt to filter out the long-trajectory contributions in two ways: (1) using a complex absorbing potential (CAP) [139–141], and/or (2) using an attosecond pulse train (APT) [94, 98, 142–144].

Since the long quantum orbits travel further away from the ionization event (thus taking longer to return), they can be suppressed by placing an absorbing boundary [139] at the maximum excursion distance of the short-trajectory contribution, called the quiver radius. In Octopus, this absorbing boundary condition is defined by

$$V_{\mathrm{CAP}}(x_i) = i\eta \sin^2\left(\frac{\pi x_i}{2w}\right) \quad , \quad \text{where } L_{x_i} - w \leq x_i \leq L_{x_i} \tag{2.13}$$

where $\{\eta, w\}$ are the parameters of the CAP described by the Octopus variables `ABCapHeight` and `ABWidth`, respectively, and L_{x_i} is the length of the box in the x_i direction. By default, I use $\eta = -1$ and $w = 15$ atomic units. Then, by scaling the length of the simulation box in the direction of the driving laser polarization to the quiver radius of the HHG electron, defined by $\alpha_\circ = E_\circ/\omega_L^2$, I can suppress the long-trajectory contribution to the dipole signal. The issue with this approach is that by placing the absorbing boundary conditions at the quiver radius, I am intentionally eating electron density (that of the

long-trajectory contribution to the HHG signal). This means that if the laser intensity is too high, a significant portion of the total electron density could be eaten by the absorbing boundary (not returning to the molecule in the third step of HHG), causing unexpected changes in both structural and dynamic features.

The second method of enhancing the short-trajectory contribution to the harmonic signal is to include another laser field, which is composed of harmonics of the HHG-driving laser field. The combination of these harmonics of the fundamental laser field, with the correct phases, leads to a series of localized-in-time laser pulses, called an attosecond pulse train (APT) – see Figure 2.5. The purpose of the APT is to replace the tunnel ionization in the first step of the HHG process with one-photon ionization, so that I can control when the ionization is happening on a sub-cycle level. This APT is timed to coincide with the release of each short-trajectory burst of the laser field – see again Fig. 1.5 [143]; here, the delay δ between the peaks of the HHG-driving laser field and the APT is approximately 0.06 optical cycles (o.c.). While the use of an APT often improves the ability of TDDFT calculations to extract target-specific information from the HHG signal, it also has the opportunity to disproportionately ionize electrons from lower-lying Kohn-Sham orbitals which may not contribute to the signal otherwise.

As an illustration of these two different methods, in Figure 2.4, I vary the length of a one-dimensional simulation box between 40 and 100 atomic units, and perform HHG on an atomic-like pseudopotential sitting at $x = 0$, using both an MIR-only and an APT-seeded driving laser. For the laser parameters used in these 1D simulations, the quiver radius is $\alpha_\circ = 50\,\text{a.u.}$, and the semiclassical cutoff energy is $E_c = 70\,\text{eV}$. By doing this, one can clearly see that increasing the box length past $\alpha_\circ$ in either the MIR-only

or APT-seeded case causes a significant amount of long trajectories to appear, causing unwanted interference in the HHG spectrum (not shown). The feasibility of using the absorbing boundary conditions versus the APT-ionization seed to select the short-trajectory contributions can be strongly limited by the specifics of the problem at hand. That said, I can deduce some generic pros and cons to each approach. For the CAP, the obvious advantage is that it is the closest to experimental conditions since no additional laser field is added to the simulations. This means that one can expect the wavelength and intensity-dependence of the ionization to be relatively well-accounted for, especially for Kohn-Sham channels that are close to each other energetically. On the other hand, the absorbing boundary conditions must essentially leave the short-trajectory component intact while damping the long-trajectory component and without inducing spurious reflections. Simultaneously fulfilling these conditions can become increasingly difficult for shorter-than-MIR wavelengths. For the APT, in addition to the difficulty of recombining the dipole signal from different Kohn-Sham channels, the performance of the ionization seed is dependent upon a proper calibration of the APT. This includes avoiding APT-field-induced effects (see, for instance, Sec. 3.3), and there are no one-size-fits-all solutions.

2.3.2. Orientation Averaging using Lebedev Grids

In an experiment, molecules in the gas phase are randomly oriented unless aligned by a laser field. Thus, in order to make accurate quantitative comparisons to experimental HHG spectra, one must compute an orientation-angle-averaged (or isotropic) harmonic spectrum [145, 146].

In general, it takes three angles to describe an object's orientation with respect to

some reference frame. They can be defined equivalently by Euler or Tait-Bryan angles; I will be using the latter, since they are the easiest to work with in this case. Any rotation of a molecule in three-dimensional space can be defined in terms of these Tait-Bryan angles:

$$\hat{R}(\phi, \theta, \psi) = \hat{R}_x(\psi)\hat{R}_y(\theta)\hat{R}_z(\phi) \tag{2.14}$$

where $\hat{R}_k$ is the rotation operator around the k^{th} Cartesian axis (in a stationary reference frame), and $\phi \in [0, 2\pi)$, $\theta \in [0, \pi)$, and $\psi \in [0, 2\pi)$. More familiarly, the non-technical terms for ϕ, θ, and ψ would be the *yaw*, *pitch*, and *roll*, respectively. However, without loss of generality, one can safely ignore rotations around the laser polarization axis (which I will define here as $\hat{x}$), and so we can ignore the ψ-dependence in Eq. 2.14. Thus, the next step is to sample points (θ, ϕ) on the unit sphere $\mathbb{S}^2$ in a consistent way, so that I can compute the isotropic harmonic spectrum:

$$\overline{S}(\omega) \equiv \sum_k \left| \int_0^{\pi} \sin\theta \, \mathrm{d}\theta \int_0^{2\pi} \mathrm{d}\phi \; \tilde{D}_k[\theta, \phi](\omega) \right|^2 \tag{2.15}$$

where $\tilde{D}_k[\theta, \phi](\omega)$ is the windowed Fourier transform of the dipole moment, defined by Eq. 2.11, along the k^{th} Cartesian axis, for a particular orientation (θ, ϕ) of the molecule.

For any arbitrary function $f(\theta, \phi)$, the surface integral over the unit sphere $\mathbb{R}^2$ can be approximated by a Riemann sum

$$I[f] = \int_0^{\pi} \sin\theta \, \mathrm{d}\theta \int_0^{2\pi} \mathrm{d}\phi \; f(\theta, \phi) \approx \sum_i w_i \, f(\theta_i, \phi_i) \tag{2.16}$$

where w_i is the weight corresponding to a particular orientation (θ_i, ϕ_i). Different methods of sampling points on $\mathbb{S}^2$ have already been thoroughly investigated [147]. I will use the Lebedev quadrature rule [148]; despite its limited flexibility in choosing the number of grid

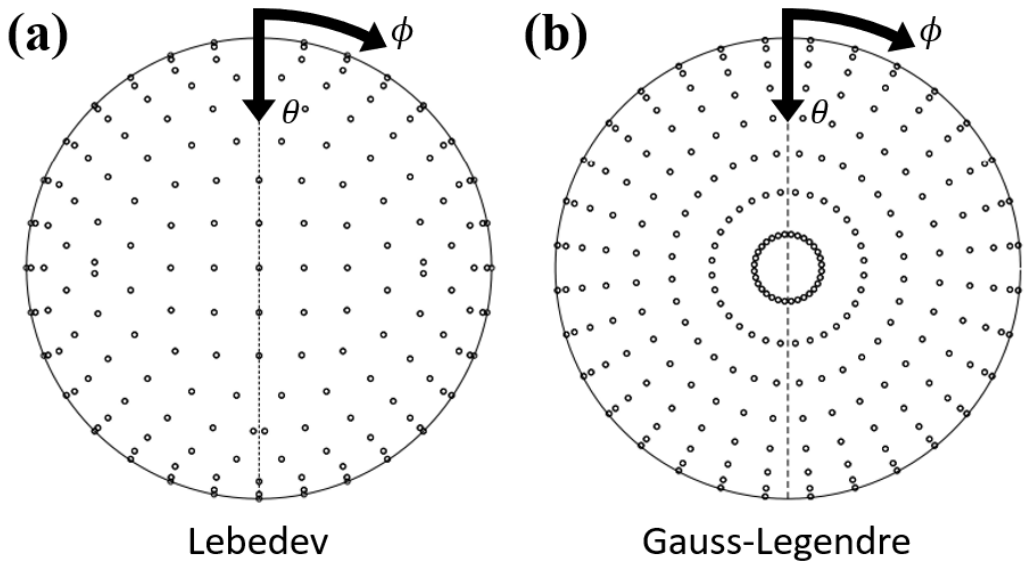

Figure 2.6: Examples of two quadrature rules: (a) Lebedev grid with 350 points, and (b) Gauss-Legendre grid with 512 points. Adapted from [149].

points to use, it outperforms product grids such as the Gauss-Legendre quadrature – see Fig. 2.6 [149]. The Lebedev quadrature is constructed such that it has octahedral-rotation and inversion symmetries; and, as with any quadrature rule, the grid points and weights are determined by enforcing the exact integration of polynomials up to a given order.

The Lebedev quadrature rule provides the most efficient way to sample over the surface of $\mathbb{S}^2$; however, by exploiting the symmetries of the molecule, I can further reduce the number of simulations required in order to compute the isotropic harmonic spectrum. As an example, rotating a benzene molecule by π radians in the plane of the molecule yields the exact same ground-state electron density – thus, the harmonic signal induced by the applied laser field will also be identical. Using the Lebedev grid without these considerations, I would treat these two orientations separately, even though only one simulation (with twice the weight) is required to achieve the same result.

To further capitalize on the molecular symmetries, I look for pairs of orientations

whose ground-state densities are consistent when one is rotated around one of the three Cartesian axes; for each of these pairs, I can determine how their corresponding dipole moments are related, add them together, and then only have to simulate one of those orientations.

Let us define π-rotation operators around each of the three Cartesian axes, which act on time-dependent electron densities $\rho(\vec{r},t)$ in a monochromatic electric field:

$$\begin{cases} \hat{\Pi}_x\rho(\vec{r},t) \equiv \hat{R}_x(\pi)\rho(\vec{r},t) = \rho(x,-y,-z,t) \\ \hat{\Pi}_y\rho(\vec{r},t) \equiv \hat{R}_y(\pi)\hat{U}(t+T_L/2,t)\rho(\vec{r},t) = \rho(-x,y,-z,t+T_L/2) \\ \hat{\Pi}_z\rho(\vec{r},t) \equiv \hat{R}_z(\pi)\hat{U}(t+T_L/2,t)\rho(\vec{r},t) = \rho(-x,-y,z,t+T_L/2) \end{cases} \tag{2.17}$$

For rotations around the y and z axes, the rotation operator $\hat{R}$ needs to be accompanied by a time-translation operator $\hat{U}$ which advances the laser field by one-half optical cycle, since for a monochromatic laser field $E(t) = -E(t+T_L/2)$.

For the trivial case described above, that of a benzene molecule rotated by π radians in the plane of the molecule, the π-rotated ground-state electron density $\rho[\theta',\phi'](\vec{r})$ is identical to the original ground-state density $\rho[\theta,\phi](\vec{r})$; therefore, all three components of the corresponding dipole moments are also identical. However, suppose that I find that two orientations' ground-state electron densities are not identical, but instead related by a $\hat{\Pi}_z$ rotation. Mathematically, this can be represented by:

$$\rho[\theta',\phi'](\vec{r},t) = \hat{\Pi}_z\rho[\theta,\phi](\vec{r},t) = \rho[\theta,\phi](-x,-y,z,t+T_L/2) \tag{2.18}$$

for two unique orientations (θ,ϕ) and (θ',ϕ') of the molecule. Then the corresponding

dipole moment in the x-direction is given by

$$\begin{aligned} d_x[\theta', \phi'](t) &= \iiint_{\mathbb{R}^3} x \ \rho[\theta', \phi'](\vec{r}, t) \ \mathrm{d}x \, \mathrm{d}y \, \mathrm{d}z \\ &= \iiint_{\mathbb{R}^3} x \ \rho[\theta, \phi](-x, -y, z, t + T_L/2) \ \mathrm{d}x \, \mathrm{d}y \, \mathrm{d}z \end{aligned} \tag{2.19}$$

Then, using the following properties of integrals:

$$\begin{cases} \int_{-\infty}^{\infty} f(x)g(x) \, \mathrm{d}x = \int_{-\infty}^{\infty} f(-x)g(x) \, \mathrm{d}x, & \text{even } g(x) \\ \int_{-\infty}^{\infty} f(x)g(x) \, \mathrm{d}x = -\int_{-\infty}^{\infty} f(-x)g(x) \, \mathrm{d}x, & \text{odd } g(x) \end{cases} \tag{2.20}$$

the aim is to recover $\rho[\theta, \phi](\vec{r}, t)$ in the integrand and simplify the above equation. For the x integral, $g(x) = x$ is odd; therefore, I gain a minus sign by transforming $-x \to x$. For the y integral, $g(y) = 1$ is even, so no additional minus sign is needed when transforming $-y \to y$. The z integral remains unchanged. Lastly, assuming that $d(t = 0) = 0$, $d(t + T_L/2) = -d(t)$; therefore the time translation provides an additional factor of -1. Thus, assuming that two orientations' ground-state densities are linked by a π-rotation around the z-axis, their x-axis dipole moments $d_x[\theta', \phi'](t) = d_x[\theta, \phi](t)$.

I repeat a similar procedure for the y and z components of the dipole moment, and also for the other two rotations $\hat{\Pi}_x$ and $\hat{\Pi}_y$. Doing so, I find that

$$\hat{1}: \begin{cases} d_x \text{ same} \\ d_y \text{ same} \\ d_z \text{ same} \end{cases} \quad \hat{\Pi}_x: \begin{cases} d_x \text{ same} \\ d_y \text{ opposite} \\ d_z \text{ opposite} \end{cases} \quad \hat{\Pi}_y: \begin{cases} d_x \text{ same} \\ d_y \text{ opposite} \\ d_z \text{ same} \end{cases} \quad \hat{\Pi}_z: \begin{cases} d_x \text{ same} \\ d_y \text{ same} \\ d_z \text{ opposite} \end{cases} \tag{2.21}$$

for a laser polarization axis along $\hat{x}$. This means that if a π-rotation around the x-axis makes two ground-state densities consistent, then one should expect that if I were to do

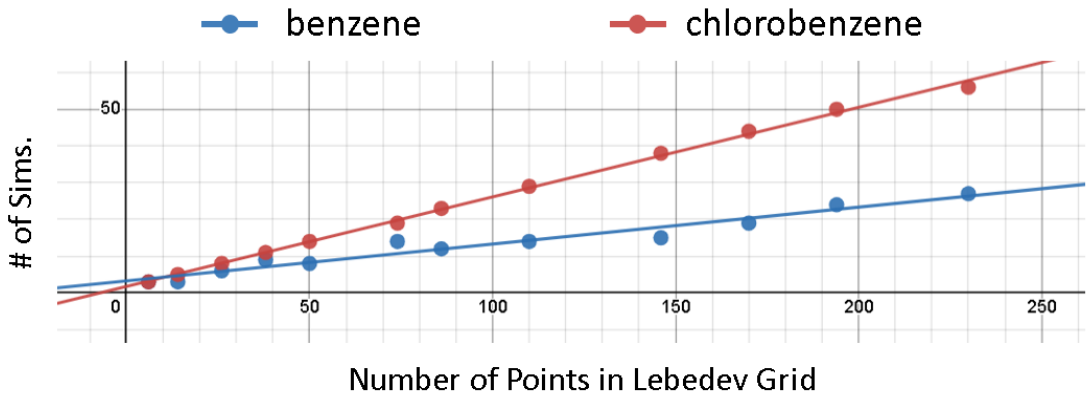

Figure 2.7: Plot showing the reduction of the number of required simulations achieved by exploiting molecular symmetries in benzene and chlorobenzene, as a function of the total number of grid points in the Lebedev quadrature.

both simulations, the resulting dipole signals are identical in the x direction, and opposite (multiplied by -1) in the y and z directions. These results are indeed consistent with simulations of orientation-dependent HHG signals in Octopus.

As a demonstration of the utility of this method, in Fig. 2.7 I show the number of required TDDFT simulations after taking account of molecular symmetries in benzene and chlorobenzene, as a function of the number of points in the Lebedev grid. If I had not done anything, I would expect a line of slope 1. Using the above method, the number of Lebedev grid points per unique simulation (inverse of the slopes of the lines) is approximately 4 for chlorobenzene and 8 for benzene. For less symmetric molecular systems, I expect that the slope of the lines in Fig. 2.7 will converge to 1, and the order of the Lebedev grid required to accurately compute the isotropic harmonic spectrum will increase. More detailed results of isotropic harmonic spectra can be found in Ref. [146].

Looking toward the future, one could imagine further improving the efficiency of the orientation averaging method described here by generating a quadrature rule that matches the point-group symmetry of the molecule. Thus, the ratio between the number

of required simulations and the number of points in the grid reaches its theoretical maximum (per molecule), and so one could use a more precise quadrature without incurring heavy computational costs.

2.3.3. Orbital-Resolved HHS

Even when properly processed, HHG spectra calculated in TDDFT can still be quite congested. Thus, I want to be able to resolve the different contributions from each of the individual orbitals in the total dipole acceleration [110, 150–155]. This breakdown is useful, for example, when looking at two-center interferences which only manifest in a specific orbital symmetry (see Ch. 3) [110]. This functionality is now native to Octopus, as of version 11.0, using the `TDOutputResolveStates` variable; however, because it is a useful exercise, I will explain how I did it before this feature was available.

Given that the one-body density $n(\vec{r},t)$ can be defined in terms of individual Kohn-Sham orbitals – see again Eq. 2.5 – I can rewrite the total dipole moment as a sum of the individual orbitals' dipole contributions:

$$\begin{aligned}\vec{d}(t) &= \iiint \vec{r}\, n(\vec{r},\, t)\, \mathrm{d}^3\vec{r} \\ &= \sum_{k=1}^{N} \vec{d}_k(t) = \sum_{k=1}^{N} \iiint \vec{r}\, |\psi_k(\vec{r},\, t)|^2\, \mathrm{d}^3\vec{r}\end{aligned} \tag{2.22}$$

With Octopus, I can calculate the x-component of the orbital-resolved dipole moment $d_k(t)$ by exporting the transversely-integrated densities $\rho_k(x,t)$ (`OutputFormat = integrate_dydz`), and then use post-processing to calculate

$$\vec{d}_k(t)\cdot\hat{x} = \int x \underbrace{\iint |\psi_k(\vec{r},t)|^2\, \mathrm{d}y\, \mathrm{d}z}_{\rho_k(x,t)}\, \mathrm{d}x \tag{2.23}$$

The y- and z-components of the orbital-resolved dipole moment can readily be calculated

in a similar way:

$$\vec{d}_k(t) \cdot \hat{y} = \int y \underbrace{\iint |\psi_k(\vec{r},t)|^2 \,\mathrm{d}x \,\mathrm{d}z}_{\rho_k(y,t)} \,\mathrm{d}y \tag{2.24}$$

$$\vec{d}_k(t) \cdot \hat{z} = \int z \underbrace{\iint |\psi_k(\vec{r},t)|^2 \,\mathrm{d}x \,\mathrm{d}y}_{\rho_k(z,t)} \,\mathrm{d}z \tag{2.25}$$

A general caveat to the orbital-resolution procedure that I propose here is that (as mentioned in Section 2.2) the Kohn-Sham orbitals of Eq. 2.4 were introduced as non-physical quantities in the construction of the electron density [108, 109] and thus the orbital-resolved dipole signals above do not correspond exactly to experimental observables. However, compared to single-active-electron or static-orbital approximations, I expect time-dependent Kohn-Sham orbitals to provide significant improvements by allowing for (i) laser-field dressing effects such as polarization, Stark shift, reshaping the density, etc., which can qualitatively affect the HHS response [156, 157]; and (ii) multi-channel contributions, if more than one Kohn-Sham channel significantly contributes to the HHG signal and is included in the analysis. Despite their introduction to ground-state DFT as non-physical quantities, the Kohn-Sham orbitals are the closest set of one-particle wavefunctions to the total multi-electron wavefunction. In that sense, I expect that time-dependent Kohn-Sham orbitals to reproduce some elements of fully-correlated models [111, 112], although the qualitative and quantitative agreement is likely to be both system- and observable-dependent [158, 159].

In order to quantitatively compare HHG spectra from different molecules, one needs to correct for the inaccurate ionization potentials (therefore, inaccurate tunnel-ionization rates) computed from TDDFT with LDA [160–163]. This process involves

breaking the total HHG spectrum into contributions from each of the Kohn-Sham orbitals, as described above, and rescaling them in accordance to the correct ionization potential [146]. Thus, the Kohn-Sham orbital resolution method brings us one step closer to bridging the gap between theoretical calculations of HHG spectra and experiment.

Chapter 3. Two-Center Interferences

In this chapter, I apply the methods put forth in Sec. 2.3 by performing high-harmonic spectroscopy (HHS) on molecules in the carbon dichalcogen family (CO_2, CS_2, and CSe_2). These molecules have a well-documented minimum in the high-harmonic spectral intensity due to destructive interference between two prominent centers of charge within the molecule, called a two-center interference (TCI) minimum. I have found that via careful signal processing and normalization, I can identify the TCI minima in several linear, triatomic molecules and compare these results with experiments performed at OSU.

TCI minima are introduced in Sec. 3.1, and the specifics of my analysis can be found in Sec. 3.2. In Sec. 3.3, I validate the orbital-resolved methodology that I outlined in Sec. 2.3.3. I then compare the TCI minima for different molecules in the carbon dichalcogen family (Sec. 3.4), and also for different laser parameters in CO_2 (Sec. 3.5). Finally, I develop and validate field-free scattering simulations performed in MATLAB, which are compared to the full TDDFT simulations in Octopus – see Sec. 2.6.

3.1. Introduction

In the third step of high-harmonic generation (HHG), the recombining electron wave packet (EWP) coherently probes the molecule from which it was ionized, encoding information about structural and dynamical features onto the high-harmonic spectral intensity and phase – see again Sec. 1.3. The simplest example of a structural feature in a molecule is a two-center interference (TCI), which occurs in a molecule whose highest-occupied molecular orbital (HOMO) is predominantly composed of two centers of charge density [141, 157, 164, 165]. Similar in spirit to Young's double-slit experiment, a mini-

mum in the spectral intensity results from the destructive interference between recombination events at each center of charge. The recombining electron wave packet (EWP), depicted as a plane wave with a de Broglie wavelength λ_e, is incident upon a molecule with two prominent charge centers separated by a distance R – see Figure 3.1(a). The EWP sees the effective distance $R\cos\theta$ between the two charge centers when the molecule is rotated in the xy plane. For symmetric molecules like the ones I consider in this chapter, the TCI shifts in energy as a function of the relative angle θ between the laser polarization direction and the molecular axis, according to the equation

$$R\cos\theta = m\lambda_e = m\pi \cdot \sqrt{2E} \;\forall\; m \in \mathbb{Z} \tag{3.1}$$

where λ_e is the electron's de Broglie wavelength, E is the electron's returning kinetic energy, and R is the distance between the two centers of electron density – see Fig. 3.1(a). By rearranging Eq. 3.1, we can conclude that the energy of the destructive interference scales quadratically with the effective distance $R\cos\theta$. For a fixed internuclear distance R (for a given molecular target), this results in a parabolic minimum in the spectral intensity with respect to angle θ, as is shown in Figure 3.2(a).

TCIs have been studied extensively in several molecules, in both experiment and theory [152, 156, 165–171], serving as an excellent demonstration of the ability of HHS to probe the electronic structure of a molecule. To measure a TCI, the molecule's alignment angle θ needs to be controlled with some level of accuracy in a field-free setting, which is achievable with current experimental techniques [172–177]. Once the sample has been aligned, an applied laser field induces HHG, and the resulting complex dipole signal encodes information about the molecule's TCI. Both amplitude and phase information

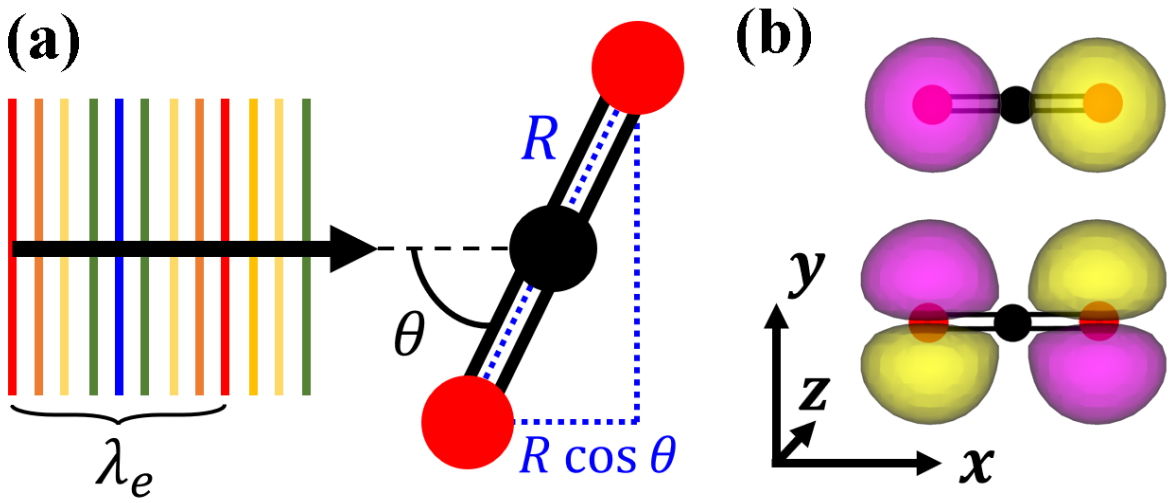

Figure 3.1: (a) Diagram of a two-center interference: the recombining EWP, depicted as a plane wave with a de Broglie wavelength λ_e, is incident upon a molecule with two prominent charge centers (the red atoms) separated by a distance R. The EWP sees the effective distance $R\cos\theta$ between the two charge centers when the molecule is rotated in the xy plane. (b) Isosurfaces of the in-plane (*top*) and out-of-plane (*bottom*) HOMO for CO_2. The purple and yellow lobes have equal amplitude but opposite phase.

(Eqs. 2.9 and 2.10) is crucial to characterizing the TCI minimum [110, 156, 165, 178]. The theoretical work presented here [110, 179] was motivated by experimental results provided by collaborators at The Ohio State University (OSU), in which they were able to characterize the TCI in CO_2 using both intensity and phase information from HHS measurements [165, 179].

3.2. Simulation Details

I investigate symmetric molecules in the carbon dichalcogen family; namely, carbon dioxide (CO_2), carbon disulfide (CS_2), and carbon diselenide (CSe_2), and extract information about the structure of the molecules from TDDFT calculations of HHS. For my real-spaced TDDFT simulations in Octopus, I require a simulation domain that allows for the EWP to freely propagate under the influence of the HHG-driving laser field and subsequently recombine with the molecule. Thus, I use a box that is elongated along the laser

polarization direction, and the length of the box along this axis is scaled to the maximum distance that the short-trajectory contribution to the EWP will travel (the quiver radius). For a laser wavelength of $\lambda = 1500\,\text{nm}$ and an intensity of $60\,\text{TW/cm}^2$, I use a simulation box which is $140 \times 70 \times 60$ atomic units in the x, y, and z directions, respectively, with a grid spacing of 0.3 a.u. in all directions. The laser field is polarized in the x-direction, and I impose the molecular alignment (parameterized by the angle θ) by rotating the target molecule in the xy-plane inside that box. Since the HHG electron wave packet travels along the direction of the laser polarization, I avoid needing to redefine the simulation box to rotate with the laser polarization by instead rotating the molecule within the box.

Because I am using a finite grid spacing, rotating the molecule within the simulation box leads to small changes in its representation on the grid. This leads to an angular dependence of the field-free ionization potential, which is clearly non-physical. With my chosen grid spacing, I have ensured that the energy of the HOMO varies by less than 0.1 eV as the target molecule is rotated. My calculated ionization potentials (simply the negative of the orbital binding energies, according to Koopmans' theorem) are $I_p = 14.5\,\text{eV}$ (experimental 13.8 eV) for CO_2, $I_p = 10.4\,\text{eV}$ (10.1 eV) for CS_2, and $I_p = 9.5\,\text{eV}$ (9.3 eV) for CSe_2 [180]. Lastly, note that carbon dichalcogens have a pair of degenerate HOMOs, which can be randomly oriented around the molecular axis; for my orbital-resolved simulations (see Sec. 3.3), I further impose the orientation of the orbitals such that one HOMO lies in the xy-plane ("in-plane"), and the other lies in the xz-plane ("out-of-plane") [110] – see Fig. 3.1(b).

I then apply a linearly-polarized mid-infrared (MIR) laser field in order to drive HHG. The envelope of this laser field has a $\sin^2$ ramp-up for two laser cycles, and then re-

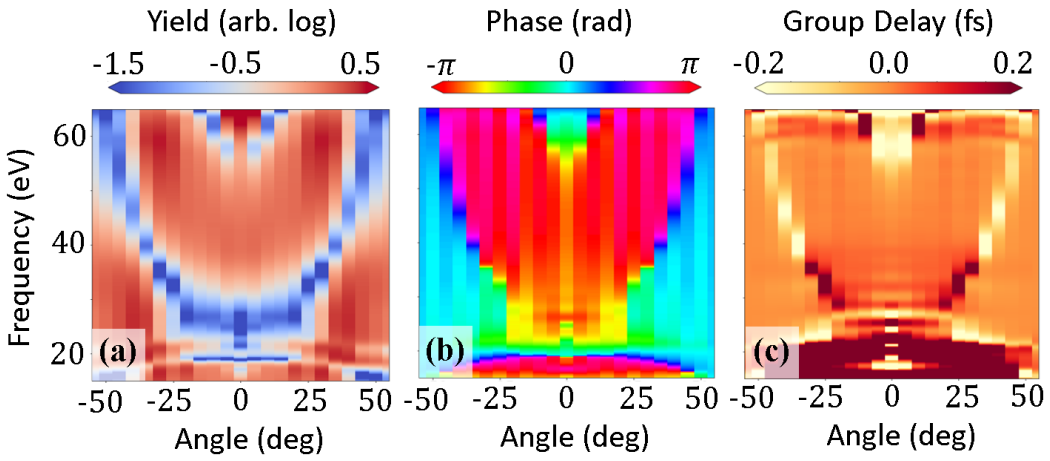

Figure 3.2: Example of the alignment-angle-dependent HHG spectral intensity (a), phase (b), and group delays (c) for CO_2 for a driving laser with a wavelength of 1500 nm and an intensity of 60 TW/cm^2.

mains a continuous wave. The wavelength and intensity of the MIR field will be varied in Sec. 3.5. For some of the calculations shown below, I add a weak attosecond pulse train (APT) ionization seed, meant to select the short-trajectory contribution to the dipole signal; the efficacy of the APT will be investigated in the following section. The APT used here is comprised of odd harmonics, ranging from the 9$^{\text{th}}$ to the 17$^{\text{th}}$ orders, and is synchronized such that its peak is 0.06 cycles after each peak of the MIR [156] – see again Fig. 2.5. Both the MIR and APT laser fields are polarized along the $\hat{x}$-axis, and I scale the APT intensity to 2% of that of the MIR. In all simulations, I use the AETRS time-propagation scheme with a time step of 0.05 atomic units [110].

For a driving laser wavelength of 1500 nm and an intensity of 60 TW/cm^2, examples of the angle-dependent spectral intensity (a), phase (b), and group delay (c) are shown in Figure 3.2. The spectral intensity and phase are taken from Eqs. 2.9 and 2.10; the group delay, related to the spectral phase by a derivative and often what is measured in an ex-

periment, is defined by

$$\tau_{\mathrm{tot}}(\omega) = \frac{\sum_{i=1}^{3}[S_i(\omega)\,\tau_i(\omega)]}{S_{\mathrm{tot}}(\omega)}\ , \quad \text{where } \tau_i(\omega) = -\frac{\partial}{\partial\omega}\varphi_i(\omega) = -\frac{\partial}{\partial\omega}\arg\left(\frac{D_i(\omega)}{D_{\mathrm{ref}}(\omega)}\right) \tag{3.2}$$

The TCI feature manifests as a smooth parabolic feature in all three cases, with a zero-degree TCI energy of around 27 eV. The TCI is a minimum in the spectral intensity, π discontinuity in the phase, and a derivative discontinuity in the group delay. In order to obtain Fig. 3.2, I calculate the alignment-angle-dependent complex dipole signal $\vec{D}[\theta](\omega)$ using the orbital-resolved dipole moment (see again Sec. 2.3.2) from TDDFT simulations in Octopus. From this dipole signal, I extract the relevant intensity and phase information in order to characterize the TCI minimum. Here, I only look at the dipole signal in the direction parallel to the laser polarization, since the harmonic signal in the two perpendicular directions is negligible within the harmonic plateau.

The frequency-dependent overlap (inner product) between the returning EWP in the continuum and the remaining molecular bound wavefunction, called the recombination dipole matrix element (RDME), contains the information relevant to characterizing the TCI minimum. For the target-specific harmonic phase and group delay, the RDME is accessed by using a reference dipole signal D_{ref}, as shown in Eqs. 2.10 and 3.2, respectively. Here, I use the 60-degree HHG signal (treated identically to the angle-resolved signal), because its spectral intensity and phase are essentially featureless in the range of energies that I am interested in here. Note that one could also use the 90-degree signal for normalization.

However, for the spectral intensity in Eq. 2.9, there is no reference dipole signal used; instead, I take inspiration from the semiclassical three-step model [72, 73]. The de-

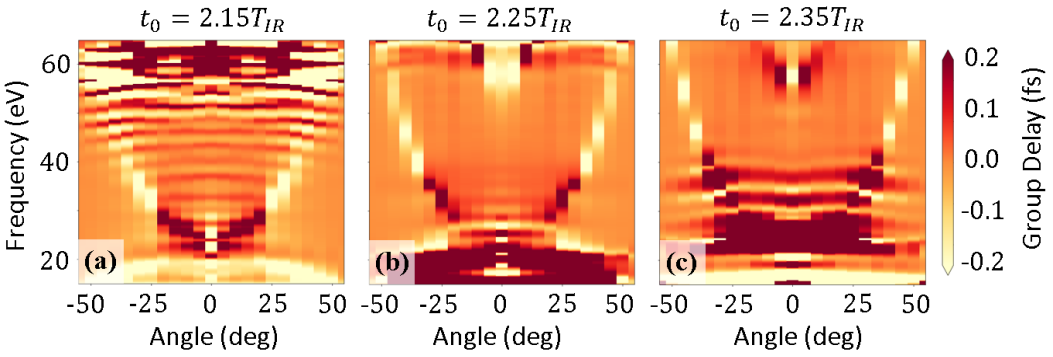

Figure 3.3: Angle-dependent group delays in CO_2 for three different central times used for the half-laser-cycle window $W(t)$: (a) $t_\circ = 2.15\,T_L$, (b) $t_\circ = 2.25\,T_L$, and (c) $t_\circ = 2.35\,T_L$, where T_L is the period of the HHG-driving laser field.

composition of the HHG process into ionization, propagation, and recombination steps which embodies the three-step model, discussed in Sec. 1.3, is not just a conceptual aide; it can also be useful in a mathematical sense [159, 181, 182]:

$$\mathrm{HHG}[\theta](\omega) = \underbrace{\sqrt{I(\theta)}}_{\text{Ion.}}\ \underbrace{\mathrm{HHG}_{\mathrm{avg}}(\omega)}_{\text{Prop.}}\ \underbrace{\mathrm{RDME}[\theta](\omega)}_{\text{Scat.}} \tag{3.3}$$

The aim is to divide through by the ionization yield $I(\theta)$ and the average harmonic signal $\mathrm{HHG}_{\mathrm{avg}}(\omega)$ in order to recover the RDME. Therefore, I first divide each dipole signal by a global ionization-yield factor which depends only on molecular alignment and which I estimate as

$$I(\theta) = \int_{20\,\mathrm{eV}}^{\infty} S[\theta](\omega)\,\mathrm{d}\omega \tag{3.4}$$

where $S[\theta](\omega)$ is the windowed harmonic spectral intensity defined by Eq. 2.9, and I integrate over frequencies not included in the perturbative region of the spectrum. Second, I divide the angle-dependent HHG spectrum $S[\theta](\omega)$ by the angle-averaged spectrum $\mathrm{HHG}_{\mathrm{avg}}(\omega)$, which removes the general structure of the harmonic spectrum and allows us to see the effect of the TCI near the cutoff energy despite the weaker signal.

Lastly, I note that there is some ambiguity in choosing the central time $t_\circ$ used in

the window function $W(t)$ – again, see Eq. 2.12 and the discussion surrounding Fig. 2.4. I wish to choose $t_\circ$ such that there is only one short-trajectory burst in the half-laser-cycle-windowed dipole signal. In Figure 3.3, I show the angle-dependent group delays for varying values of $t_\circ$, where the differences are most noticeable. If $t_\circ$ is too low, interference effects (between two short-trajectory bursts, not the two-center interference I am looking for) muddle the high-energy signal, near the cutoff energy; if $t_\circ$ is too high, the low-energy signal near the ionization potential is muddled by similar interference effects. Thus, I must find a balance which does not disturb the spectral range of interest; this value may be different for different molecular targets (with different ionization potentials), or driving laser wavelengths (different cutoff energies). For the figures shown, the value of $t_\circ$ will be listed in the caption – see also the supplemental data and code corresponding to Ref. [179].

3.3. Validation of Orbital-Resolved HHS

Ordinarily, TDDFT calculations of HHG spectra use the Fourier transform of the total dipole acceleration $\vec{a}(t) = -\langle\Psi| - \nabla V_{\mathrm{KS}}|\Psi\rangle = \frac{\mathrm{d}}{\mathrm{d}t}\int \vec{r}\,\rho(t)$. However, the TDDFT-calculated orbital energies (which can often be inconsistent with experimental data [146, 160]) and symmetries of the HOMO-2 and lower-lying orbitals are such that larger-than-expected multi-orbital effects can be prevalent in the HHG signature of CO_2 [110, 150, 179]. These multi-orbital effects can be quite destructive to imaging a TCI [151, 183–187], which lies only in the HOMO.

Historically, the short-trajectory contribution to the HHG signal was enhanced by including an attosecond pulse train (APT), synchronized with the HHG-driving MIR laser, which replaces tunnel ionization with one-photon ionization – see again Sec. 2.3.1. Despite

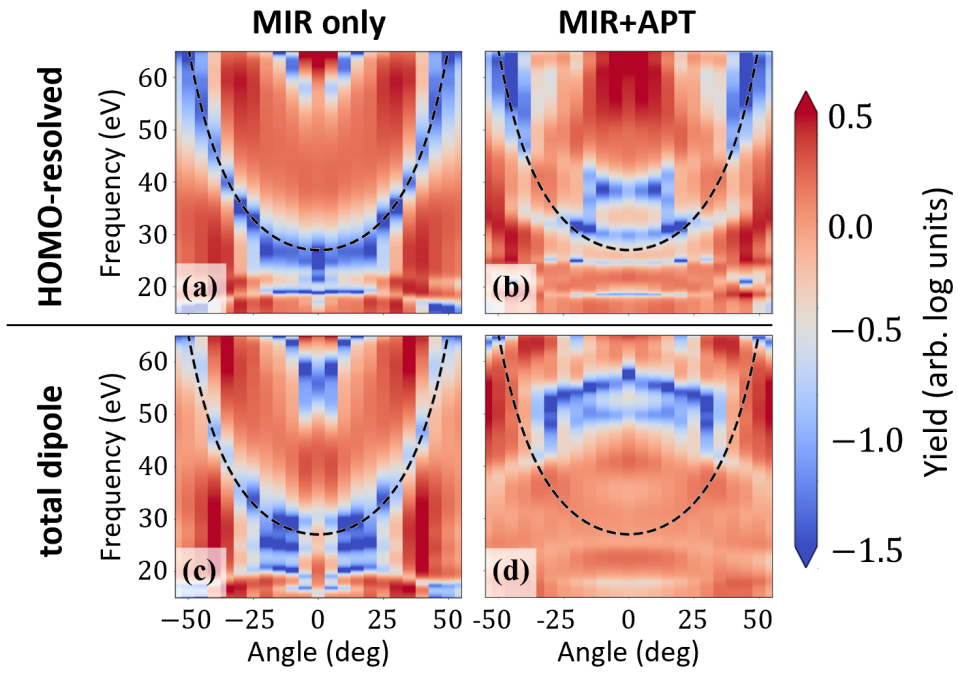

Figure 3.4: Angle-dependent HHG spectra calculated from (a,b) the HOMO-resolved dipole moment and (c,d) the total dipole acceleration. I use either an MIR-only (a,c) or an APT-seeded (b,d) driving laser with $\lambda = 1500\,\text{nm}$ and $I_\circ = 60\,\text{TW/cm}^2$. ($t_\circ = 2.25T_L$ for all panels.)

its advantages, I have found the APT further disproportionately enhances ionization from lower-lying Kohn-Sham orbitals, since tunnel ionization depends much more heavily on the orbital binding energy than one-photon ionization. To alleviate the effects of multiple orbitals in the harmonic signal, I can use the technique of resolving individual Kohn-Sham orbitals as described in Sec. 2.3.1. In Figure 3.4, I look at spectral intensities for MIR-only (a, c) and APT-seeded (b, d) driving lasers calculated from either the HOMO-resolved dipole moment (a, b) or the total dipole acceleration (c, d). The black dashed lines in all panels, taken to be the "true" TCI minimum, is taken from scattering simulations performed in MATLAB, discussed further in Section 3.6.

Considering all four cases in Fig. 3.4, the best scenario for detecting the TCI feature in CO_2 appears to be HOMO-resolved and MIR-only (panel (a)), in which there is

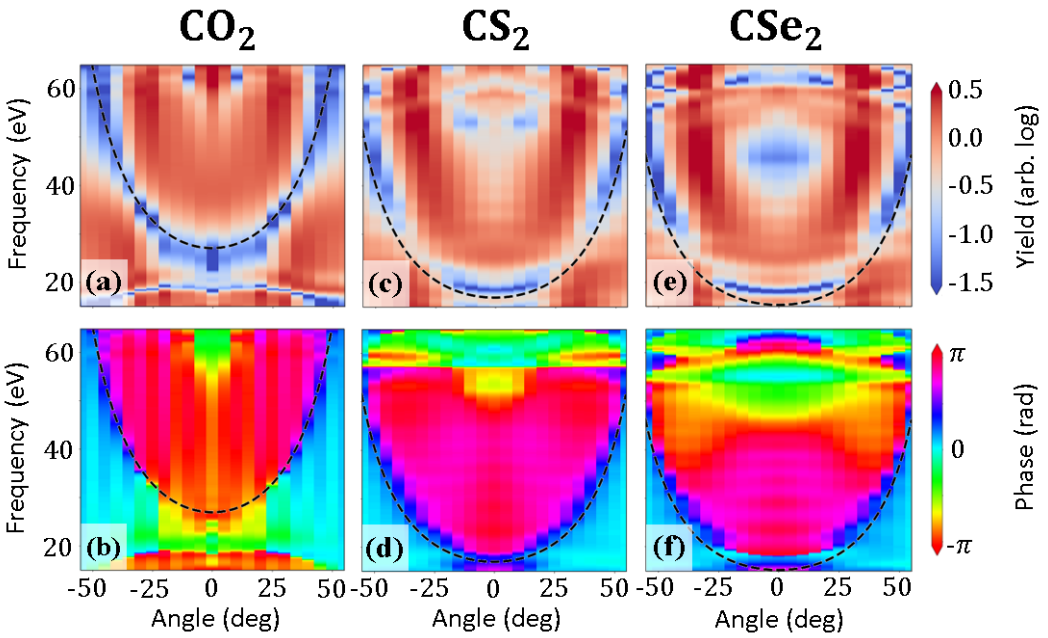

Figure 3.5: Angle-dependent HOMO-resolved HHG spectra (a,c,e) and phases (b,d,f) for CO_2 (a,b), CS_2 (c,d), and CSe_2 (e,f), for $\lambda = 1500\,\text{nm}$ and $60\,\text{TW/cm}^2$. ($t_\circ = 2.22T_L$ for all panels.)

a clear parabolic minimum in the spectral intensity. In both the total-dipole and orbital-resolved cases, the inclusion of the APT greatly obscures the TCI feature in CO_2. These conclusions are also supported by the angle-dependent spectral phases (not shown).

3.4. TCIs in Carbon Dichalcogens

Now that I have extracted the TCI feature using HHS, I perform a systematic investigation of the molecules in the carbon dichalcogen family. Figure 3.5 shows the spectral intensities (a,c,e) and phases (b,d,f) using the HOMO-resolved dipole signal for three different molecules in the carbon dichalcogen family: CO_2, CS_2, and CSe_2. All three molecules exhibit the same qualitative feature in both the spectral intensity and phase, as expected. Comparing the three TCI minima, it is apparent that their zero-degree energies decrease across the family. This trend is expected, since the carbon-chalcogen bond length increases with heavier elements, and the energy of the TCI feature is expected to

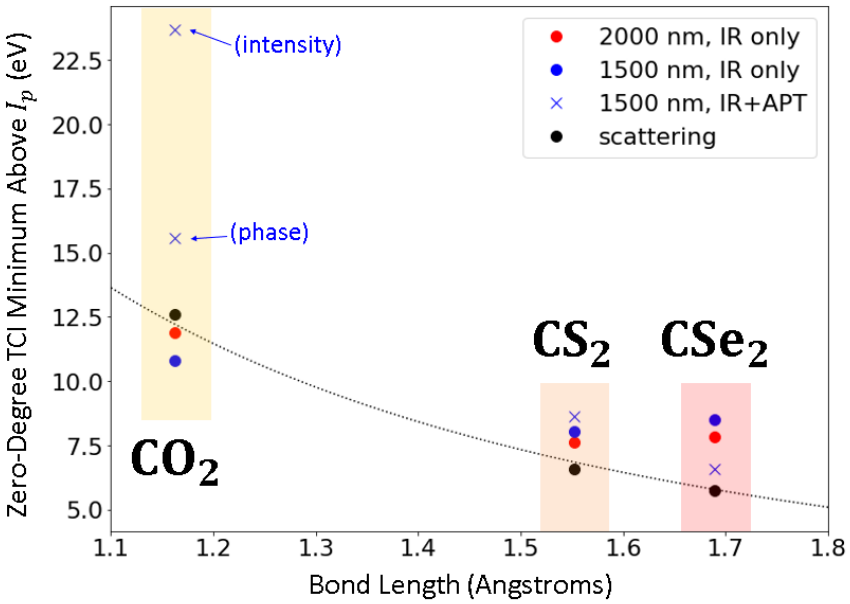

Figure 3.6: Markers: comparison of the TCI minimum in the carbon dichalcogen family for different MIR wavelengths and intensities, as well as scattering simulations – see legend. For each datum, I report the difference between the HHG energy at which the TCI minimum is located at zero degrees and the molecule's ionization potential. The dotted curve is proportional to $1/R^2$, as predicted by scattering theory [157, 165, 184].

qualitatively scale as the inverse of the charge-separation distance squared (see Eq. 3.1). For the phases in Fig. 3.5(b,d,f), we see a clear difference between the value of the phase above and below the TCI. Since the TCI feature results from destructive interference, it is accompanied by a π phase jump [156]. This transition, as a function of alignment angle θ, is entirely consistent with the features shown in the spectral intensities in (a,c,e); compare, for instance, the dashed lines in both plots.

In Fig. 3.6, I show the location of the zero-degree minima for the three molecules, plotted versus the carbon-chalcogen bond length R, for a number of different pulse parameters. The location has been extracted from the data shown in Fig. 3.5 as the energy of the deepest minimum of the zero-degree spectral intensity. I also show the location of the minimum extracted from my scattering calculations (see Sec. 3.6) as well as a fit propor-

tional to $1/R^2$, which is what one would expect for plane-wave scattering of the returning wave packet on two centers separated by a distance R. The small variation between the different IR-only extracted results, as well as the good agreement with the scattering results, provides a measure of the accuracy of the HHS-based approach. The APT-seeded results for CS_2 and CSe_2 also agree well with the other results; however, for CO_2 the APT-seeded results are substantial outliers, something which has been noted elsewhere [150, 152, 179, 186]. Taken together, these results also illustrate the benefits of comparing spectral features across multiple dimensions [171, 179, 188] – here, the parameters of the laser field and the molecular targets within the carbon-dichalcogen family – to identify both generic spectroscopic features that can be compared against each other as well as signatures that are unique to each system.

3.5. Wavelength and Intensity Dependence of the TCI

While the first experimental measurement of the spectral minimum in CO_2 in 2005 [167] attributed the feature to a two-center interference in the doubly-degenerate HOMO, later studies [150, 152, 158, 186] reinterpreted this result as an interference between HHG signals from the HOMO and HOMO-2 orbitals. In recent years, the consensus is that both of these mechanisms are at play, depending on the wavelength and intensity of the HHG-driving laser. This claim was rigorously tested in collaboration with The Ohio State University in Ref. [179]. This was done by taking simultaneous measurements of the spectral intensity and phase of harmonic radiation generated in CO_2 at different driving wavelengths and intensities, and comparing them with TDDFT simulations performed in Octopus (the computational details of which have been discussed above).

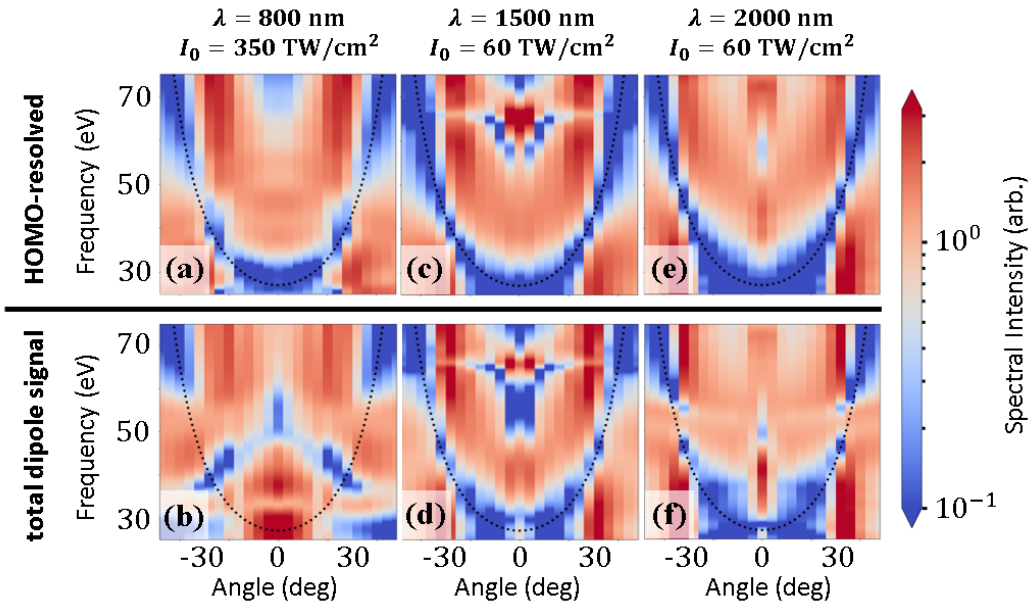

Figure 3.7: Angle-dependent spectral intensities for (a,b) $\lambda = 800\,\text{nm}$, $I_\circ = 350\,\text{TW/cm}^2$; (c,d) $\lambda = 1500\,\text{nm}$, $I_\circ = 60\,\text{TW/cm}^2$; and (e,f) $\lambda = 2000\,\text{nm}$, $60\,\text{TW/cm}^2$, calculated from both the HOMO-resolved dipole signal (a,c,e) and the total dipole acceleration (b,d,f).

In Figure 3.7, I plot the (a-c) HOMO-only and (d-f) total HHG spectra for three different wavelengths: 800, 1500, and 2000 nm. Again, the dotted lines correspond to scattering calculations, discussed in the following section. For the HOMO-resolved HHG spectra, the three driving wavelengths show a qualitatively similar yield to the experimental results with a parabolic minimum which shifts to higher energies as the molecule is rotated away from parallel to the laser polarization. However, the zero-degree energy is quite different from the experiment (33 eV here as opposed to 47 eV in the experiment), likely due to the use of an LDA exchange-correlation functional. The uniformity of Figs. 3.7(a-c) suggest that the structural shape of the feature is wavelength- and intensity-independent, consistent with a static TCI minimum. By contrast, the total HHG spectrum in panel (d) is dramatically different from that of its HOMO-resolved complement in (a); here, multi-orbital effects from the HOMO-2 and lower-lying orbitals have completely washed out the

TCI minimum. The total HHG spectra for 1500 and 2000 nm (e,f), however, are quite consistent with (b,c) – this suggests that other orbitals do not play a significant role in the HHG process at those wavelengths. This behavior is reflected also in the spectral phase measurements shown in Figure 3.8.

The simulation results shown in Figs. 3.7 and 3.8 are in good agreement with the experiment [179]: for 800 nm, multi-channel interferences play an important role in the observed spectral feature, while for longer wavelengths, the influence of the HOMO-2 fades and the TCI minimum is the predominant interference mechanism. It was found that a wavelength of approximately 1200 nm was the turning point between the two mechanisms, though the exact wavelength where the interplay between interference mechanisms is observed depends heavily on the degree of alignment (which strongly governs the ratio of yields between the HOMO and HOMO-2), the magnitude of the interference, and the energetic location of the spectral feature.

3.6. Field-Free Scattering Simulations

As discussed in Sec. 2.3, the rescattering step of HHG imprints the recombination dipole matrix element (RDME) onto the harmonic signal [110, 179]. I have already examined how to extract the RDME from the dipole acceleration obtained from TDDFT simulations, via careful normalization. Instead, I propose to achieve a similar result by taking a user-defined scattering seed and throwing it at the bound wavefunction in order to calculate the RDME directly. A schematic of my scattering simulations is shown in Figure 3.9. Within the ground-state DFT potential $V_{\mathrm{KS}}(\vec{r})$, a scattering seed $|\phi_s\rangle$ in the continuum travels towards the field-free out-of-plane HOMO $|\phi_k^{\mathrm{MO}}[\theta]\rangle$ of a carbon dichalcogen

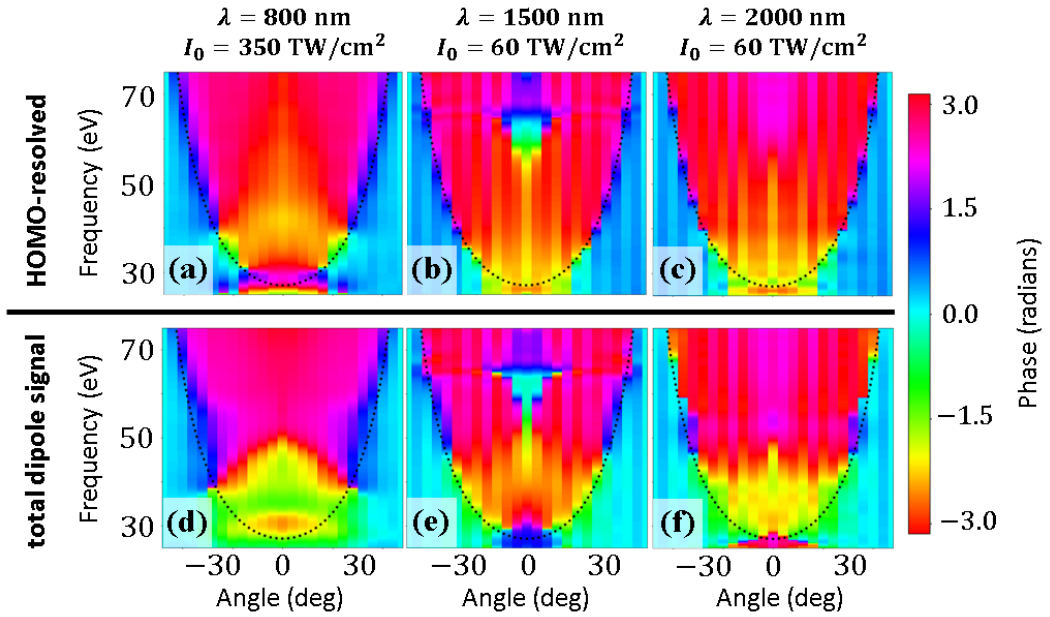

Figure 3.8: Angle-dependent spectral phases for (a,b) $\lambda = 800\,\text{nm}$, $I_\circ = 350\,\text{TW/cm}^2$; (c,d) $\lambda = 1500\,\text{nm}$, $I_\circ = 60\,\text{TW/cm}^2$; and (e,f) $\lambda = 2000\,\text{nm}$, $60\,\text{TW/cm}^2$, calculated from both the HOMO-resolved dipole signal (a,c,e) and the total dipole acceleration (b,d,f).

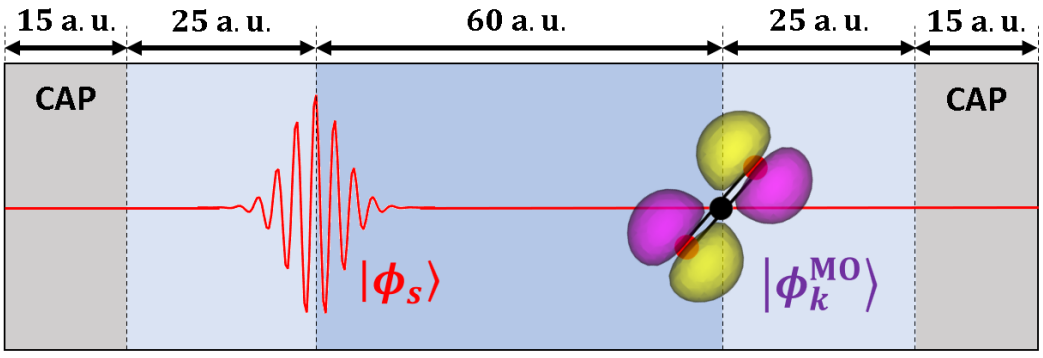

Figure 3.9: Schematic of my scattering simulations. A scattering seed $|\phi_s\rangle$ propagates towards the field-free out-of-plane HOMO $|\phi_k^{\text{MO}}[\theta]\rangle$, immersed in the ground-state Kohn-Sham potential $V_{\text{KS}}(\vec{r})$.

molecule, where the TCI minimum resides. In the field-free case, I can formally calculate the time evolution of an arbitrary wave packet without explicitly computing any scattering states, which is a non-trivial process for arbitrary potentials [110, 189].

In Sec. 3.3.6.1, I go into the mathematical details of how these scattering simulations are performed. In Sec. 3.3.6.2, I present the results from my scattering simulations of TCIs in carbon dichalcogens, to be compared to the full TDDFT results in Fig. 3.5.

3.6.1. Methodology

Here, I am looking for the recombination dipole matrix element (RDME), defined by $\langle\phi_s|\hat{x}|\phi_k^{\mathrm{MO}}\rangle$, where $|\phi_s\rangle$ is a user-defined scattering seed, and $|\phi_k^{\mathrm{MO}}\rangle$ is the bound molecular orbital with an orbital energy $-I_p^k$, which acts as the scattering target, as illustrated in Fig. 3.9.

Consider the orthonormal set of wavefunctions $\{|\phi_{\mathrm{sc}}\rangle\}$ such that

$$\left(-\frac{1}{2}\nabla^2 + V_{\mathrm{KS}}(r)\right)|\phi_{\mathrm{sc}}\rangle = \frac{p^2}{2}\,|\phi_{\mathrm{sc}}\rangle \;\;, \quad \text{where } V_{\mathrm{KS}}(r) \propto \frac{1}{r} + \mathcal{O}(r^{-2}) \tag{3.5}$$

The above scattering wavefunctions are target-specific, since $\mathcal{O}(r^{-2})$ above depends on the molecular structure and orientation. I can formally decompose the scattering seed $|\phi_{\mathrm{s}}\rangle$ in momentum space, initially localized away from the core, as

$$\phi_s(\vec{r}, t=0) \approx \int w(\vec{p}) \cdot \phi_{\mathrm{sc}}[\theta, \vec{p}](\vec{r})\,\mathrm{d}\vec{p} \tag{3.6}$$

I would like to analytically calculate the field-free time-dependent dipole signal, but I do not know the mathematical form of the scattering states $\{|\phi_{\mathrm{sc}}\rangle\}$ due to their target-specificity. However, far away from the molecular core (as $r \gg 1$), the Kohn-Sham potential V_{KS} converges to something which is proportional to $1/r$ (the Coulomb tail). Therefore, since the scattering seed is initially far away from the molecule, I assume that the

coefficients $w(\vec{p})$ in Eq. 3.6 are independent of the molecular alignment, parameterized by the angle θ. Thus, in the above factorization, the weight distribution $w(\vec{p})$ is solely determined by $|\phi_s\rangle$, while all of the information associated with the specifics of the molecular target are contained in the scattering states $\{|\phi_{\rm sc}\rangle\}$.

In a practical sense, for the scattering simulations, I know the initial scattering seed $\phi_s(\vec{r}, t = 0)$ and seek to cancel out the weights $w(\vec{p})$ in order to access the RDME without ever explicitly computing either $w(\vec{p})$ or $\phi_{\rm sc}(\vec{r})$. Since $|\phi_k^{\rm MO}\rangle$ and $|\phi_{\rm sc}\rangle$ are eigenstates of the Kohn-Sham potential $V_{\rm KS}(\vec{r})$ (bound and continuum, respectively), I know their explicit time dependence since there is no time-dependent laser field:

$$|\phi_k^{\rm MO}(t)\rangle = \exp\left[-iI_p^k t\right] |\phi_k^{\rm MO}(0)\rangle \qquad\qquad |\phi_{\rm sc}(t)\rangle = \exp\left[i\frac{p^2}{2}t\right] |\phi_{\rm sc}(0)\rangle \tag{3.7}$$

Thus, using Eqs. 3.6 and 3.7 above, I can formally write the time-dependent dipole matrix element as

$$d_k^{\rm sc}(\theta, t) = \langle\phi_s(t)|\hat{x}|\phi_k^{\rm MO}(t)\rangle + \text{c.c.} \tag{3.8}$$

$$\Downarrow\ \phi_s(\vec{r},\, t) = \int w(\vec{p}) \cdot \phi_{\rm sc}[\theta, \vec{p}](\vec{r})\, \exp\left[-\frac{1}{2}ip^2 t\right]\, \mathrm{d}\vec{p}$$

$$= \int w^*(\vec{p}) \cdot \langle\phi_{\rm sc}[\theta, \vec{p}]|\hat{x}|\phi_k^{\rm MO}(0)\rangle\, \exp\left[i\left(I_p^k + \frac{p^2}{2}\right)\, t\right]\, \mathrm{d}\vec{p} + \text{c.c.} \tag{3.9}$$

where c.c. denotes the complex conjugate. The term $w(\vec{p})\ \langle\phi_{\rm sc}|\hat{x}|\phi_k^{\rm MO}(0)\rangle$ is time-independent, and thus $d_k^{\rm sc}$ in Eq. 3.9 looks like a Fourier expansion at the frequencies $\omega \equiv I_p^k + \frac{p^2}{2}$. Thus, taking the Fourier transform of the scattering dipole is proportional to the RDME:

$$\mathcal{F}[d_k^{\rm sc}(\theta, t)](\omega) \propto \text{RDME}_k(\theta, \omega) \tag{3.10}$$

The only unknown factor here is the weight distribution $w(\vec{p})$. As mentioned, if the scat-

tering seed is sufficiently far away from the target wavefunction at $t = 0$ (if $r \gg 1$), then $w(\vec{p})$ is identical for wavefunctions with a Coulomb tail given a scattering seed $|\phi_s\rangle$. Thus, I can remove $w(\vec{p})$ by normalizing the scattering-seed results with a reference set of parameters:

$$\mathrm{RDME}_k(\theta, \omega) = \frac{\mathcal{F}[W(t) \times d_k^{\mathrm{sc}}(\theta, t)](\omega)}{\mathcal{F}[W(t) \times d_{\mathrm{ref}}^{\mathrm{sc}}(t)](\omega)} \tag{3.11}$$

As with my full TDDFT HHS calculations, I require that both ends of the dipole signal $d_k^{\mathrm{sc}}[\theta](t)$ go to zero. Since the scattering seed and molecular target wavefunction start so far apart, $d_k^{\mathrm{sc}}(t = 0)$ is already zero; thus, I multiply the dipole signal by a broad time window $W(t)$ equal to 1 for the beginning of the scattering simulation and then goes to 0, with a $\cos^6$ shape, at the end of the simulation duration. This result can then be treated like a normalized complex dipole signal in Eqs. 2.9 and 2.10.

In practice, I define a scattering seed $|\psi_s\rangle$ of the form

$$\phi_s(\vec{r}, t = 0) = \mathcal{N}_{\parallel}(x - x_\circ)\, \mathcal{N}_{\perp}(y, z) \cdot e^{ip_\circ x} \tag{3.12}$$

where $x_\circ$ is the initial central position of the scattering seed, and $p_\circ$ is the initial momentum in the $+\hat{x}$ direction. The parallel term $\mathcal{N}_{\parallel} e^{ip_\circ x}$ emulates the wave front along the scattering direction of the rescattering electron in HHG – similar to the plane wave in Fig. 3.1. The parameters $x_\circ$, $p_\circ$, and $\mathcal{N}_{\parallel}$ must be chosen such that none of the scattering seed propagates backwards (in the $-\hat{x}$ direction). One final detail to consider is that the symmetry of the target molecular orbital is carried over to the outgoing EWP at ionization (and thus rescattering). I account for this by choosing the transverse component $\mathcal{N}_{\perp}$ such that its shape reflects the symmetry of the outgoing EWP resulting from strong-field ionization. For example, in the case of the out-of-plane HOMO of CO_2, as is shown in Fig. 3.9, the

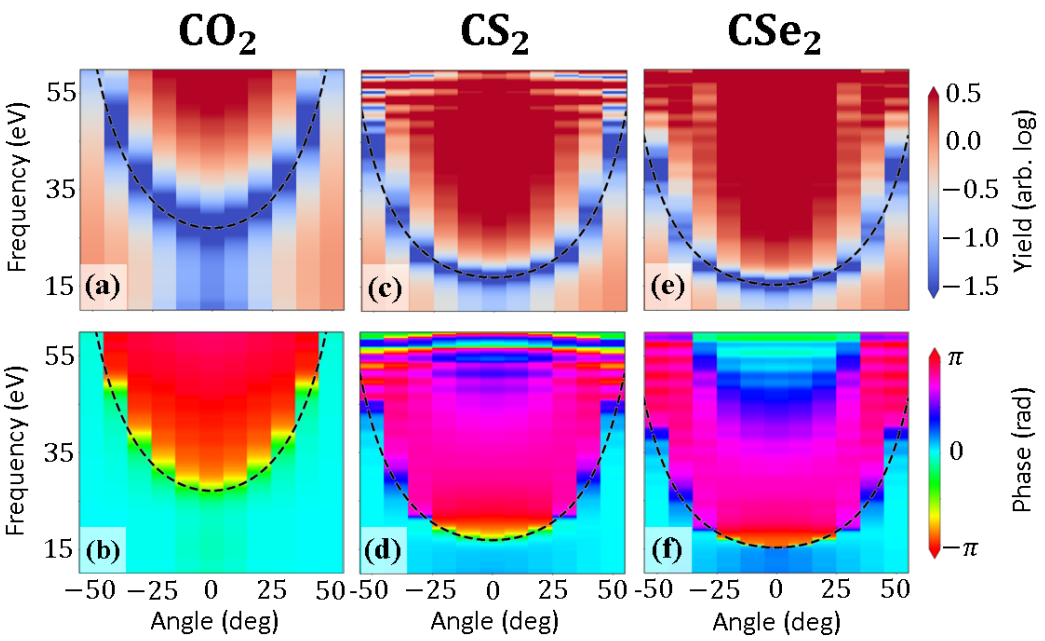

Figure 3.10: Field-free scattering simulations, for the out-of-plane HOMO, in the carbon-dichalcogen family. I show the angle-resolved target-specific intensities (a,c,e) and phases (b,d,f) for CO_2 (a,b), CS_2 (c,d), and CSe_2 (e,f). ($t_\circ = 2.25T_L$ for all panels.)

outgoing EWP has a nodal plane at $z = 0$, which is accounted for in the following section.

3.6.2. Results/Comparison with TDDFT

My computational approach to the scattering simulations is similar to that of the full TDDFT simulations, described in Section 3.1. I again put the carbon-dichalcogen target (more specifically, the out-of-plane HOMO of such – see again Fig. 3.9) at the origin of the simulation box and impose alignment by rotating the the molecule inside the box. In all scattering simulations, I use an initial scattering seed of the form given in Eq. 3.12, with a central position $x_\circ = -60\,\text{a.u.}$ and a central momentum $\vec{p}_\circ = 1.21\,\text{a.u.}$ ($\approx 20\,\text{eV}$) in the positive x-direction. The in-plane component $\mathcal{N}_\parallel$ is a Gaussian function in the x direction, with a width of $\sigma = 0.3\,\text{a.u.}$, and I take $\mathcal{N}_\perp(y,z) = (L_z/2\pi)\sin(2\pi z/L_z)$, where L_z is the total length of the simulation box in the direction of the lobes of the HOMO. Note that $\mathcal{N}_\perp(y,z)$ here applies only because I am using the out-of-plane orbital; if I was scat-

tering off of the in-plane orbital, I would need to replace z with y in the above expression.

In the scattering simulations, performed in MATLAB, I propagate in time a scattering seed $|\phi_s\rangle$ in the DFT ground-state potential $V_{\mathrm{KS}}(\vec{r})$ (which I export from Octopus) using a second-order spectral-split scheme with a time step of 0.01 a.u. for about 3 femtoseconds. With my box and initial-seed parameters, this ensures that the entire scattering wave packet $|\phi_s\rangle$ can travel through the target $|\phi_k^{\mathrm{MO}}\rangle$. To enhance the signals' spectral resolution, in the computation of the scattering dipole components I artificially shift the molecular orbital's ionization potential to a higher energy value, which I then compensate for in Eq. 3.9. Spatially, I use a rectangular domain elongated along the scattering direction x, similar to the full TDDFT simulations. I impose absorbing boundary conditions in the scattering direction and periodic boundary conditions in the other directions. On both ends of the domain I leave a buffer of about 40 a.u. along, and 30 a.u. transversely to, the scattering direction between the faces of the box and the centers of both the molecule and the initial ionization seed. Finally, I use the 0.3 a.u. discretization step in all directions, same as for my TDDFT simulations.

In Fig. 3.10, I show the results of the scattering simulations described above for the out-of-plane HOMO in the carbon dichalcogen family. Overall, these are strikingly similar to the TDDFT MIR-only HHS results with a clear local minimum in the spectral intensity that moves to higher energies with increasing the alignment angle – compare with Fig. 3.5, for both the spectral intensities and phases. Note that, for small alignment angle, the CS_2 and CSe_2 TCI features are close to the ionization threshold and it is therefore more challenging to accurately extract the phase information, which explains the small strip of negative phase around 20 eV in Figs. 3.10 (e) and (f). The location of the zero-degree mini-

mum is also consistent with my TDDFT MIR-only findings, as shown in the dashed lines in Fig. 3.5 and the black dots in Fig. 3.6.

Chapter 4. High-Harmonic Sideband Spectroscopy

In this chapter, I simulate charge migration (CM) dynamics with grid-based TDDFT, and then apply the principles of high-harmonic spectroscopy (HHS, discussed in Sec. 2.3) to probe that dynamics. First, I have found that creating a localized outer-valence hole on the halogen end of a bromobutadiyne (BrC_4H) molecule causes a particle-like motion of the electron hole along the molecular backbone with a fundamental CM frequency of $\omega_{\mathrm{CM}} = 1.845\,\mathrm{eV}$. By applying an HHG-driving laser field that is polarized perpendicular to the molecular backbone, I can independently probe the CM dynamics without driving it. I have found that the periodic modulation of the time-dependent electron density caused by the CM gives rise to a beat in the time-dependent harmonic yield since the laser and CM frequencies are in general incommensurate. This beat leads to sidebands in the resulting harmonic spectrum, which can be used to determine the underlying fundamental CM frequency.

In Sec. 4.1, I discuss experimental efforts to measure CM using various techniques, and make the case for HHS. The initial condition I use for particle-like CM, how I obtain it, and what the resulting CM looks like, is discussed in Sec. 4.2. The emergence of sidebands within the harmonic spectrum is presented and explained in Sec. 4.3, and the methodology I use to characterize the CM dynamics using the location of these sidebands is discussed in Sec. 4.4. In Sec. 4.5, I define a model calculation which reproduces the sidebands I find in the full TDDFT calculations; in Sec. 4.6, I discuss the experimental viability of my approach.

4.1. Introduction

As discussed in Sec. 1.2, charge migration (CM) is the motion of a positively-charged electron hole along the backbone of a molecule following a localized ionization. Now, I wish to use the foundations laid in the previous chapter to first simulate and subsequently probe periodic, particle-like CM using high-harmonic spectroscopy (HHS). However, the first task at hand is to determine which molecules are a suitable platform for this type of CM. As discussed in Ref. [35], double- and triple-bonded molecules can often support robust CM that progresses via hopping from π bond to π bond. Though this conjugation requirement had previously been observed [28, 190–192], our research group was the first to systematically study this phenomenon in families of molecules using first-principles calculations in NWChem [193–195]. Then, leveraging tools from nonlinear dynamics [196, 197], we used frequency-map analysis [198] to study this type of coherent CM [18]. While previous studies [23, 25, 33, 49] invoked the beating between a few molecular orbitals as the underlying mechanism for CM, we found that periodic modes of CM emerge as solitary waves [18, 199] which represent a balance between dispersion and non-linear, time-dependent multi-electron interactions. Furthermore, we found that a single molecule can robustly support several different CM modes, with periods varying by several hundred attoseconds. We have also spent considerable time trying to relate the metrics of CM (time, length, speed, and contrast) to simple attochemistry principles, such as electron donating strength [35, 39].

Though symmetric conjugated molecules like diacetylene can also support facile CM modes [18], adding a heavy halogen like bromine or iodine [35] allows for the creation

of a site-specific localized electron hole via either strong-field ionization (SFI) [200–203] or X-ray inner-shell ionization [204–206]. Previous studies [42, 61, 207] have shown that a core-level ionization event causes a localized shake-up in the valence shell due to the Auger effect. However, TDDFT is known to have challenges when using adiabatic exchange-correlation functionals to drive systems far from equilibrium [208–212]. Though efforts have been made to incorporate the ionization step into existing quantum chemistry codes [15, 53] (including my own [213] – see Sec. 6.4), we instead emulate the creation of a localized electron hole using constrained density-functional theory (cDFT) [214–218] by using an energy-minimization procedure to put the molecule in an intricate superposition of cationic states at some initial time [66] which mimics a site-specific outer-valence ionization.

Once a mode of periodic CM has been identified, I want to characterize the dynamics using HHS [66]. Despite the challenges of experimental control at the attosecond timescale, CM has been detected in several measurements [14, 33, 34, 65, 219–221], many of them very recent [55, 61, 67, 68, 222–226]. The majority of these have documented a modulation of in the double-ionization signal of a molecular fragment following ultrafast photoionization. These delay-dependent variations have been ascribed to CM, with theory showing similar modulations in the populations of cationic states [14, 33, 49, 55, 221]. Two of these experimental studies [34, 67] employ self-probing HHS, where the ionization and recombination steps of the HHG process were used to initiate and probe the CM, respectively. Accordingly, the CM dynamics was re-initiated in each half-laser-cycle, and therefore did not manifest in a straightforward modulation. Instead, these experiments heavily relied on theory computations to validate and interpret their results. Other studies

have used attosecond pump-probe spectroscopy [221] or attosecond transient absorption spectroscopy (ATAS) [222], to similar effect.

Here, I introduce high-harmonic sideband spectroscopy (HHSS), a robust probe of CM that uses HHS as an independent probe step following a CM-inducing pump. The HHG-driving laser field is perpendicular to the molecular backbone so that it does not drive the CM dynamics. This CM dynamics, initiated by the creation of a localized hole, leads to a coherent modulation of time-dependent HHG yield produced by a delayed probe pulse, and I demonstrate how to extract detailed information about the characteristics of the CM motion [66]. By varying the driving laser wavelength, I can very precisely obtain the CM frequency (see Sec. 4.4).

4.2. Initial Condition using Constrained DFT

Though efforts have been made to perform cDFT calculations on a real-spaced grid [19], Octopus does not natively have the ability to perform cDFT calculations like the ones done in Ref. [35]. Thus, I instead import the initial condition, represented by a wavefunction $|\psi_{\oplus}\rangle$ (the cDFT HOMO obtained from NWChem), by taking a linear combination of the ground-state molecular orbitals $\{|\chi_k\rangle\}$ from Octopus [66]. However, $|\psi_{\oplus}\rangle$ cannot be reproduced exactly since the set of wavefunctions available to NWChem is different from that of Octopus (and both are incomplete sets). Thus, the reconstructed target $|\psi_{\mathrm{CM}}\rangle$ is defined by

$$|\psi_{\mathrm{CM}}\rangle = \sum_{k=1}^{N} \langle\chi_k|\psi_{\oplus}\rangle\,|\chi_k\rangle \tag{4.1}$$

where $\{|\chi_k\rangle\}$ and $|\psi_{\oplus}\rangle$ are all normalized. A good measure of the accuracy of this reconstructed target wavefunction with respect to the original is simply $\langle\psi_{\mathrm{CM}}|\psi_{\oplus}\rangle$.

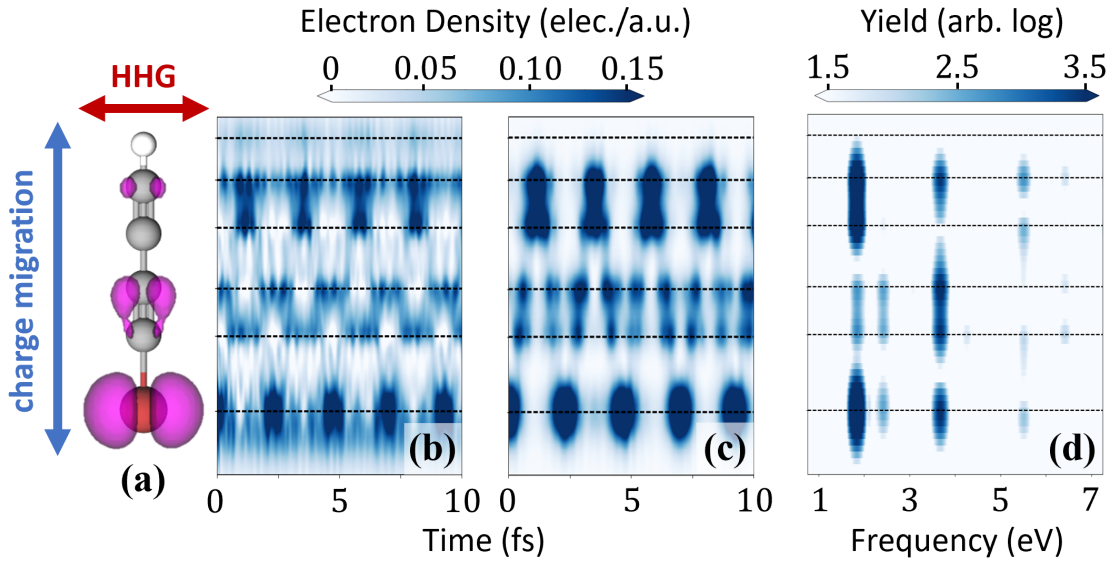

Figure 4.1: (a) Schematic of HHSS configuration to probe CM in BrC_4H. The HHG driving field is polarized perpendicular to the molecular backbone along which the periodic CM occurs. I also show the isosurface of the electron density contribution from the unpaired Kohn-Sham channel in which I introduce the initial localized-hole perturbation. (b) Time evolution of the electron density contribution from (a), integrated over the directions transverse to the molecular backbone, as a function of position. (c) Fourier transform of the time-dependent dynamics in (b).

However, directly replacing $|\chi_1\rangle$ with $|\psi_{\mathrm{CM}}\rangle$ would have devastating effects on the remainder of the basis, since the set would no longer be orthonormal. Thus, I instead obtain a unitary transformation matrix $\hat{U}$ that transforms $\{|\chi_k\rangle\}$ to a new orthonormal basis set $\{|\psi_k\rangle\}$; to this end, the coefficients $\langle\chi_k|\psi_\oplus\rangle$ in Eq. 4.1 are important, since they are the first row in $\hat{U}$. In order to find the remainder of $\hat{U}$, I use the Gram-Schmidt orthonormalization procedure outlined in several quantum mechanics textbooks (*i.e.* Ref. [227]). Briefly, the state $|\psi_k\rangle$ is given by

$$|\psi_k\rangle = |\chi_k\rangle - \sum_{j=1}^{k-1} \langle\psi_j|\chi_k\rangle\,|\psi_j\rangle \ , \qquad k = 2\ldots N \tag{4.2}$$

Thus, having found $\{|\psi_k\rangle\}$, I can obtain the transformation matrix U:

$$U_{ij} = \langle\chi_i|\psi_j\rangle \ \forall\ i,\ j \tag{4.3}$$

where $|\psi_1\rangle \equiv |\psi_{\mathrm{CM}}\rangle$. At this point, one should confirm that the resulting transformation matrix $\hat{U}$ is unitary by checking that $\hat{U}^\dagger\hat{U} = \hat{1}$. Using this method, I am able to reproduce the cDFT-localized electron hole from NWChem with greater than 99% accuracy ($\langle\psi_{\mathrm{CM}}|\psi_\oplus\rangle > 0.99$). This matrix can be directly imported into Octopus via the `TransformStates` block; then, one electron can be removed from $|\psi_{\mathrm{CM}}\rangle$ using the `Occupations` block, inducing periodic CM in the target molecule.

For the molecules considered here, such as bromobutadiyne, I am mainly interested in the electron hole density integrated in the directions transverse to the molecular backbone, here defined to be along the z-axis:

$$\rho_h(z,t) = \iint \mathrm{d}x\,\mathrm{d}y\,\rho_h(\vec{r},t) \tag{4.4}$$

In Figure 4.1, I show (a) the unpaired Kohn-Sham orbital density $|\psi_{\mathrm{CM}}(\vec{r},0)|^2$

which I use as the initial condition for periodic CM (which I will call the CM orbital), as well as the resulting field-free dynamics in both the time (b,c) and frequency (d) domains. More specifically, I plot the electron hole density $\rho_h(z,t)$ defined in Eq. 4.4 in panel (b), as well as the time-dependent CM orbital density $|\psi_{\mathrm{CM}}(z,t)|^2$ (again, integrated over the x and y directions) in panel (c). The total electron hole density in (b) has high-frequency artefacts related to the creation of the initial condition which do not appear in panel (c). In both cases, however, starting on the halogen atom, the electron hole migrates to the middle triple bond, then to the terminal triple bond, and then back again in about 2.2 fs, yielding a fundamental CM frequency of 1.83 ± 0.05 eV. In the absence of nuclear motion, this CM dynamics persists for several tens of femtoseconds. The position-dependent Fourier transform of the CM dynamics in panel (c), shown in (d), is also very interesting: in addition to this fundamental CM frequency ω_{CM}, there are also features at $2\omega_{\mathrm{CM}}$ and $3\omega_{\mathrm{CM}}$, consistent with the mechanism for CM discussed in Ref. [18]. In particular, the $2\omega_{\mathrm{CM}}$ component is most easily seen in panel (c) near the middle triple bond, where the electron hole has to travel through twice per CM cycle. Moreover, there is a feature at 2.4 eV which is not a part of the harmonic comb, likely due to the *ad hoc* creation of the initial electron hole.

4.3. Emergence of Sidebands

Without pump-initiated CM (thin red curve in Figure 4.2), I observe well-resolved odd-harmonic peaks, as expected. By contrast, the solid blue curves showing the HHG spectra with CM for two different wavelengths (1575 and 1800 nm) exhibit additional peaks located between the harmonic orders. These *sidebands* are caused by the CM mo-

tion along the molecular backbone. This periodic modulation gives rise to a beat in the time-dependent harmonic yield since the laser and CM frequencies ω_L and ω_{CM} are in general incommensurate. As illustrated in Fig. 4.2, the location, strength, and number of sidebands depend on the driving laser frequency relative to the CM frequency. Thus, the CM-driven modulation of the HHG signal is a clear and background-free probe of the CM dynamics. Note that any potential MIR-triggered CM is re-initiated every half cycle and therefore contributes only to the signal at the odd-harmonic frequencies. Also, here I have chosen a consistent value for the sub-cycle delay between the phase of the driving laser field and the CM (defined formally in Sec. 5.2) in my TDDFT simulations; but, in an experiment, this delay does not need to be controlled since I am always calculating a multi-cycle-windowed high-harmonic spectrum in order to detect sidebands.

Working in the frequency domain, I show that the energies of these sidebands can be used to directly measure the fundamental frequency of the CM mode. To that end, I track the energy separation between each sideband and its nearest odd harmonic. Since the sideband amplitudes vary considerably across the harmonic plateau, I use a stacked spectrum obtained by averaging over $2\omega_L$-wide slices taken from the entire spectrum above 20 eV. For a driving laser wavelength of 1575 nm, the stacking process is illustrated in Figure 4.3(a) using the slices associated with harmonics 83 to 87, and the corresponding stacked spectrum is shown in (b). This stacked spectrum clearly shows two sideband peaks to the right of the central odd harmonic, marked by SB_1 and SB_2. The frequencies of SB_1 and SB_2 are given by

$$\Delta\omega_1 = \pm(\omega_{\mathrm{CM}} - 2\omega_L) \ , \qquad \Delta\omega_2 = 2 \cdot \Delta\omega_1 \tag{4.5}$$

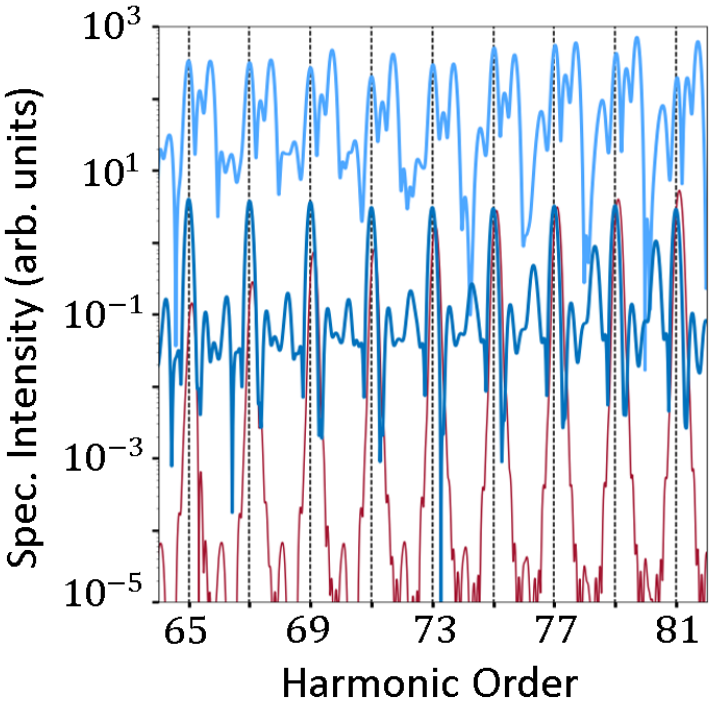

Figure 4.2: Multi-cycle HHG spectra for 1575 nm (top light blue) and 1800 nm (middle dark blue) driving wavelengths. The bottom thin red curve shows the 1800 nm spectrum in the absence of CM (in the neutral molecule). For clarity, the light blue curve is offset by a factor of 200.

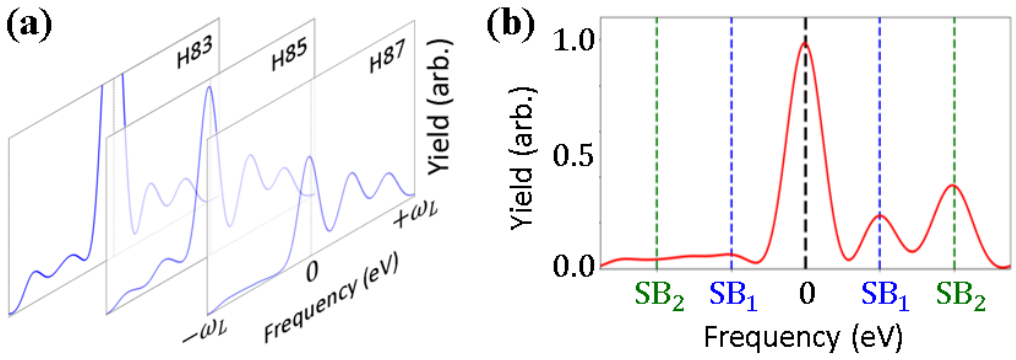

Figure 4.3: (a) Schematic of the stacking process I use to produce the stacked sideband spectrum, where I average $2\omega_L$-wide slices of the relevant HHG spectrum centered around successive odd harmonics. (b) Stacked HHG spectrum around one odd harmonic at 1575 nm. Sideband peaks 1 and 2, above and below the odd harmonic peak, are marked.

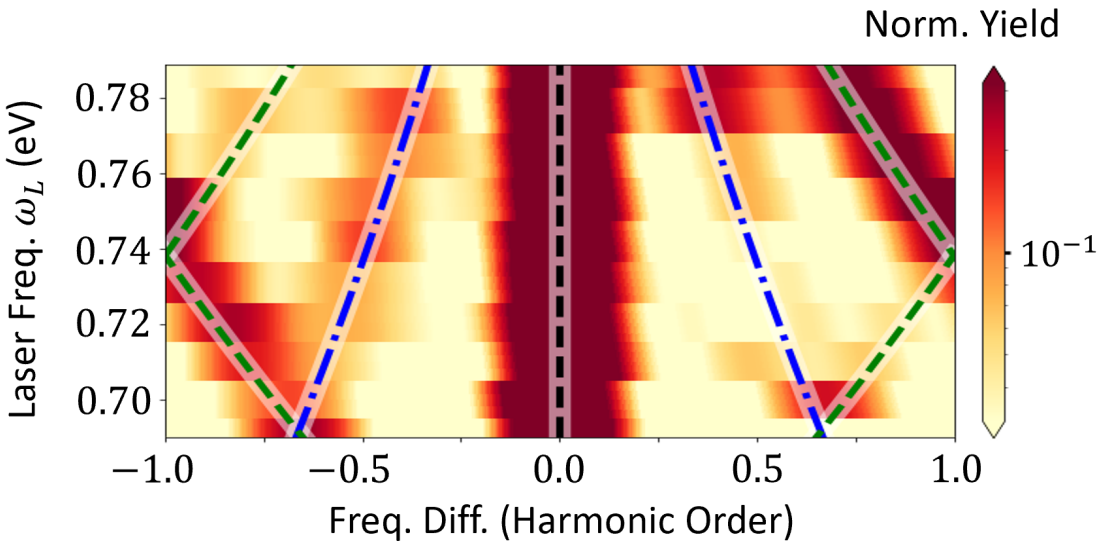

Figure 4.4: Stacked HHG spectra as a function of laser frequency, for laser wavelengths between 1575 nm and 1800 nm. The trendlines correspond to the sum and difference frequencies $\Delta\omega_1$ and $\Delta\omega_2$ of Eq. (4.5), as fitted in Fig 4.5(b).

It is worth noting that there is nothing special about the sidebands appearing on the high-energy side of the harmonic peaks, and that there are other driving laser wavelengths for which the low-energy sidebands dominate. This fluctuation in the relative strength between the harmonics and the sidebands is due to the finite sampling of the beat between incommensurate frequencies.

The fact that *two* sidebands are present in Fig. 4.3 above (and below, though they are less intense) each harmonic peak is significant, however: it means that the harmonics are modulated not just at ω_{CM}, but also at $2\omega_{\mathrm{CM}}$. This modulation is consistent with the particle-like CM shown in Fig. 4.1(c), in which the time-dependent hole density evolves at both the fundamental CM frequency and its second harmonic. The presence of both sets of sidebands thus means that the HHSS probe is sensitive to the full dynamical evolution of the CM.

One could determine the CM frequency ω_{CM} from the single stacked spectrum

shown in Fig. 4.3(b); however, I now show that the accuracy of the extraction of ω_{CM} increases if one scans the driving laser frequency. This is illustrated in Figure 4.4, which shows clear patterns in the evolution of the sidebands' locations relative to the central odd harmonic. The four trend lines correspond to the sum and difference frequencies $\Delta\omega_1$ and $\Delta\omega_2$ of Eq. 4.5, highlighted by the blue and green lines, respectively. The green dashed lines have a discontinuity near $\omega_L = 0.74\,\mathrm{eV}$ ($\lambda_L = 1675\,\mathrm{nm}$), when SB_2 reaches the edge of the stacking box and reemerges on the other side of it. This means that sidebands from different harmonics interfere with each other at the edges of the stacked spectra and then cross. Similarly, for laser frequencies near $\omega_L = 0.70\,\mathrm{eV}$ (1775 nm), SB_1 and SB_2 cross paths and interfere with each other.

4.4. Extraction of CM Frequency

To extract ω_{CM} from the laser-wavelength scan, I systematically record the frequency difference between each sideband peak and its nearest odd harmonic across the plateau and sort these peaks into two groups associated with SB_1 and SB_2. To do so, for each laser wavelength I record the energies of all of the peaks in the harmonic plateau and then distinguish between odd harmonics (at odd multiples of the MIR frequency) and sidebands (every other peak). In Figure 4.5(a), I plot the frequency difference between each of the thus-detected sideband peaks and their nearest odd harmonics for driving wavelengths between 1575 and 1800 nm. Here, all of the sideband peaks clearly fall into two groups, which I will associate with SB_1 and SB_2. For each wavelength, I automate the sorting of the sideband peaks between SB_1 and SB_2 using a 1D k-means clustering algorithm [228] with $k = 2$ since there are two sets of sidebands. Essentially, this algorithm

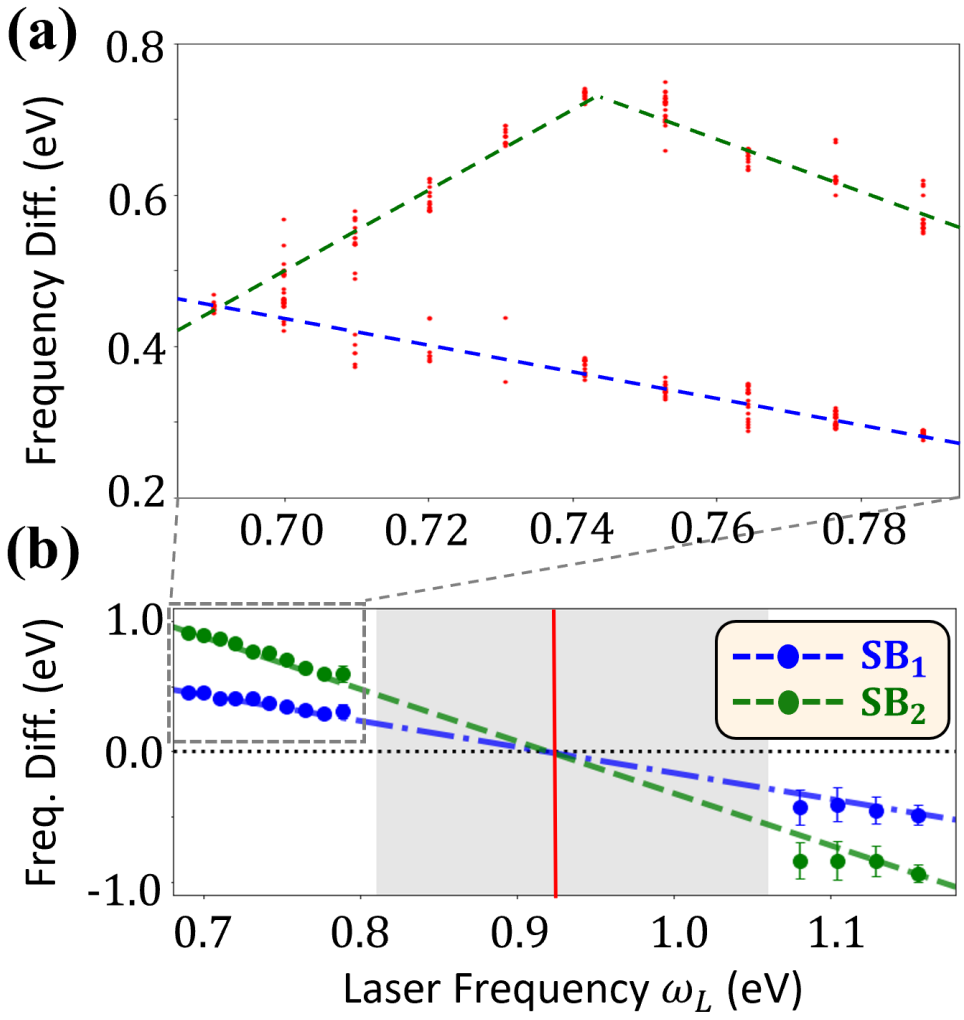

Figure 4.5: (a) Individual harmonic and sideband peaks analysis. Markers show the frequency difference between all the sideband peaks and their nearest odd harmonic throughout the HHG plateau for driving laser wavelengths between 1575 and 1800 nm. The two dashed curves mark the linear regression of the clusters of points associated with SB_1 and SB_2 (see text). (b) Sideband analysis to extract the CM frequency. The markers show the average energy separation of SB_1 and SB_2 from their odd harmonics with the error bars marking the standard deviation – note that most error bars are contained within their respective markers. The vertical red line marks $\omega_{CM}/2$, where SB_1, SB_2, and the odd harmonics are all predicted to overlap.

calculates the average difference frequency, and then sorts the peaks by whether they fall above or below this average. Compared to the stacked spectrum, the analysis of the individual sideband peaks across the entire harmonic plateau provides not only $\Delta\omega_1$ and $\Delta\omega_2$ (which are indeed consistent with the stacked-spectrum results), but also a measure of the corresponding uncertainties.

In Figure 4.5(b), I plot the mean values and standard deviations of the sideband energy differences $\Delta\omega_1$ and $\Delta\omega_2$ as a function of the laser frequency ω_L. For clarity, I have unfolded SB_2 below $\omega_L = 0.74\,\mathrm{eV}$ to avoid the discontinuity seen in (a). Note that this unfolding does not require prior knowledge of the CM frequency, only that of the driving laser. I have also chosen to plot the frequency differences with positive (negative) values for laser wavelengths where $2\omega_L < \omega_{\mathrm{CM}}$ ($2\omega_L > \omega_{\mathrm{CM}}$). Again, this does not require prior knowledge of the CM frequency since it can be inferred from the sign of the slopes in the stacked spectrum. The shaded gap in the middle marks the laser frequencies where the sideband peaks become indistinguishable from the odd harmonics in the HHG spectrum. To recover the CM frequency, I then fit the sideband energies against the prediction of Eq. 4.5. For both datasets, the fits are excellent. Each set of sidebands provides an independent measurement of $\omega_{\mathrm{CM}}/2$ with

$$\begin{aligned} \mathrm{SB}_1 &: \ \omega_{\mathrm{CM}} = 1.841 \pm 0.004 \text{ eV}, \\ \mathrm{SB}_2 &: \ \omega_{\mathrm{CM}} = 1.849 \pm 0.002 \text{ eV}. \end{aligned} \tag{4.6}$$

The extracted frequencies in Eq. 4.6 are both in good agreement with each other and also consistent with the value of $1.83 \pm 0.05\,\mathrm{eV}$ which I obtain directly from the CM dynamics in Fig. 4.1. I note that the inclusion of laser wavelengths above *and* below the CM frequency greatly improves the precision of the measurement of the CM frequency ω_{CM}.

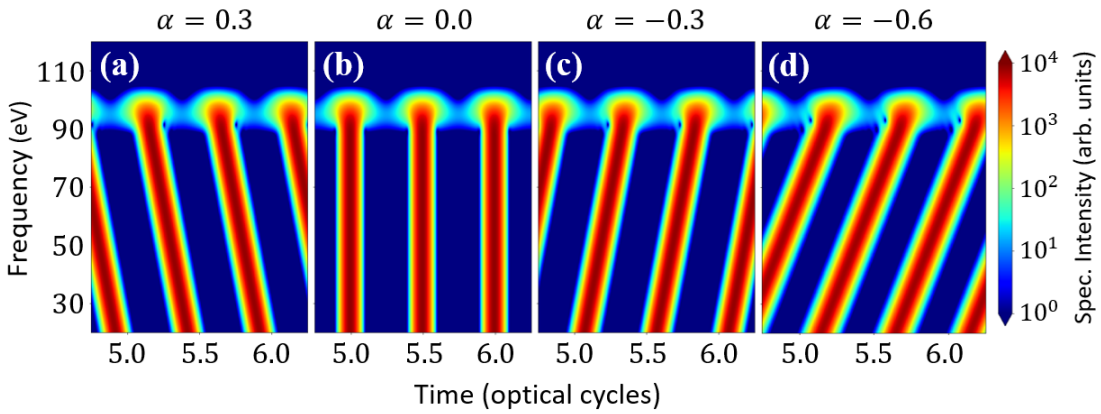

Figure 4.6: Gabor transforms corresponding to four different values of α, defined in Eq. 4.8. Changing α modifies the attochirp of the harmonic response.

4.5. Simplified Model of CM+HHSS

The idealized harmonic response from a gas-phase target irradiated by a one-color laser field with a frequency ω_L, a cutoff frequency ω_c defined by Eq. 1.2, and an envelope $F(t)$ is given by

$$d(t) = F(t) \cdot \sum_{n=1,3,5...}^{\infty} A_n \sin\left(n\omega_L t + \phi_n\right) \tag{4.7}$$

where the amplitude and phase of the n^{th} harmonic are defined by

$$A_n = \begin{cases} 1\ , & n\omega_L \leq \omega_c \\ e^{-(n\omega_L - \omega_c)}\ , & \text{otherwise} \end{cases} ; \qquad \phi_n = \frac{\alpha\omega_L}{U_p} n^2 - 2\pi n\Delta \tag{4.8}$$

where Δ is the delay between the start of the driving laser field and the initiation of the CM, U_p is the ponderomotive energy defined by Eq. 1.2, and α is a parameter which describes the attochirp. I have chosen a value $\alpha = -0.3$ for my model calculations – see Figure 4.6), since the slope of the features in Fig. 4.6(c) match the slope of the semiclassical short trajectory curves shown in *i.e.* Fig. 2.4.

Now I wish to include in this model a periodic modulation, as if by the particle-like CM dynamics shown in Fig. 4.1. Thus, I modify the previously-obtained dipole signal $d(t)$

via

$$\tilde{d}(t) = d(t) \cdot \left[1 + e^{-t/\tau} \sum_m B_m \sin\left(m\omega_{\mathrm{CM}} t + \phi_m\right)\right] \tag{4.9}$$

where τ is a decoherence time for the CM dynamics, and the parameters $\{m, B_m, \phi_m\}$ describe the individual Fourier components of the field-free CM dynamics. For instance, for the particle-like CM in BrC_4H shown in Fig. 4.1(d), there are two main Fourier components: one at $\omega = 1 \cdot \omega_{\mathrm{CM}}$, and a second at $2 \cdot \omega_{\mathrm{CM}}$ that is roughly four times less intense as the first, and with an extra $\pi/4$ phase shift. Note that between Eq. 4.7 and 4.9, there are many "free" parameters in this analytical model which pertain to either the description of the laser or the CM. However, most of these parameters are determined by the laser and molecular parameters chosen for the full TDDFT simulations. Additionally, the CM-induced modulation of the harmonic response is quite robust in both the model and the full TDDFT calculations.

In Figure 4.7, I perform the same analysis as Fig. 4.4, instead using these model CM+HHSS spectra. The blue and green trendlines are taken from the full TDDFT results, using Eq. 4.5 and the measurements of the CM frequency in Eq. 4.6 for SB_1 and SB_2). The resulting wavelength-dependent stacked spectrum looks very similar to Fig. 4.4. Here, I use the same time discretization in the model calculations as the full TDDFT simulations, so that the width of the harmonic and sideband peaks are the same as in Fig. 4.4. The ratio of amplitudes between SB_1 and SB_2 has been set at 4:1 for all laser wavelengths explicitly in the model calculations, while there is no such determination in the full TDDFT simulations.

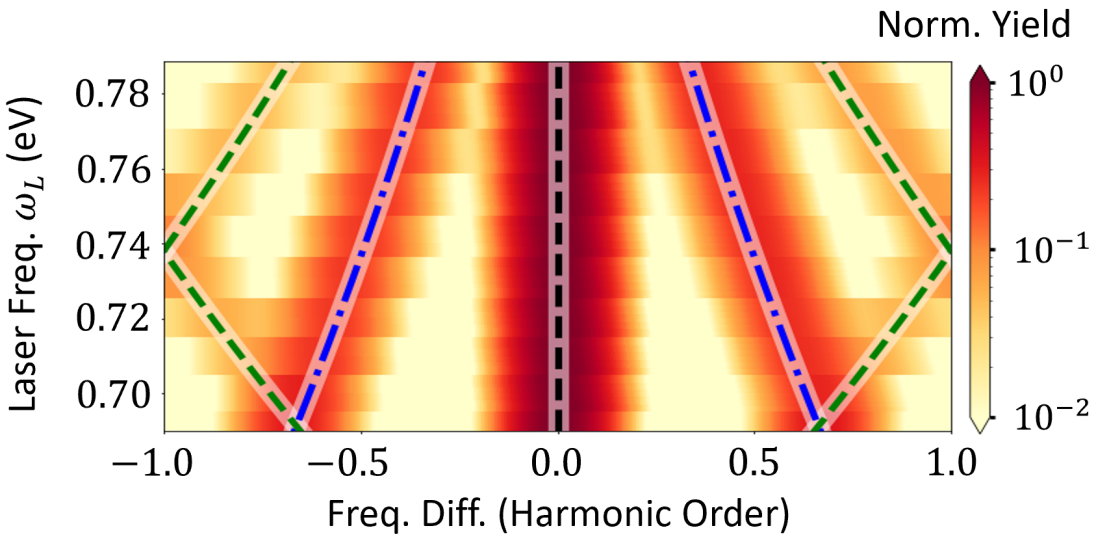

Figure 4.7: Stacked HHG spectra as a function of laser frequency taken from model calculations, for laser wavelengths between 1575 nm and 1800 nm. The trendlines are taken from full TDDFT calculations (same as Fig. 4.4).

4.6. Experimental Viability

Until now, I have assumed the idealized condition of a single, perfectly oriented, BrC_4H molecule undergoing particle-like CM. However, I have verified the viability of HHSS for more realistic experimental considerations. I start by investigating the effect of a distribution of molecular alignments. I use a Gaussian distribution of angles around perpendicular alignment and coherently average the corresponding CM+HHG dipole signals, for $\lambda = 1575\,\text{nm}$. In Fig. 4.8, I plot the evolution of the stacked spectrum (see Section 4.3) when increasing the width of the alignment distribution from perfect orientation ($\theta \equiv 0°$). Strikingly, up to 40° FWHM, I clearly see SB_1 and SB_2 sideband peaks, and I find that their positions can be located with error bars comparable to those in Fig. 4.5(b). The relatively lower strength of the sidebands when including the distribution of alignment angles is caused by the the component of the MIR field that is parallel to the molecular axis which disturbs the field-free CM dynamics. This generally leads to sidebands at slightly

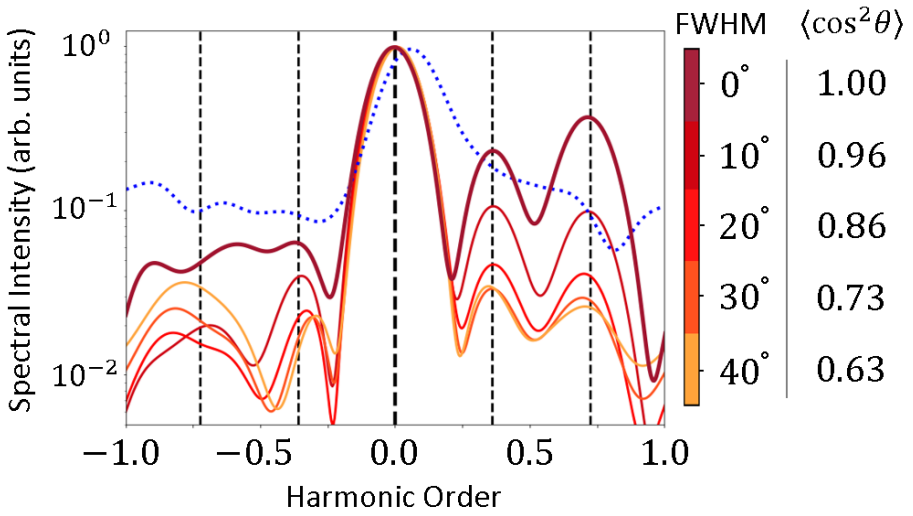

Figure 4.8: Effect of having a distribution of molecular-alignment angles around perpendicular alignment. The solid curves compare the stacked spectrum of Fig. 4.3 when including various Gaussian angular distributions – see colorbar. For comparison, the blue dotted curve shows the unaligned stacked spectrum. Vertical black lines mark the locations of the odd harmonic and sidebands.

different frequencies for different alignment angles. For the completely unaligned sample (blue dotted curve in Fig. 4.8), the sidebands average out altogether. I note that the CM induces different modulation amplitudes in the sub-cycle dipole signals of molecules with the same alignment but opposite orientations, except when the molecule is exactly perpendicular to the laser polarization. To generate Fig. 4.8, I therefore sample molecular-orientation angles covering a full 180° instead of the 90° range that would otherwise be sufficient for a linear molecule in a symmetric multi-cycle MIR field.

Next, I have found that the sideband signals are robust with respect to having only a fraction of the molecules in the HHG target gas undergoing CM. I consider a weighted average of the dipole signals from the target with and without CM – thin red and solid blue curves in Fig. 4.2, respectively. I find that the intensity of the sidebands scales quadratically with the fraction of molecules with CM, as expected for a coherent process.

I also expect the sidebands to phase match to the same extent as the constituent harmonics in that pulse train, since they originate from the time-domain amplitude modulation of the individual bursts in the harmonic pulse train.

Finally, I have tested the influence of a finite CM lifetime, *e.g.*, due to the onset of nuclear dynamics. When adding a phenomenological exponential decay to the CM-modulated dipole component, I still observe well-defined sidebands with a lifetime as short as 10 fs. Although the formal inclusion of nuclear motion is beyond the scope of this report, my preliminary calculations including (classical) nuclear dynamics described at the Ehrenfest level indicate that the linear, triple-bonded BrC_4H molecule is quite rigid, such that the localized hole motion is stable over multiple CM cycles.

Chapter 5. Frequency-Matched Strobo-Spectroscopy

In this chapter, I present frequency-matched high-harmonic strobo-spectroscopy of charge migration (CM+FMSS), which takes advantage of the intrinsic time resolution of the HHG process (the attochirp) in order to track the time-dependent location of the electron hole by scanning the delay between the initiation of the CM and a frequency-matched few-cycle laser pulse. More specifically, I find that there is a harmonic-frequency- and delay-dependent modulation in the yield that results from a site-specific feature of the harmonic spectrum – in this case, a decrease in the total yield when the hole is on the halogen atom. Finally, I also begin a preliminary investigation into the effect of a many-cycle laser pulse on the CM dynamics.

In Sec. 5.1, I introduce the concept of CM+FMSS, an independent pump-probe scheme which I use to track particle-like CM dynamics. The simulation details are discussed in Sec. 5.2. In Sec. 5.3, I present delay-dependent HHG spectra of bromobutadiyne (BrC_4H) undergoing CM dynamics, and I extract the time-dependent location of the electron hole along the molecular backbone in Sec. 5.4. I investigate whether the modulation of the harmonic signal via the CM dynamics occurs in the ionization step or the recombination step of the HHG process in Sec. 5.5, and I check the robustness of my results with respect to more realistic experimental conditions in Sec. 5.6. Finally, in Sec. 5.7, I detail my preliminary findings of a delay-dependent drift in the CM dynamics when irradiated by a many-cycle laser pulse.

5.1. Introduction

In Chapter 4, I presented high-harmonic sideband spectroscopy of charge migration (CM+HHSS), in which the CM dynamics causes a coherent time-dependent beat in the harmonic signal, resulting in sidebands in the corresponding CM-modulated HHG spectrum. By varying the wavelength of the HHG-driving laser field, I was able to accurately determine the CM frequency ω_{CM}. Knowing this frequency, the inherent sub-femtosecond temporal resolution of the HHG process (via the attochirp [98, 158, 229, 230] of the harmonic radiation), allows me to go further with this line of investigation. Instead of varying the laser wavelength, I vary the sub-cycle delay between the initiation of the CM dynamics and a frequency-matched few-cycle laser pulse; by doing so, I gain access to some phase information: put simply, where the hole is at what time.

In this chapter, I present frequency-matched high-harmonic strobo-spectroscopy of charge migration (CM+FMSS), simulated with time-dependent density-functional theory (TDDFT) [105, 109]. Here, I am studying the same CM mode in bromobutadiyne (BrC_4H) as was described in Sec. 4.2. After the initiation of the CM dynamics, CM+FMSS uses a delay-dependent, few-cycle HHG-driving laser pulse as an independent probe step to precisely determine the time-dependent location of the electron hole, by tracking the amount of electron density on the bromine atom. I match the frequency ω_L of the laser to ω_{CM} such that the position of the electron hole is the same in each half-cycle of the laser field for any given delay. The driving laser field is polarized perpendicular to the CM motion, so that it does not drive the electron density.

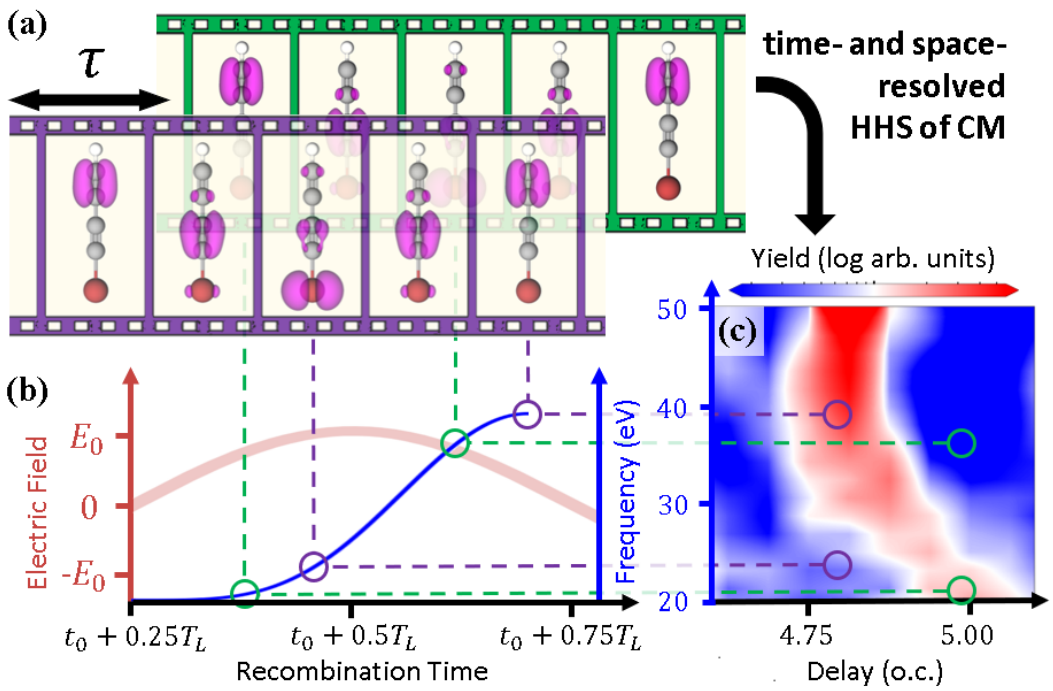

Figure 5.1: Schematic of the CM+FMSS analysis: (a) snapshots of the time-dependent CM dynamics following the creation of a localized hole on the bromine atom for two different time delays (purple and green frames). (b) This dynamics is probed by a delayed, frequency-matched HHG-driving laser field (red curve). The semiclassical return energy of the rescattered electron wave packet is plotted as a function of the recombination time (blue curve). (c) The resulting orbital-resolved, normalized CM+FMSS spectrum (see text) over half an optical cycle for delays near 4.50 optical cycles (approximately 18 fs after the initiation of the CM). There is a clear variation in the delay-dependent harmonic spectrum due to the CM dynamics.

CM+FMSS is a pump-probe scheme: the "pump step" occurs at $t = 0$ when the CM dynamics is initiated via constrained DFT, and a HHG-driving laser field probes the CM dynamics at some later time. Importantly, in CM+FMSS the pump and probe steps are completely independent of one another, in contrast to other studies using HHG to probe CM dynamics [34, 67, 231]. In Figure 5.1, I show a schematic which describes the FMSS concept: panel (a) depicts the time-dependent CM dynamics at two different time delays after initiation (purple and green frames, respectively). This dynamics is probed after some time τ by a HHG-driving laser field, shown in panel (b), with $\omega_L = \omega_{\mathrm{CM}}/2$. Also

in panel (b) I show the semiclassical [72–74, 93] time-dependent return energies during one-half cycle of the HHG-driving laser field, which maps to the sub-cycle time-dependent emission frequencies in the harmonic spectrum [99, 158, 232] – see again Fig. 1.5. For different delays, a given harmonic energy is emitted at a different time during the CM period, and this strongly affects the resulting HHG yield as shown in panel (c). For example, at a delay of 4.55 o.c., the low-order (high-order) harmonics are emitted when the hole is located on the bromine atom (terminal C $\equiv$ C bond), which gives rise to low (high) HHG yield – see the purple dashed lines in Fig. 5.1. A central finding of this work is that the delay-dependent harmonic yield tracks the time-dependent electron density on the bromine atom, from which I determine the phase of the CM motion.

5.2. Simulation Details

In my CM+FMSS simulations, I start by creating a one-electron valence hole localized on the halogen end of a bromobutadiyne (BrC_4H) molecule using constrained density functional theory, as described in Sec. 4.2. I then induce HHG in the BrC_4H cation undergoing CM, using a laser pulse with a polarization direction perpendicular to the molecular backbone so that the electron density is not driven along the molecular backbone. Unlike my sideband spectroscopy analysis from Chapter 4, I use a fixed laser frequency $\omega_L = \omega_{\mathrm{CM}}/2$ (corresponding to a laser wavelength $\lambda_L = 1344$ nm). The frequency-matching condition is chosen such that the electron hole is at the same position along the molecular backbone at every half-cycle of the laser field. By using different sub-cycle delays between the initiation of the CM and the laser field, I therefore sample different positions of the electron hole along the molecular backbone. For my TDDFT simulations,

I use $\sin^2$ laser pulses centered around a delay τ relative to the initiation of the CM, and that last for 5 o.c. in total ($\approx$ 1.5 o.c. FWHM). I then scan the sub-cycle-resolved delay over two full laser cycles, advancing the delay τ in increments of 1/16 optical cycles. In all simulations I use a peak intensity of 45 TW/cm^2, leading to a cutoff energy of around 40 eV.

Again, I use grid-based TDDFT with a local-density-approximation exchange-correlation functional [123–125] and average-density self-interaction correction [126–128] within the Octopus software package [119, 120, 129, 130] to describe both the CM and HHG processes. I use a simulation box with dimensions of 90 $\times$ 40 $\times$ 90 a.u. (with the shorter box length transverse to both the laser field and molecular axes), and a complex absorbing potential that extends 15 a.u. from each edge of the box. I choose the box dimensions such that I select the short-trajectory contribution to the HHG spectrum that is usually observed in HHG measurements [110], by absorbing the long-trajectory contribution. I use a grid spacing of 0.3 a.u. in all directions.

The harmonic spectrum is calculated using a $\sin^2$ window function that has the same width as the laser pulse (5 o.c. in total) – see again Sec. 2.3. I focus on the dipole signal parallel to the driving laser field (in the x-direction). I have checked that the results shown below are nearly identical when including the dipole signal in the directions perpendicular to the laser field. The oscillating charge density along the molecular axis induces a significant dipole contribution along the axis of the molecular backbone, as was also observed in Kuleff *et al* [233]. However, above 20 eV, the total emission spectrum is dominated by the driven (harmonic) response, with the CM-only emission rapidly decreasing with respect to the emission frequency – see Figure 5.2.

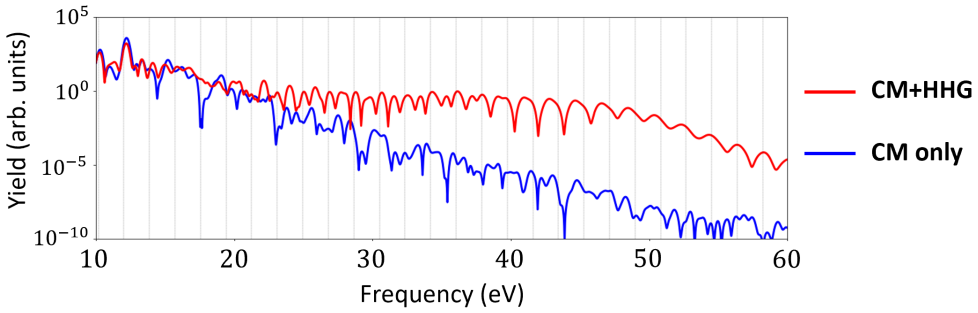

Figure 5.2: Total spectral intensities for a bromobutadiyne molecule undergoing CM, with (red curve) and without (blue curve) the harmonic-generation field applied in the perpendicular direction.

As a first approximation, I calculate the delay-dependent CM+FMSS spectra from the CM-orbital-resolved dipole moment, since the CM orbital dynamics provides the clearest picture of the CM motion – see again Fig. 4.1(b,c). However, the CM-orbital-resolved spectrum cannot be observed experimentally. Consider the electronic structure of BrC_4H: in addition to six lower-lying σ-type orbitals that do not contribute to the CM or the HHG, there are six π-type orbitals that span the entire length of the molecular backbone. Three of these π orbitals lie in the xz-plane (where the molecular backbone is along the z-axis, and the laser polarization direction is along the x-axis), while the other three lie in the yz-plane. By pulling one of the two electrons from one of the π orbitals in the xz-plane (the CM orbital), I induce particle-like CM in BrC_4H; however, there are an additional 4 electrons in the π_x system that strongly contribute to both the valence electron dynamics and the HHG process. As an illustration, Figure 5.3 shows the orbital-resolved CM+FMSS spectra for different groups of orbitals. The π_x-orbitals-resolved CM+FMSS spectrum is indeed consistent with the total dipole signal, while the contributions from the π_y and σ orbitals are several orders of magnitude lower, as expected.

Lastly, in order to more clearly investigate the CM-induced delay-dependent mod-

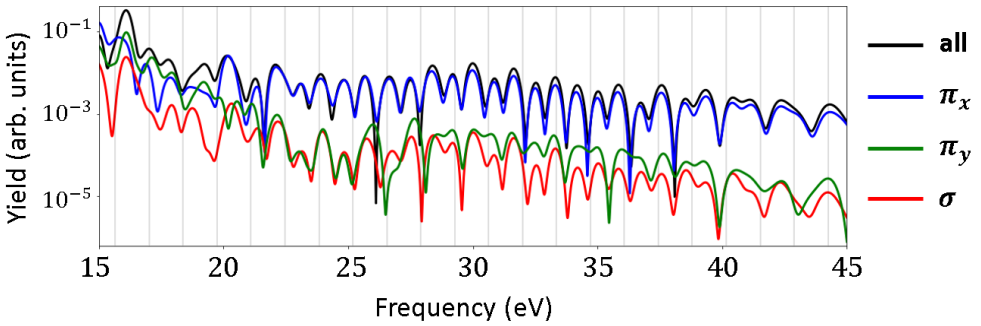

Figure 5.3: CM+FMSS spectra (a) from the total dipole signal (black), and (b) from the π_x-orbitals-resolved (blue), (c) π_y-orbitals-resolved (green), and (d) σ-orbitals-resolved dipole moments, for a delay $\tau = 4$ optical cycles.

ulation of the harmonic signal, I first smooth the spectrum using a $6\omega_L$-wide moving average to remove the individual harmonic peaks. Then, I normalize the delay-dependent CM+FMSS spectrum by the delay-averaged harmonic signal, as I did in Ch. 3; this final step removes the general shape (perturbative region, plateau, and cutoff region) of the harmonic spectrum and focuses purely on the delay dependence.

5.3. Delay-Dependent CM+HHG Spectra

In Figure 5.4(a), I show an expanded version of the normalized CM+FMSS spectrum calculated from the CM-orbital-resolved dipole moment shown previously in Fig. 5.1(c), around 4 optical cycles (approximately 18 fs) after the initiation of the CM. Clearly, there is a pronounced half-laser-cycle-periodic, delay- and harmonic-frequency-dependent variation in the harmonic signal which is not present in the neutral molecule. This variation is such that the yield is roughly five times more intense when the hole is *not* on the bromine atom. Below the cutoff energy $E_c = 40$ eV, this spectral maximum trends towards earlier delays as the harmonic frequency increases. As I discuss below, the slope of this tilt matches the negative of the attochirp of the harmonic radiation.

In addition, I plot the delay-dependent harmonic spectrum calculated from the

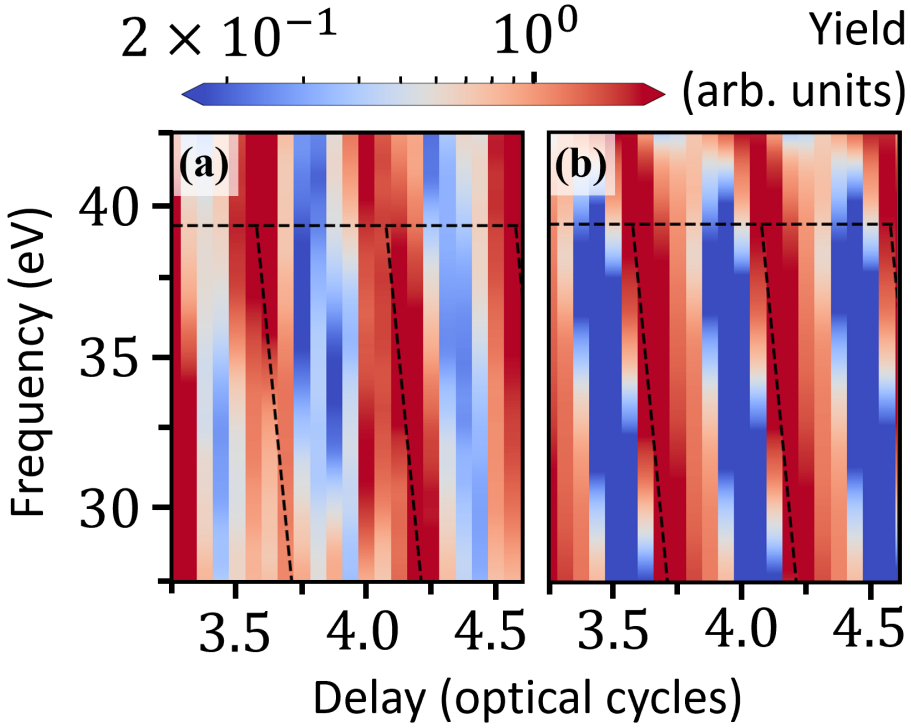

Figure 5.4: (a) Normalized, CM-orbital-resolved FMSS spectrum for $\lambda_L = 1344$ nm ($\omega_L = \omega_{\mathrm{CM}}/2$), $I_\circ = 45$ TW/cm^2. (b) Delay-dependent harmonic spectrum taken from model calculations (see text). Black dashed lines are taken from ridge detection of the peaks in panel (b).

delay-dependent model dipole signal of Sec. 4.5 in Figure 5.4(b). Like in panel (a), we see a half-cycle-periodic modulation tilting to the left as the harmonic frequency increases. The modulations seen in both panels are consistent with one another, as evidenced by the black dashed lines in both plots, taken from a ridge detection of the peaks in the model spectrum in (b). Removing the attochirp from the model calculations of Sec. 4.5 (first term in the phase of Eq. 4.8) eliminates the slope of the variation shown in Fig. 5.4(b). The delay dependence of the variation in the harmonic signal in Fig. 5.4(a) is therefore sensitive to the attochirp of the harmonic radiation, as illustrated in the schematic of Fig. 5.1. The recombining electron wave packet images different molecular landscapes depending on when it rescatters [98, 99, 158, 229, 230, 232], leading to a variation in

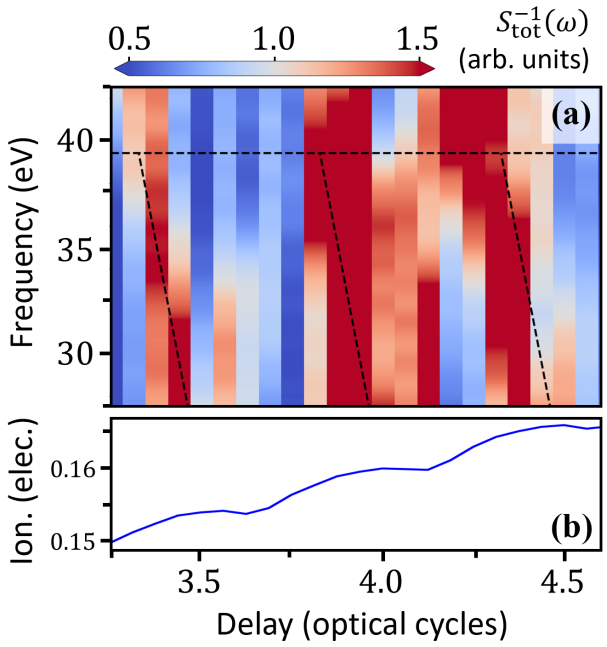

Figure 5.5: (a) Normalized CM+FMSS spectrum, again for $\lambda_L = 1344$ nm and $I_\circ = 45$ TW/cm^2, calculated from the dipole signal from the three π_x orbitals. Black dashed lines again taken from model calculations. (b) Amount of ionized charge, three optical cycles after the center of the laser pulse, as a function of delay.

the HHG light emission. High-frequency light (near the cutoff energy) is emitted later, meaning that an earlier delay is required to image any given position of the hole along the molecular backbone.

Note that harmonic generation from any neutral molecules not undergoing CM would not have any delay dependence, and so would be canceled out by the normalization process. I also note that the time resolution built into FMSS via the attochirp means that there will be a delay and frequency dependence to the harmonic yield even if ω_{CM} does not match $\omega_L/2$ exactly, *i.e.*, as long as $1/|\omega_{CM} - \omega_L/2|$ is small compared to the time (delay) duration over which the CM is sampled. For an arbitrary driving laser frequency, I expect that there will still be a modulation of the resulting HHG signal, even if it is more complicated [234].

From the purple and green dashed lines in Fig. 5.1, we see that the HHG yield increases when the hole is located in the terminal bond (*i.e.* when the electron density is on the bromine atom), and vice versa. This conclusion suggests that the scattering cross-section of the bromine atom is larger than the rest of the carbon chain, meaning that an increase in the overall density on the bromine atom (when the hole is *not* on the halogen) results in a relative increase in the harmonic yield. This is a crucial result: because there is a spatially-resolvable feature in the harmonic spectrum – here, a decrease in the harmonic yield when the hole is located on the halogen atom – I am able to perform a time- and space-resolved measurement of the CM dynamics using FMSS.

Though I am simulating and measuring particle-like CM dynamics [35, 66, 69] here, I expect that FMSS can be used to characterize a variety of ultrafast electron dynamics. The only requirement is that the electron dynamics is periodic, and that there is one or more features of the harmonic yield that can be traced back to specific parts of the molecule. As an example, in the usual way that CM is described, as a back-and-forth motion between two sites (*e.g.* bromoacetylene), a measure of the amount of electron density on one of the sites fully describes the CM motion since any hole density not on the probed site must be on the other site.

As discussed in Sec. 5.2, the CM orbital used in Fig. 5.4 does not correspond to an experimental observable. Therefore, I look at the combined dipole signal from the three π_x orbitals in Figure 5.5(a). Thus far, we have been looking at the relative increase in the delay-dependent HHG yield that occurs when the hole is *not* on the bromine atom. This method works well for the CM-orbital-resolved FMSS spectrum of Fig. 5.4(a); switching to the π_x-orbitals-resolved FMSS spectrum, however, I instead look for an *absence*

of harmonic yield corresponding to the hole being on the bromine atom. This is because the hole spends only about 25% of its time on the halogen end, meaning that the dip in harmonic signal is sharper and therefore easier to detect when inverting the spectrum. Thus, in Fig. 5.5(a), I plot the inverse of the π_x-orbitals-resolved harmonic yield, $1/S_\pi(\omega)$. Again, we see a delay- and harmonic-frequency-dependent variation in the (inverse) harmonic yield due to the CM dynamics. The black dashed lines, again taken from my model calculations in Fig. 5.4(b), have been shifted by $0.25\omega_L$ since I am looking for an absence, rather than the presence, of harmonic signal.

5.4. Tracking the Electron Hole

I have shown that the HHG yield tracks the hole density on the bromine atom. To further illustrate this, I algebraically remove the effect of the attochirp in the CM+FMSS spectra of Figs. 5.4(a) and 5.5(a) in order to obtain an absolute-time-dependent measure of how much hole density is on the bromine end of the molecule. This analysis is performed in Figure 5.6. From the semiclassical model of HHG [72–74, 93], I know exactly when each harmonic is emitted as a function of absolute time (for every delay τ). From my TDDFT simulations, I also know the exact location of the electron hole as a function of absolute time. Thus, I can unambiguously map the variation in the harmonic signal to the amount of electron density on the halogen atom. The blue curve depicts the amount of hole density centered around the bromine atom, taken from the field-free CM dynamics depicted in Fig. 4.1(b). I compare this hole density to the recombination-time-dependent harmonic yield, integrated over harmonic frequencies above 20 eV, for the CM-orbital-resolved data in Fig. 5.4(a) (solid red curve) and the π_x-orbitals-resolved data in

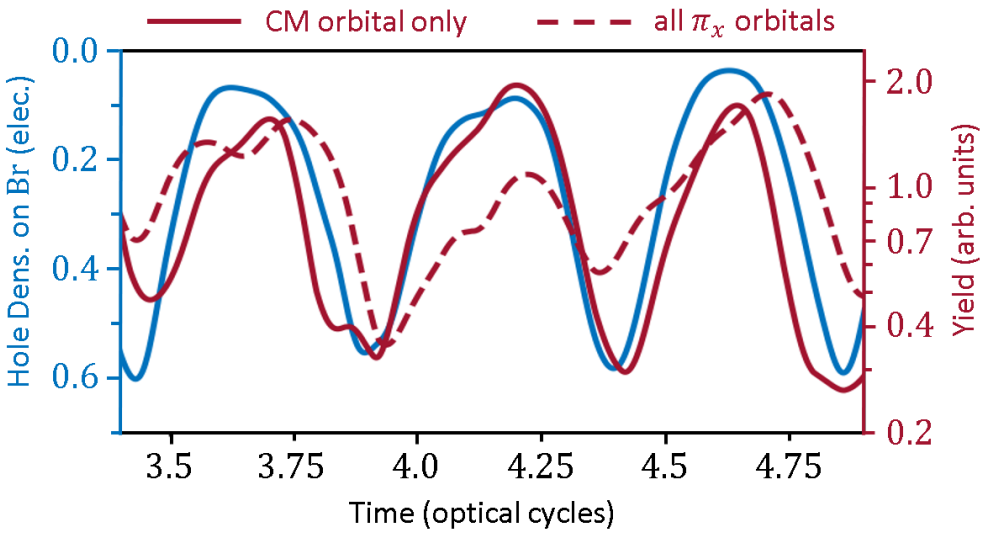

Figure 5.6: Comparison between time-dependent, field-free hole density on the bromine atom (blue) and recombination-time-dependent HHG yield, with the attochirp removed and integrated over harmonic frequencies above 20 eV (red). The solid red line is taken from the CM-orbital-resolved spectra in Fig. 5.4(a), and the dashed line corresponds to the π_x-orbitals-resolved data in Fig. 5.5(a).

Fig. 5.5(a) (dashed red curve). In Fig. 5.6, a value near the top of the figure means the hole density is *not* localized on the bromine atom (is localized on the terminal bond), and therefore results in a larger HHG yield. Despite the vastly different methods used to obtain the red and blue curves in Fig. 5.6, they match each other very well. Note that the higher-frequency oscillations in the red curves (particularly, the dashed red curve) can be explained by the additional atomic-center-localized oscillations in the hole density seen in Fig. 4.1(c).

5.5. Ionization versus Rescattering

I now ask the question of whether the CM-induced modulation of the harmonic yield is due to the ionization step or the rescattering step. To do so, I return to Figure 5.5(b): here, I plot the amount of charge ionized from the simulation box, one-half laser cycle after the end of the laser pulse, as a function of the delay τ. There is a small

amount of leakage – ionized charge leaving the simulation box even in the absence of the laser field, approximately 2% of an electron per laser cycle – as evidenced by the overall slope in Fig. 5.5(b), which can be attributed to the absorbing boundaries in the direction perpendicular to both the CM and the laser. I have checked that the leakage disappears for a larger box size in the $\hat{y}$ direction, and that the leakage does not effect the results shown here. On top of this overall linear slope, we see a clear half-laser-cycle-periodic modulation in the ionization signal due to the CM dynamics. Different relative phases between the CM and the peaks of the laser field cause different amounts of charge to be ionized as a function of the delay τ. However, after correcting for the leakage, the amplitude of the oscillation in the ionization signal is quite small (roughly 1%) compared to the variation in the harmonic signal, for which the yield is roughly three times larger when the hole density is not localized on the bromine atom (as opposed to five times larger, for the CM-orbital-resolved case). Thus, I conclude that the modulation of the HHG signal from the CM dynamics occurs mainly as a result of the recombination step, not the ionization step.

5.6. Experimental Viability

It is interesting to consider how the CM+FMSS envisioned in this paper would fare when considering more realistic experimental conditions; in particular, the two approximations I am making concerning (1) the (perfect) perpendicular alignment of the molecule relative to the laser polarization, and (2) the absence of nuclear motion. For (1), I expect the biggest issue to be that a laser field component that is parallel to the molecular backbone will drive CM that is not necessarily in phase with the field-free CM, and which will

therefore likely give rise to a different delay dependence. For bromobutadiyne interacting with the few-cycle laser pulse I have used here, I find that the harmonic response to a parallel-polarized laser pulse does indeed exhibit a different delay dependence but that it is also substantially weaker than that of the perpendicular-polarized pulse and thus does not contribute much in the total delay dependence. For the longer driving pulses used in Chapter 4, I found that the sideband-based HHS proposed in that paper was valid for a full-width half-maximum angular distribution of 40°. Given the weaker response for the shorter pulse duration used here, I expect that FMSS will also tolerate at least 40° of angular distribution.

For (2) I can approximate the effects of including nuclear motion in several different ways. First, I have performed preliminary calculations of CM in bromobutadiyne when including Ehrenfest dynamics and find that the molecule is quite rigid when starting from the optimized ground-state geometry. A more thorough investigation into the nuclear degrees of freedom in bromobutadiyne can be found in Ref. [19]. However, I can also consider the timescale for the nuclear dynamics, as compared to the timescale of the few-cycle probe pulse that I use here. In particular, by incorporating decoherence into the model calculations described above, I find that FMSS remains applicable within the typical time scale for nuclear dynamics and decoherence. This robustness is demonstrated for a decoherence time of 10 fs in Figure 5.7.

Beyond the BrC_4H molecule used here, I note that similar particle-like CM modes have been predicted in other classes of molecules [35, 39]. Thus, given the generalizable nature of this approach, I expect that CM+FMSS analyses can be applied broadly to other classes of molecules, such as functionalized benzenes or even bio-molecules and be-

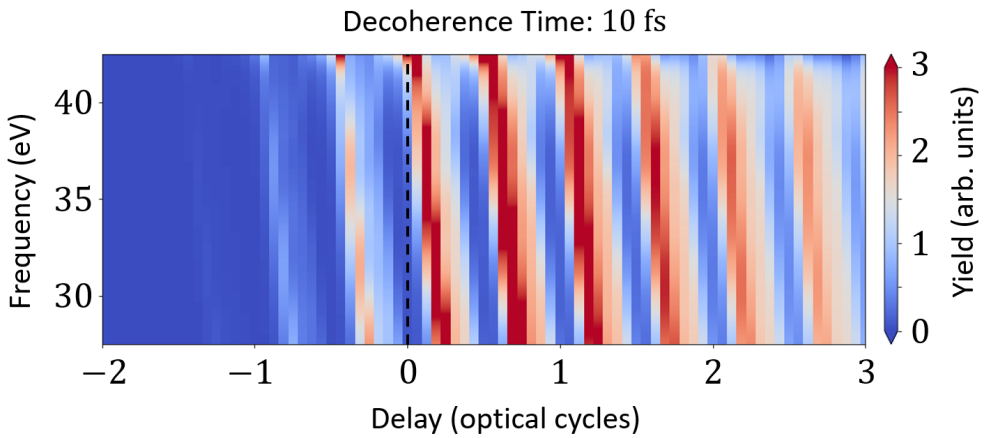

Figure 5.7: CM+FMSS analysis around $\tau = 0$, using the model calculations described by Sec. 4.5, with a 10 fs phenomenological decay on the CM dynamics.

yond. Given the intense, current interest in probing and understanding charge migration, with a range of experiments underway at large-scale X-ray facilities [223, 235], approaches based on HHS, such as FMSS, could be appealing due to the much wider availability of table-top based HHG sources.

5.7. Outlook: Charge Migration Drift

In this chapter and the previous one, I have investigated the effect of the CM dynamics on an applied laser field (in other words, performing spectroscopy). However, it would be naive to expect that the applied laser field has no effect on the CM dynamics, especially when using longer laser pulses, even despite the perpendicular configuration I use here. To that end, I apply a linearly-polarized MIR laser field which has a 2-cycle $\sin^2$ ramp-up, and then remains a continuous wave thereafter, to a BrC_4H molecule undergoing CM. I again look at the case where the polarization direction of the laser is perpendicular to the molecular backbone – see also Figure 4.1(a). I vary the wavelength λ_L, intensity $I_\circ$, and relative delay Δ between the initiation of the CM and the start of the laser field.

In Figure 5.8, I plot the amount of hole density located around the bromine

atom as a function of time for four different sub-cycle delays Δ. In the incommensurate-laser-frequency case in panel (a), for $\lambda_L = 1575\,\text{nm}$, the time-dependent CM dynamics do not change significantly as a function of delay, as I would expect since the laser is perpendicular to the CM motion. However, for the commensurate-laser-frequency case ($\lambda_L = 1344\,\text{nm}$) in panel (b), there are some delays for which the CM dynamics deviate (or "drift") from the field-free dynamics. As an analogy, consider a pendulum swinging at a frequency ω, with an applied periodic perturbation with the same frequency ω. Depending on the relative phase between the perturbation-free pendulum dynamics and the perturbation itself, the pendulum's dynamics will deviate from a simple harmonic oscillator as a function of time (eventually converging to a motion which is in phase with the perturbation). This drift does not occur in the incommensurate frequency case because the electron density is being nudged one way just as often as it is nudged in the opposite way.

I now investigate the dependence of the severity of the CM drift on the intensity of the applied laser field. Similar to Fig. 5.8, in Figure 5.9 I show the time-dependent hole density $\rho_H(z,t)$, this time along the entire molecular backbone, for several different sub-cycle delays Δ. The images are superimposed on top of one another; a clean periodic motion of the electron hole (near the left end of the figures) indicates that there is very little CM drift, while a blurring of the dynamics (near the right end of the figures) indicates strong CM drift. This is done for $\lambda_L = 1344\,\text{nm}$ and for two different laser intensities: (a) $I_\circ = 60\,\text{TW/cm}^2$ and (b) $I_\circ = 150\,\text{TW/cm}^2$. The vertical dashed red lines in each panel marks the time at which the delay-dependent CM dynamics starts to blur. Since the blurring starts approximately two optical cycles earlier in the lower-intensity case, I conclude

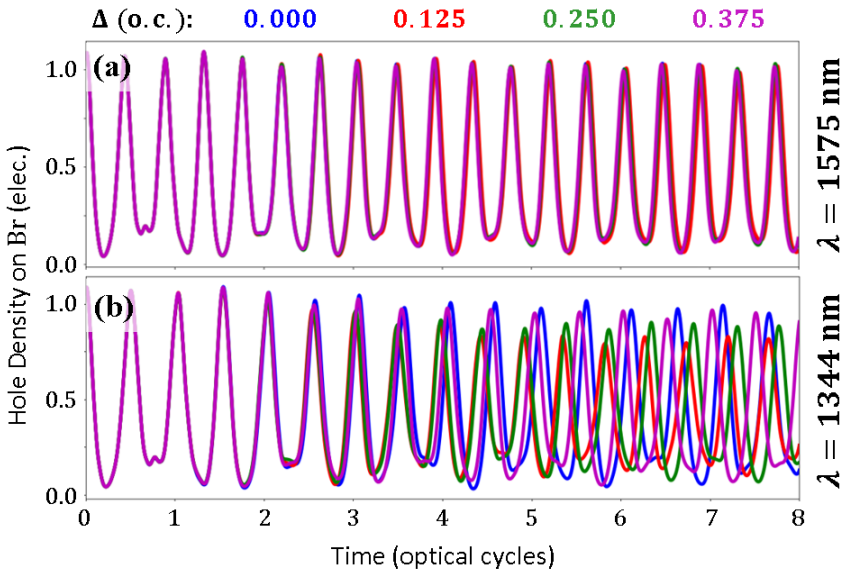

Figure 5.8: For laser wavelengths of (a) 1575 nm and (b) 1344 nm: the amount of hole density located on the bromine atom, as a function of time, for several different delays Δ between the initiation of the CM dynamics and the phase of the flat-top laser pulse.

that an increase in the laser intensity will cause the CM drift to progress faster.

Finally, I ask the question of whether there is a particular delay for which there is little to no CM drift. In Figure 5.10, I look at the time-dependent hole density around the bromine atom, at a delay $\Delta = 0.4375$ optical cycles. The applied laser has a wavelength $\lambda_L = 1344\,\text{nm}$, and I look at three different laser intensities: (black curve) 0 TW/cm^2 (field-free), (blue curve) 60 TW/cm^2, and (red curve) 150 TW/cm^2. At this particular delay, there does not appear to be much CM drift. Thinking about the semiclassical model of HHG presented in Sec. 1.3, I find that $\Delta = 0.4375\,\text{o.c.}$ is the delay at which each half-laser-cycle's ionization event coincides with when the hole is on the terminal bond (when there is an excess of electronic density on the bromine atom). Thus, going back to the resonantly-driven harmonic oscillator analogy, this delay is close to the steady-state solution. The pendulum is being nudged in phase with the original motion.

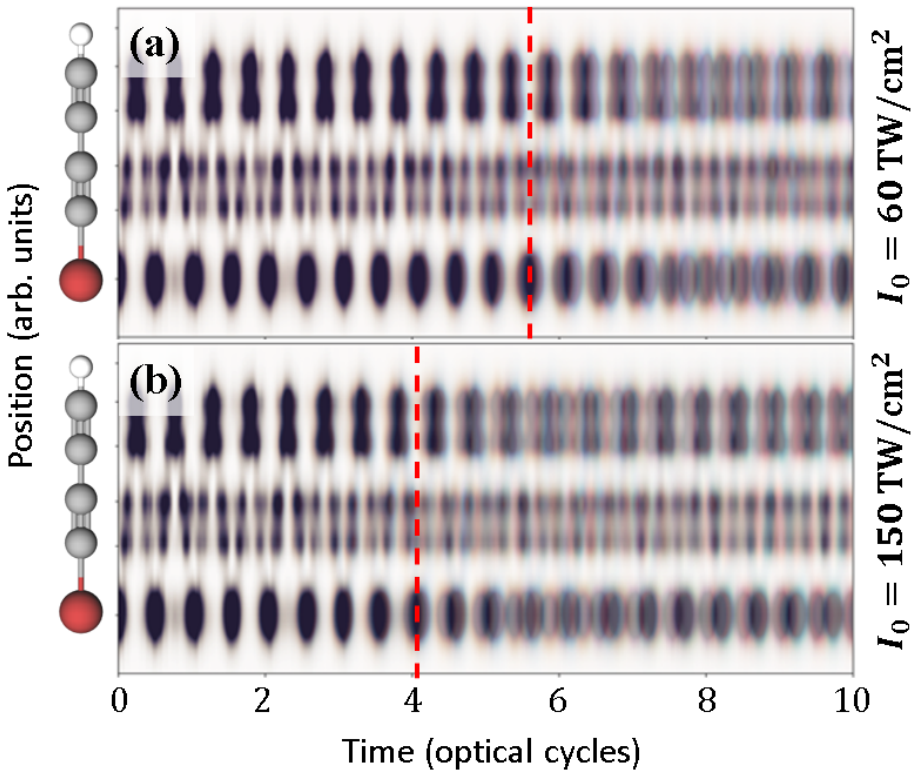

Figure 5.9: For a commensurate laser wavelength and laser intensities of (a) 60 TW/cm^2 and (b) 150 TW/cm^2: time-dependent hole densities, for four different sub-cycle delays, superimposed on top of each other. A blurring of the image indicates that the CM drift has dephased the delay-dependent dynamics.

I have avoided the effects of CM drift in the HHSS analysis of Chapter 4 by using an incommensurate laser frequency, and in the FMSS analysis of this chapter by using short (few-cycle) laser pulses. However, I do think that CM drift is an interesting phenomenon – in particular, in relation to the analogy with a driven simple harmonic oscillator – and I hope that it will be studied more closely in the future.

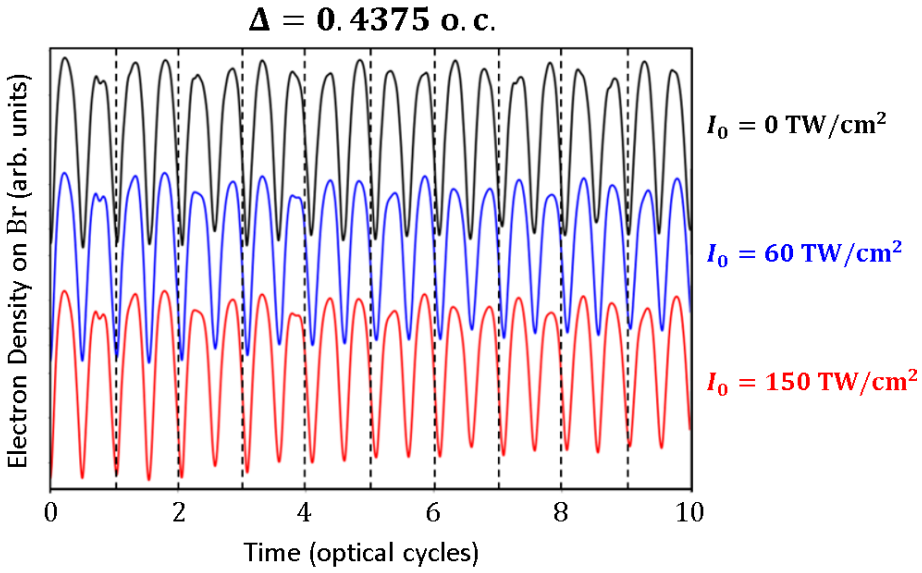

Figure 5.10: For a commensurate laser wavelength and three different laser intensities of (black curve) 0 TW/cm^2 (field-free), (blue curve) 60 TW/cm^2, and (red curve) 150 TW/cm^2, the amount of hole density located on the bromine atom, as a function of time, for a delay $\Delta = 0.4375$ optical cycles. (There is an offset between each of the curves.)

Chapter 6. Summary and Outlook

6.1. Summary: Two-Center Interferences

In Chapter 3, I showed that I can reliably recover both amplitude and phase information specific to a molecular target in TDDFT simulations of HHS, in order to characterize the two-center interference (TCI) minima in three molecules within the carbon dichalcogen family [110]. This TCI is characterized by a minimum in the spectral intensity and a π phase jump, both of which were recovered using this methodology. To do so, I have combined resolving the total dipole signal into contributions from individual Kohn-Sham orbitals with careful signal processing and normalization. I compared generic strategies on how to select a single set of short trajectories either through the simulation-box absorbing boundary conditions or with an APT-ionization seed [143], together with a well-timed short-window time filtering, in order to compare my results directly with experiment [165, 171, 179]. I also discussed field-induced effects that can be unique to a specific target, such as the reshaping of the TCI feature induced by the APT in CO_2 that is absent in the other carbon dichalcogens. Also, in conjunction with the experiments performed at The Ohio State University, I further studied the wavelength and intensity dependence of the TCI minimum in CO_2 [179], and determined that multi-orbital effects were to blame for the deviation from the expected results for wavelengths less than 1200 nm. Finally, I introduced a method to numerically approximate the field-free scattering-dipole matrix elements through coherent scattering simulations. These field-free scattering simulations showed an excellent agreement when compared to the full TDDFT HHS results [110].

More generally, the idea of working with the Kohn-Sham-orbital-resolved dipole signal, as proposed in Sec. 2.2.3.3 and first tested in Chapter 3, is a powerful tool for practitioners of TDDFT, like myself. Though the Kohn-Sham (KS) orbitals are not physical quantities *per se* [108, 109], their usefulness (particularly with respect to the correct shape/symmetry of the wavefunction) is starting to become more widely-recognized within the community [111, 112, 156, 157]. Even when using an LDA exchange-correlation functional, one can make quantitative comparisons between high-harmonic spectra from different molecules by simply correcting for the incorrect ionization potentials of the computed KS orbitals [146]. Furthermore, the ability to decompose and correct the dipole signal from individual KS orbitals will be even more important when performing high-harmonic spectroscopy on larger molecules, or on molecules in the condensed phase.

6.2. Summary: High-Harmonic Sideband Spectroscopy

In Chapter 4, I showed that periodic, particle-like CM dynamics initiated in bromobutadiyne (BrC_4H) leads to a coherent time-dependent modulation of a wavelength-dependent HHG probe, reflecting the sensitivity of the HHG process to the local charge density [66]. In the spectral domain and over several laser cycles, the CM dynamics manifests as sidebands whose energies correspond to the sum and the difference frequencies between the driving laser and the CM. These sidebands constitute a background-free probe of the CM motion from which one can unambiguously extract the migration frequencies by scanning the laser wavelength. Interestingly, a localized, particle-like CM motion in BrC_4H is characterized by multiple sidebands, associated with ω_{CM} and $2\omega_{\mathrm{CM}}$, which each give a measurement of the CM frequency which is consistent with the value obtained directly

from the time-dependent dynamics. I also explored the experimental viability of these results, by investigating the effect of a distribution of molecular alignments, of having only a fraction of the molecules undergoing CM, and of a finite CM lifetime.

6.3. Summary: Frequency-Matched Strobo-Spectroscopy

In Chapter 5, I showed that frequency-matched high-harmonic strobo-spectroscopy of charge migration (CM+FMSS) in BrC_4H causes a coherent modulation of the HHG signal that precisely tracks the amount of electron density on the bromine atom, which provides information about the phase of the CM motion. By exploiting a site-specific feature of the HHG spectrum, I achieve a time- and space-resolved analysis of the CM by performing a sub-cycle-resolved delay scan [69]. FMSS takes advantage of the intrinsic attosecond time resolution of the HHG process (the attochirp), in which different harmonics are emitted at different times and thus probe different locations of the electron hole. These claims are supported by a similar result from an SFA-inspired model calculation. I can also make a direct comparison between the recombination-time-dependent, harmonic-frequency-integrated HHG yield and the hole density on the halogen. Lastly, I briefly explored the effect of the laser field on the CM dynamics (the CM drift), and connected those results to what I learned from nonlinear dynamics [18].

When combined with my previous results, outlined in the previous section, I get a full picture of how one could measure CM using high-harmonic spectroscopy:

1. Choose the target molecule wisely. A conjugated system of π bonds (alkenes and alkynes) acts as a "highway" for the electron density to travel along, and a heavy halogen on one end of the molecule provides a site for localized ionization [35, 39].

2. Initiate CM dynamics in the target sample via a localized ionization – see also Section 6.4. According to nonlinear dynamics, the characteristics of the created CM mode should be robust with respect to the specifics of the ionization event [18].

3. Apply a laser field polarized perpendicular to the molecular backbone. The time-dependent beat between the periods of the CM dynamics and the laser causes sidebands to appear in the resulting high-harmonic spectrum. By varying the wavelength of the applied laser field, one can precisely determine the fundamental CM frequency [66].

4. Tune the laser wavelength so that it is resonant with the CM dynamics ($\omega_L = \omega_{\mathrm{CM}}/2$). Then, by scanning the delay between the pump pulse that induces CM and the (still perpendicularly-polarized) few-cycle laser pulse, one can exploit a site-specific feature in the harmonic spectrum to track the time-dependent location of the electron hole [69].

While the procedure outlined above would likely need to adapt to each individual experimental setup, I have endeavoured to make sure that each of the above steps is both robust and generalizable. I hope that in the future, some or all of these techniques are used to realize an experimental measurement of CM using high-harmonic spectroscopy.

6.4. Outlook: Initiating CM with Ultrashort Laser Pulses

In the past, theoretical studies of charge migration have often created the initial condition for ultrafast electron dynamics by simply removing an electron from one (or more) molecular orbitals – see Refs. [25, 36, 37, 41], among many others. More recently, however, there has been some effort put towards accurately modeling the ionization of a molecule via an ultrashort laser pulse [10, 33, 221, 236]. Many CM experiments take place at free-electron lasers (FELs) [235, 237–239], which promise ultrashort (few hundreds of attoseconds) laser pulses with high photon energies (few tens of electron-volts). When looking at CM in larger molecules, these laser pulses can communicate with dozens of molecular orbitals, leading to incredibly complicated CM dynamics. Theoretical models for these types of CM experiments involve computing the frequency-dependent photoionization cross section of all of the relevant molecular orbitals in order to determine what

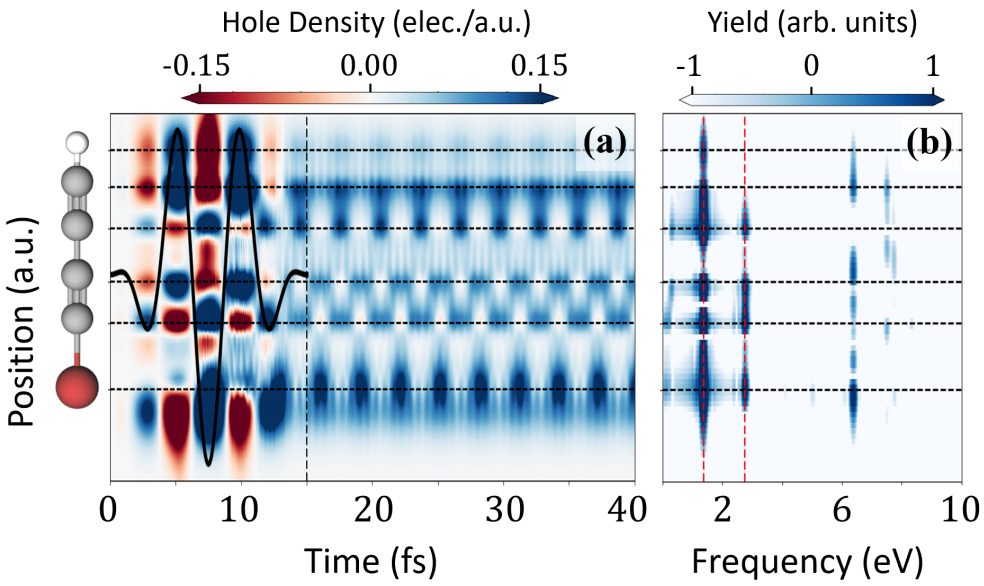

Figure 6.1: (a) Time-dependent hole density $\rho_H(z,t)$ along the molecular backbone of BrC_4H during and after a 1500 nm, 1 o.c. FWHM (3 o.c. total) laser pulse, parallel to the molecular axis. Solid black curve denotes the applied laser field; after the black vertical dashed line, the field is zero. (b) Position-dependent Fourier spectrum of the field-free (after the laser pulse has ended) CM dynamics in panel (a). Red vertical dashed lines indicate the fundamental CM frequency ω_{CM} and its second harmonic $2\omega_{\mathrm{CM}}$.

the initial condition for CM looks like, while also factoring in the frequency profile of the applied laser pulse – for an example using the amino acid tryptophan, see Ref. [221].

As discussed in Sec. 4.2, I have instead opted to use constrained DFT to create the localized initial condition needed to induce CM dynamics. By doing so, I have learned a lot about the fundamentals of CM [18, 35, 39]; however, the most pressing question is how particle-like CM dynamics can be created in a laboratory setting. This is the question I start to grapple with in this section; while these results are preliminary, they are promising enough to include here.

I apply a few-cycle, strong MIR laser pulse *parallel* to the backbone of a BrC_4H molecule. For a wavelength of 1500 nm, an intensity of 50 TW/cm^2, and a total pulse duration of 3 optical cycles, the resulting dynamics is presented in Figure 6.1. In panel (a),

I show the time-dependent hole density $\rho_H(z,t)$ along the molecular backbone, defined in Eq. 4.4, during and after the applied laser pulse. During the laser pulse ($0 \leq t \leq 15\,\text{fs}$), polarization effects heavily dominate; after the pulse, however, there is a clear back-and-forth motion of a localized electron hole moving from one end of the molecule to the other end, with a well-defined CM frequency. This particle-like CM dynamics is stable (in the absence of nuclear motion, at least) for another 30 femtoseconds. The corresponding position-dependent Fourier spectrum of the field-free (after the laser pulse has ended) CM dynamics is shown in Fig. 6.1(b). As expected for a particle-like CM motion in BrC_4H, we see a strong feature at $\omega_{\text{CM}} \approx 1.5\,\text{eV}$, as well as a weaker $2\omega_{\text{CM}} \approx 3\,\text{eV}$ feature that is found primarily on the middle C $\equiv$ C bond. In addition, there are high-frequency oscillations of the electron density, seen in (b) near 6.5 eV, that I believe are caused by the beating between two or more molecular orbitals (similar to Cederbaum's original theory [25]).

Figure 6.1 shows that tunnel ionization from a 1500 nm, few-cycle laser pulse polarized parallel to the backbone of a BrC_4H molecule can induce a periodic CM motion along the molecular axis. Furthermore, early investigations of the robustness of this CM mode with respect to various laser parameters (wavelength, carrier-envelope phase, intensity, etc.) are very encouraging [213]. A robust method for initiating a particle-like mode of CM would be a big step forward in the field, and another milestone towards the experimental measurement of particle-like CM.

Appendix A. Angle-Dependent TCI in CO_2 (Octopus 8.4)

```
CalculationMode = td # gs if ground-state, td if time-dependent


TheoryLevel = dft

SICCorrection = sic_adsic

ParStates = no


# convergence parameters for ground state

ConvRelEv = 1E-10

ConvRelDens = 1E-15

MaximumIter = -1


################################################################################

# !! GROUND STATE PARAMETERS !!

################################################################################

FromScratch = yes

BoxShape = parallelepiped

Spacing = 0.300 # in atomic length units


%Lsize # in atomic length units

  70.0 | 35.0 | 30.0

%
```

```
theta_deg=00 # <-- Scan Parameter


AbsorbingBoundaries = cap

ABWidth = 15.0 # in atomic length units

ABCapHeight = -1.00 # in atomic units


Output = wfs_sqmod

OutputFormat = integrate_yz + integrate_xz

OutputInterval = 5

################################################################################


%Species

  'O' | species_pseudo | file | './O.psf' | lmax | 1 | lloc | 1

  'C' | species_pseudo | file | './C.psf' | lmax | 1 | lloc | 1

%


theta_rad = theta_deg*pi/180

%Coordinates

  'O' | -2.1966*cos(theta_rad) | -2.1966*sin(theta_rad) | 0.0 | no

  'C' |  0.0000*cos(theta_rad) |  0.0000*sin(theta_rad) | 0.0 | no

  'O' |  2.1966*cos(theta_rad) |  2.1966*sin(theta_rad) | 0.0 | no

%
```

```
################################################################################
# !! TIME-DEPENDENT PARAMETERS TO BE ALTERED !!
################################################################################
delay = 0.06 # in IR optical cycles
lambda = 1500 # in nanometers
I0 = 0.6 # x 10^14 W/cm^2
dt = 0.05 # in atomic time units
n = 9 # must be an odd integer!

TDOutput = laser + dipole_acceleration
################################################################################

F0 = sqrt(I0/351)
F1 = sqrt(0.000*I0/351)
omega = 45.6/lambda
period = 2*pi/omega
tau = 2*period
Ttot = 3*period
Tdel = (delay - 0.25)*period

TDPropagator = aetrs
TDMaxSteps = ceiling(Ttot/dt)
TDTimeStep = dt
```

```
%TDExternalFields
  electric_field | 1 | 0 | 0 | omega | "envelope_sin" | "phase"
  electric_field | 1 | 0 | 0 | n*omega | "envelope" | "phase1"
  electric_field | 1 | 0 | 0 | (n+2)*omega | "envelope" | "phase2"
  electric_field | 1 | 0 | 0 | (n+4)*omega | "envelope" | "phase3"
  electric_field | 1 | 0 | 0 | (n+6)*omega | "envelope" | "phase4"
  electric_field | 1 | 0 | 0 | (n+8)*omega | "envelope" | "phase5"
%


%TDFunctions
  "envelope_sin" | tdf_from_expr | "F0*step(tau-t)*((sin(pi*t/(2*tau)))^2)
        +F0*step(t-tau-0.001)"
  "envelope" | tdf_from_expr | "0.2*F1*step(tau-t)*((sin(pi*t/(2*tau)))^2)
        +0.2*F1*step(t-tau-0.001)"
  "phase" | tdf_cw | -pi/2
  "phase1" | tdf_cw | pi/2 - n*omega*Tdel
  "phase2" | tdf_cw | pi/2 - (n+2)*omega*Tdel
  "phase3" | tdf_cw | pi/2 - (n+4)*omega*Tdel
  "phase4" | tdf_cw | pi/2 - (n+6)*omega*Tdel
  "phase5" | tdf_cw | pi/2 - (n+8)*omega*Tdel
%
```

Appendix B. CM+HHSS in BrC_4H (Octopus 11.4)

```
CalculationMode = td # gs for ground-state, td for time-dependent


TheoryLevel = kohn_sham

SICCorrection = sic_adsic

ExperimentalFeatures = true

ParStates = no

FromScratch = yes

BoxShape = parallelepiped


Spacing = 0.3

%Lsize

  45.0 | 20.0 | 45.0

%


# Comment out for gs, uncomment for td.

AbsorbingBoundaries = cap

ABWidth = 15.0 # in atomic length units

ABCapHeight = -1.00 # in atomic units


%Species

  'H' | species_pseudo | file | './H.psf' | lmax | 1 | lloc | 1

  'C' | species_pseudo | file | './C.psf' | lmax | 1 | lloc | 1
```

```
  'Br' | species_pseudo | file | './Br.hgh' | lmax | 3 | lloc | 1
%

# Geometry for bromobutadiyne.
%Coordinates
  'H' | 0.000000 | 0.000000 | 13.033552 | no
  'C' | -0.004314 | 0.000064 | 11.020957 | no
  'C' | -0.007581 | 0.000113 | 8.753220 | no
  'C' | -0.008477 | 0.000126 | 5.858400 | no
  'C' | -0.006588 | 0.000098 | 3.590760 | no
  'Br' | 0.000000 | 0.000000 | 0.000000 | no
%

%TransformStates # depends on converged ground state
    .
    .
    .
%

%Occupations
  1 | 2 | 2 | 2 | 2 | 2 | 2 | 2 | 2 | 2 | 2 | 2
%
ExcessCharge = 1
```

```
###############################################################################
# !! TIME-DEPENDENT PARAMETERS !!
###############################################################################
lambda = 1344 # laser wavelength
I0 = 0.45 # x 10^14 W/cm^2; laser intensity
tIR=0.0000 # delay between start of CM and laser (should not matter)
###############################################################################


F0 = sqrt(I0/351)
omega = 45.6/lambda
period = 2*pi/omega
tau = 2*period
Tdel = (delay - 0.25)*period
Tstart = tIR * period


# Define laser pulse
%TDExternalFields
  electric_field | 1 | 0 | 0 | omega | "envelope_sin" | "phase"
%


%TDFunctions
  "envelope_sin" | tdf_from_expr | "F0*step(t-Tstart)*step(tau+Tstart-t)
```

```
    *((sin(pi*(t-Tstart)/(2*tau)))^2)+F0*step(t-tau-Tstart-0.001)"
  "phase" | tdf_cw | -pi/2 - omega*Tstart
%

%TDOutput
  dipole_acceleration
  multipoles
  laser
  energy
%

TDPropagator = etrs
TDPropagationTime = ceiling((10.0 + tIR)*period)
TDTimeStep = 0.05
TDEnergyUpdateIter = 1
TDExponentialMethod = lanczos
TDExpOrder = 8

# Output the charge migration dynamics.
%Output
  density | "output_format" | integrate_xy + integrate_xz + integrate_yz |
      "output_interval" | 5
  wfs_sqmod | "output_format" | integrate_xy + integrate_xz + integrate_yz |
```

```
      "output_interval" | 5

%

OutputWfsNumber = "1"
```

Appendix C. CM+FMSS in BrC_4H (Octopus 11.4)

```
CalculationMofde = td # gs for ground-state, td for time-dependent


TheoryLevel = kohn_sham

SICCorrection = sic_adsic

ExperimentalFeatures = true

FromScratch = no

ParStates = no

BoxShape = parallelepiped


Spacing = 0.3

%Lsize

  45.0 | 20.0 | 45.0

%


# Comment out for gs, uncomment for td.

AbsorbingBoundaries = cap

ABWidth = 15.0 # in atomic length units

ABCapHeight = -1.00 # in atomic units


%Species

  'H' | species_pseudo | file | './H.psf' | lmax | 1 | lloc | 1

  'C' | species_pseudo | file | './C.psf' | lmax | 1 | lloc | 1
```

```
  'Br' | species_pseudo | file | './Br.hgh' | lmax | 3 | lloc | 1
%

# Geometry for bromobutadiyne.
%Coordinates
  'H' | 0.000000 | 0.000000 | 13.033552 | no
  'C' | -0.004314 | 0.000064 | 11.020957 | no
  'C' | -0.007581 | 0.000113 | 8.753220 | no
  'C' | -0.008477 | 0.000126 | 5.858400 | no
  'C' | -0.006588 | 0.000098 | 3.590760 | no
  'Br' | 0.000000 | 0.000000 | 0.000000 | no
%

%TransformStates # depends on converged ground state
  .
  .
  .
%

%Occupations
  1 | 2 | 2 | 2 | 2 | 2 | 2 | 2 | 2 | 2 | 2 | 2
%
```

```
ExcessCharge = 1


################################################################################
# !! TIME-DEPENDENT PARAMETERS !!
################################################################################
lambda = 1344 # laser wavelength (frequency-matched)
I0 = 0.45 # x 10^14 W/cm^2; laser intensity
tIR=3.2500 # delay between laser and CM
CEP = 0.0000 # CEP of laser pulse
pulse_width = 5.0000 # width of laser pulse
################################################################################


F0 = sqrt(I0/351)
omega = 45.6/lambda
period = 2*pi/omega
tau = pulse_width * period
Tstart = (tIR * period) - 0.5 * tau


%TDExternalFields
  electric_field | 1 | 0 | 0 | omega | "envelope_sin" | "phase"
%


%TDFunctions
```

```
  "envelope_sin" | tdf_from_expr | "F0*step(tau+Tstart-t)*step(t-Tstart)
    *((sin(pi*(t-Tstart)/(tau)))^2)"
  "phase" | tdf_cw | -((omega * (pi/2 + Tstart + tau/2)) + CEP)
%

%TDOutput
  laser
  dipole_acceleration
  eigenvalues
  multipoles
%

TDPropagator = etrs
TDPropagationTime = ceiling((tIR + 1.5)*period + 0.5*tau)
TDTimeStep = 0.05
TDEnergyUpdateIter = 1
TDExponentialMethod = lanczos
TDExpOrder = 8

# New in Octopus 11: automatically compute orbital-resolved dipole moments.
TDOutputResolveStates = true

# Output the charge migration dynamics.
```

```
%Output
  density | "output_format" | integrate_xy + integrate_xz + integrate_yz
    | "output_interval" | 5
  wfs_sqmod | "output_format" | integrate_xy + integrate_xz + integrate_yz
    | "output_interval" | 5
%
OutputWfsNumber = "1"
```

Published Works

- Kyle A. Hamer et al. "Orbital-Resolved Calculations of Two-Center Interferences in Linear Triatomic Molecules" *Phys. Rev. A* **104**, 033114 (2021) [110]

- Kyle A. Hamer et al. "Characterizing Particle-Like Charge Migration Dynamics with High-Harmonic Sideband Spectroscopy" *Phys. Rev. A* **106**, 013103 (2022) [66]

- Kyle A. Hamer et al. "Frequency-Matched Strobo-Spectroscopy as a Tool for Tracking Particle-Like Charge Migration" *Jour. of Phys. Chem. A* **128.1** (2024) [69]

- Kyle A. Hamer et al. (in preparation, 2024) [213]

- Aderonke S. Folorunso et al. "Molecular Modes of Attosecond Charge Migration" *Phys. Rev. Lett.* **126**, 133002 (2021) [35]

- François Mauger et al. "Charge Migration and Attosecond Solitons in Conjugated Organic Molecules" *Phys. Rev. Res.* **4**, 013073 (2022) [18]

- Daniel R. Tuthill et al. "Investigation of Interferences in Carbon Dioxide through Multidimensional Molecular-Frame High-Harmonic Spectroscopy" *Jour. of Phys. Chem. A* **126.46** (2022) [179]

- Aderonke S. Folorunso et al. "Attochemistry Regulation of Charge Migration" *Jour. of Phys. Chem. A* **127.8** (2023) [39]

- Stephanie N. Armond et al. (in preparation, 2024) [146]

Bibliography

[1] M. F. Kling and M. J. J. Vrakking. "Attosecond Electron Dynamics". In: *Annual Review of Physical Chemistry* 59.1 (2008), pp. 463–492.

[2] A. H. Zewail. "Femtochemistry: Atomic-Scale Dynamics of the Chemical Bond". In: *The Journal of Physical Chemistry A* 104.24 (2000), pp. 5660–5694.

[3] M. Ferray et al. "Multiple-harmonic conversion of 1064 nm radiation in rare gases". In: *Journal of Physics B: Atomic, Molecular and Optical Physics* 21.3 (Feb. 1988), pp. L31–L35.

[4] A. McPherson et al. "Studies of multiphoton production of vacuum-ultraviolet radiation in the rare gases". In: *J. Opt. Soc. Am. B* 4.4 (Apr. 1987), pp. 595–601.

[5] P. M. Paul et al. "Observation of a Train of Attosecond Pulses from High Harmonic Generation". In: *Science* 292.5522 (2001), pp. 1689–1692.

[6] M. Hentschel et al. "Attosecond metrology". In: *Nature* 414.6863 (Nov. 2001), pp. 509–513.

[7] F. Krausz and M. Ivanov. "Attosecond physics". In: *Rev. Mod. Phys.* 81 (1 Feb. 2009), pp. 163–234.

[8] C. Altucci, R. Velotta, and J. P. Marangos. "Ultra-fast dynamic imaging: An overview of current techniques, their capabilities and future prospects". In: *Journal of Modern Optics* 57 (July 2010), pp. 916–952.

[9] F. Lépine, M. Y. Ivanov, and M. J. J. Vrakking. "Attosecond molecular dynamics: fact or fiction?" In: *Nature Photonics* 8.3 (Mar. 2014), pp. 195–204.

[10] A. Palacios and F. Martín. "The quantum chemistry of attosecond molecular science". In: *WIREs Computational Molecular Science* 10.1 (2020).

[11] A. Mak et al. "Attosecond single-cycle undulator light: a review". In: *Reports on Progress in Physics* 82.2 (Jan. 2019), p. 025901.

[12] Swedish Royal Academy of Sciences. "Press Release: The Nobel Prize in Physics 2023".

[13] H. J. Wörner et al. "Charge migration and charge transfer in molecular systems". In: *Structural Dynamics* 4.6 (2017), p. 061508.

[14] F. Calegari et al. "Charge migration induced by attosecond pulses in bio-relevant molecules". In: *Journal of Physics B: Atomic, Molecular and Optical Physics* 49.14 (June 2016), p. 142001.

[15] M. Nisoli et al. "Attosecond Electron Dynamics in Molecules". In: *Chemical Reviews* 117.16 (2017), pp. 10760–10825.

[16] F. Remacle, R. D. Levine, and M. A. Ratner. "Charge directed reactivity: a simple electronic model, exhibiting site selectivity, for the dissociation of ions". In: *Chemical Physics Letters* 285.1 (1998), pp. 25–33.

[17] N. V. Golubev and A. I. Kuleff. "Control of charge migration in molecules by ultrashort laser pulses". In: *Phys. Rev. A* 91 (5 May 2015), p. 051401.

[18] F. Mauger et al. "Charge migration and attosecond solitons in conjugated organic molecules". In: *Phys. Rev. Research* 4 (2022), p. 013073.

[19] W.-D. Yu et al. "Dynamical analysis of attosecond molecular modes". In: *Phys. Rev. A* 107 (1 Jan. 2023), p. 013101.

[20] O. K. Rice and H. C. Ramsperger. "Theories of Unimolecular Gas Reactions at Low Pressures". In: *Journal of the American Chemical Society* 49.7 (1927), pp. 1617–1629.
[21] L. S. Kassel. "Studies in Homogeneous Gas Reactions. I". In: *The Journal of Physical Chemistry* 32.2 (1928).
[22] R. A. Marcus. "Unimolecular Dissociations and Free Radical Recombination Reactions". In: *The Journal of Chemical Physics* 20.3 (1952), pp. 359–364.
[23] F. Remacle and R. D. Levine. "An electronic time scale in chemistry". In: *Proceedings of the National Academy of Sciences* 103.18 (2006), pp. 6793–6798.
[24] R. Weinkauf et al. "Nonstationary Electronic States and Site-Selective Reactivity". In: *The Journal of Physical Chemistry A* 101.42 (1997), pp. 7702–7710.
[25] L. S. Cederbaum and J. Zobeley. "Ultrafast charge migration by electron correlation". In: *Chemical Physics Letters* 307.3 (1999), pp. 205–210.
[26] J. Breidbach and L. S. Cederbaum. "Migration of holes: Formalism, mechanisms, and illustrative applications". In: *The Journal of Chemical Physics* 118.9 (2003), pp. 3983–3996.
[27] J. Breidbach and L. S. Cederbaum. "Universal Attosecond Response to the Removal of an Electron". In: *Phys. Rev. Lett.* 94 (3 Jan. 2005), p. 033901.
[28] V. Despré and A. I. Kuleff. "Size effects in charge migration in alkyne chains". In: *Theoretical Chemistry Accounts* 138.9 (Aug. 2019), p. 110.
[29] V. Despré and A. I. Kuleff. "Correlation-driven charge migration as an initial step of the dynamics in correlation bands". In: *Phys. Rev. A* 106 (2 Aug. 2022), p. L021501.
[30] K. Chordiya et al. "Photo-ionization initiated differential ultrafast charge migration: impacts of molecular symmetries and tautomeric forms". In: *Phys. Chem. Chem. Phys.* 25 (6 2023), pp. 4472–4480.
[31] S. van den Wildenberg et al. "Temporal and spatially resolved imaging of the correlated nuclear-electronic dynamics and of the ionized photoelectron in a coherently electronically highly excited vibrating LiH molecule". In: *The Journal of Chemical Physics* 151.13 (2019), p. 134310.
[32] E. Goulielmakis et al. "Real-time observation of valence electron motion". In: *Nature* 466.7307 (Aug. 2010), pp. 739–743.
[33] F. Calegari et al. "Ultrafast electron dynamics in phenylalanine initiated by attosecond pulses". In: *Science* 346.6207 (2014), pp. 336–339.
[34] P. M. Kraus et al. "Measurement and laser control of attosecond charge migration in ionized iodoacetylene". In: *Science* 350.6262 (2015), pp. 790–795.
[35] A. S. Folorunso et al. "Molecular Modes of Attosecond Charge Migration". In: *Phys. Rev. Lett.* 126 (13 Mar. 2021), p. 133002.
[36] H. Hennig, J. Breidbach, and L. S. Cederbaum. "Electron Correlation as the Driving Force for Charge Transfer: Charge Migration Following Ionization in N-Methyl Acetamide". In: *The Journal of Physical Chemistry A* 109.3 (2005), pp. 409–414.
[37] V. Despré, N. V. Golubev, and A. I. Kuleff. "Charge Migration in Propiolic Acid: A Full Quantum Dynamical Study". In: *Phys. Rev. Lett.* 121 (20 Nov. 2018), p. 203002.

[38] Y. Meng et al. “Ultrafast charge migration in ionized iodo-alkyne chain I(CC)nH+”. In: *AIP Advances* 13.4 (2023), p. 045301.

[39] A. S. Folorunso et al. “Attochemistry Regulation of Charge Migration”. In: *The Journal of Physical Chemistry A* 127.8 (2023), pp. 1894–1900.

[40] J. Feist et al. “Probing Electron Correlation via Attosecond xuv Pulses in the Two-Photon Double Ionization of Helium”. In: *Phys. Rev. Lett.* 103 (6 Aug. 2009), p. 063002.

[41] A. I. Kuleff, S. Lünnemann, and L. S. Cederbaum. “Electron-correlation-driven charge migration in oligopeptides”. In: *Chemical Physics* 414 (2013), pp. 100–105.

[42] A. I. Kuleff et al. “Core Ionization Initiates Subfemtosecond Charge Migration in the Valence Shell of Molecules”. In: *Phys. Rev. Lett.* 117 (9 Aug. 2016), p. 093002.

[43] J. I. Fuks et al. “Dynamics of Charge-Transfer Processes with Time-Dependent Density Functional Theory”. In: *The Journal of Physical Chemistry Letters* 4.5 (2013), pp. 735–739.

[44] D. Jia et al. “Quantum control of electronic fluxes during adiabatic attosecond charge migration in degenerate superposition states of benzene”. In: *Chemical Physics* 482 (2017). Electrons and nuclei in motion - correlation and dynamics in molecules (on the occasion of the 70th birthday of Lorenz S. Cederbaum), pp. 146–159.

[45] K. E. Spinlove et al. “Using quantum dynamics simulations to follow the competition between charge migration and charge transfer in polyatomic molecules”. In: *Chemical Physics* 482 (2017). Electrons and nuclei in motion - correlation and dynamics in molecules (on the occasion of the 70th birthday of Lorenz S. Cederbaum), pp. 52–63.

[46] A. Bruner et al. “Attosecond Charge Migration with TDDFT: Accurate Dynamics from a Well-Defined Initial State”. In: *The Journal of Physical Chemistry Letters* 8.17 (2017), pp. 3991–3996.

[47] M. Lara-Astiaso et al. “Role of electron-nuclear coupled dynamics on charge migration induced by attosecond pulses in glycine”. In: *Chemical Physics Letters* 683 (2017). Ahmed Zewail (1946-2016) Commemoration Issue of Chemical Physics Letters, pp. 357–364.

[48] M. Vacher, M. J. Bearpark, and M. A. Robb. “Communication: Oscillating charge migration between lone pairs persists without significant interaction with nuclear motion in the glycine and Gly-Gly-NH-CH3 radical cations”. In: *The Journal of Chemical Physics* 140.20 (2014), p. 201102.

[49] D. Ayuso et al. “Ultrafast charge dynamics in glycine induced by attosecond pulses”. In: *Phys. Chem. Chem. Phys.* 19 (30 2017), pp. 19767–19776.

[50] I. Polyak et al. “Charge migration engineered by localisation: electron-nuclear dynamics in polyenes and glycine”. In: *Molecular Physics* 116.19-20 (2018), pp. 2474–2489.

[51] L. Lehr et al. “Femtosecond Dynamics after Ionization: 2-Phenylethyl-N,N-dimethylamine as a Model System for Nonresonant Downhill Charge Transfer in Peptides”. In: *The Journal of Physical Chemistry A* 109.36 (2005), pp. 8074–8080.

[52] S. Lünnemann, A. I. Kuleff, and L. S. Cederbaum. "Ultrafast charge migration in 2-phenylethyl-N,N-dimethylamine". In: *Chemical Physics Letters* 450.4 (2008), pp. 232–235.

[53] B. Mignolet, R. D. Levine, and F. Remacle. "Charge migration in the bifunctional PENNA cation induced and probed by ultrafast ionization: a dynamical study". In: *Journal of Physics B: Atomic, Molecular and Optical Physics* 47.12 (June 2014), p. 124011.

[54] P. Hoerner, W. Li, and H. B. Schlegel. "Angular Dependence of Strong Field Ionization of 2-Phenylethyl-N,N-dimethylamine (PENNA) Using Time-Dependent Configuration Interaction with an Absorbing Potential". In: *The Journal of Physical Chemistry A* 124.23 (2020), pp. 4777–4781.

[55] E. P. Månsson et al. "Real-time observation of a correlation-driven sub 3 fs charge migration in ionised adenine". In: *Communications Chemistry* 4.1 (May 2021), p. 73.

[56] F. Calegari et al. "Ultrafast Charge Dynamics in an Amino Acid Induced by Attosecond Pulses". In: *IEEE Journal of Selected Topics in Quantum Electronics* 21.5 (2015), pp. 1–12.

[57] E. Perfetto et al. "Ultrafast Charge Migration in XUV Photoexcited Phenylalanine: A First-Principles Study Based on Real-Time Nonequilibrium Green's Functions". In: *The Journal of Physical Chemistry Letters* 9.6 (2018), pp. 1353–1358.

[58] M. Boggio-Pasqua, M. J. Bearpark, and M. A. Robb. "Toward a Mechanistic Understanding of the Photochromism of Dimethyldihydropyrenes". In: *The Journal of Organic Chemistry* 72.12 (2007), pp. 4497–4503.

[59] S. Eberhard, G. Finazzi, and F. A. Wollmann. "The Dynamics of Photosynthesis." In: *Annu. Rev. Genet.* 42 (2008), pp. 463–515.

[60] G. Leo et al. "Ultraviolet laser-induced cross-linking in peptides". In: *Rapid Communications in Mass Spectrometry* 27.14 (2013), pp. 1660–1668.

[61] T. Barillot et al. "Correlation-Driven Transient Hole Dynamics Resolved in Space and Time in the Isopropanol Molecule". In: *Phys. Rev. X* 11 (3 Sept. 2021), p. 031048.

[62] S. Haessler, J. Caillat, and P. Salières. "Self-probing of molecules with high harmonic generation". In: *Journal of Physics B: Atomic, Molecular and Optical Physics* 44.20 (Sept. 2011), p. 203001.

[63] J. P. Marangos. "Development of high harmonic generation spectroscopy of organic molecules and biomolecules". In: *Journal of Physics B: Atomic, Molecular and Optical Physics* 49.13 (May 2016), p. 132001.

[64] P. M. Kraus and H. J. Wörner. "Perspectives of Attosecond Spectroscopy for the Understanding of Fundamental Electron Correlations". In: *Angewandte Chemie International Edition* 57.19 (2018), pp. 5228–5247.

[65] J. Leeuwenburgh et al. "High-Order Harmonic Generation Spectroscopy of Correlation-Driven Electron Hole Dynamics". In: *Phys. Rev. Lett.* 111 (12 Sept. 2013), p. 123002.

[66] K. A. Hamer et al. "Characterizing particle-like charge-migration dynamics with high-order harmonic sideband spectroscopy". In: *Phys. Rev. A* 106 (1 July 2022), p. 013103.

[67] L. He et al. “Filming movies of attosecond charge migration in single molecules with high harmonic spectroscopy”. In: *Nature Communications* 13.1 (Aug. 2022), p. 4595.
[68] H. B. Schlegel, P. Hoerner, and W. Li. “Ionization of HCCI Neutral and Cations by Strong Laser Fields Simulated With Time Dependent Configuration Interaction”. In: *Frontiers in Chemistry* 10 (2022).
[69] K. A. Hamer et al. “Tracking Charge Migration with Frequency-Matched Strobo-Spectroscopy”. In: *The Journal of Physical Chemistry A* 128.1 (2024), pp. 20–27.
[70] K. C. Kulander and B. W. Shore. “Generation of optical harmonics by intense pulses of laser radiation. II. Single-atom spectrum for xenon”. In: *J. Opt. Soc. Am. B* 7.4 (Apr. 1990), pp. 502–508.
[71] J. L. Krause, K. J. Schafer, and K. C. Kulander. “High-order harmonic generation from atoms and ions in the high intensity regime”. In: *Phys. Rev. Lett.* 68 (24 June 1992), pp. 3535–3538.
[72] P. B. Corkum. “Plasma perspective on strong field multiphoton ionization”. In: *Phys. Rev. Lett.* 71 (13 Sept. 1993), pp. 1994–1997.
[73] K. J. Schafer et al. “Above threshold ionization beyond the high harmonic cutoff”. In: *Phys. Rev. Lett.* 70 (11 Mar. 1993), pp. 1599–1602.
[74] M. Lewenstein et al. “Theory of high-harmonic generation by low-frequency laser fields”. In: *Phys. Rev. A* 49 (3 Mar. 1994), pp. 2117–2132.
[75] R. Santra and A. Gordon. “Three-Step Model for High-Harmonic Generation in Many-Electron Systems”. In: *Phys. Rev. Lett.* 96 (7 Feb. 2006), p. 073906.
[76] G. Farkas and C. Tóth. “Proposal for attosecond light pulse generation using laser induced multiple-harmonic conversion processes in rare gases”. In: *Physics Letters A* 168.5 (1992), pp. 447–450.
[77] X. Chu and S.-I. Chu. “Self-interaction-free time-dependent density-functional theory for molecular processes in strong fields: High-order harmonic generation of H_2 in intense laser fields”. In: *Phys. Rev. A* 63 (2 Jan. 2001), p. 023411.
[78] R. Velotta et al. “High-Order Harmonic Generation in Aligned Molecules”. In: *Phys. Rev. Lett.* 87 (18 Oct. 2001), p. 183901.
[79] N. Hay et al. “High-order harmonic generation in laser-aligned molecules”. In: *Phys. Rev. A* 65 (5 Apr. 2002), p. 053805.
[80] R. de Nalda et al. “Role of orbital symmetry in high-order harmonic generation from aligned molecules”. In: *Phys. Rev. A* 69 (3 Mar. 2004), p. 031804.
[81] S. Baker et al. “Probing Proton Dynamics in Molecules on an Attosecond Time Scale”. In: *Science* 312.5772 (2006), pp. 424–427.
[82] X. Zhou et al. “Molecular Recollision Interferometry in High Harmonic Generation”. In: *Phys. Rev. Lett.* 100 (7 Feb. 2008), p. 073902.
[83] J. Itatani et al. “Tomographic imaging of molecular orbitals”. In: *Nature* 432.7019 (Dec. 2004), pp. 867–871.
[84] C. Vozzi et al. “Generalized molecular orbital tomography”. In: *Nature Physics* 7.10 (Oct. 2011), pp. 822–826.
[85] S. Patchkovskii et al. “High Harmonic Generation and Molecular Orbital Tomography in Multielectron Systems: Beyond the Single Active Electron Approximation”. In: *Phys. Rev. Lett.* 97 (12 Sept. 2006), p. 123003.

[86] S. Haessler et al. “Attosecond imaging of molecular electronic wavepackets”. In: *Nature Physics* 6.3 (Mar. 2010), pp. 200–206.
[87] R. M. Lock et al. “Extracting Continuum Electron Dynamics from High Harmonic Emission from Molecules”. In: *Phys. Rev. Lett.* 108 (13 Mar. 2012), p. 133901.
[88] A. Wardlow and D. Dundas. “High-order-harmonic generation in benzene with linearly and circularly polarized laser pulses”. In: *Phys. Rev. A* 93 (2 Feb. 2016), p. 023428.
[89] V. Gruson et al. “Attosecond dynamics through a Fano resonance: Monitoring the birth of a photoelectron”. In: *Science* 354.6313 (2016), pp. 734–738.
[90] T. T. Luu and H. J. Wörner. “Measurement of the Berry curvature of solids using high-harmonic spectroscopy”. In: *Nature Communications* 9.1 (Mar. 2018), p. 916.
[91] M. R. Bionta et al. “Tracking Ultrafast Solid-State Dynamics in VO2 Using High Harmonic Spectroscopy”. In: *The 22nd International Conference on Ultrafast Phenomena 2020*. Optical Society of America, 2020, Th3B.7.
[92] P. Salières et al. “Feynman’s Path-Integral Approach for Intense-Laser-Atom Interactions”. In: *Science* 292.5518 (2001), pp. 902–905.
[93] Z. Chang. *Fundamentals of Attosecond Optics*. 1st ed. CRC Press, 2011.
[94] P. Antoine, A. L’Huillier, and M. Lewenstein. “Attosecond Pulse Trains Using High–Order Harmonics”. In: *Phys. Rev. Lett.* 77 (7 Aug. 1996), pp. 1234–1237.
[95] P. Salières, A. L’Huillier, and M. Lewenstein. “Coherence Control of High-Order Harmonics”. In: *Phys. Rev. Lett.* 74 (19 May 1995), pp. 3776–3779.
[96] P. Balcou et al. “Generalized phase-matching conditions for high harmonics: The role of field-gradient forces”. In: *Phys. Rev. A* 55 (4 Apr. 1997), pp. 3204–3210.
[97] M. B. Gaarde and K. J. Schafer. “Quantum path distributions for high-order harmonics in rare gas atoms”. In: *Phys. Rev. A* 65 (3 Mar. 2002), p. 031406.
[98] Y. Mairesse et al. “Attosecond Synchronization of High-Harmonic Soft X-rays”. In: *Science (New York, N.Y.)* 302 (Dec. 2003), pp. 1540–3.
[99] K. Varjú et al. “Frequency chirp of harmonic and attosecond pulses”. In: *Journal of Modern Optics* 52.2-3 (2005), pp. 379–394.
[100] D. R. Hartree. “The Wave Mechanics of an Atom with a Non-Coulomb Central Field. Part I. Theory and Methods”. In: *Mathematical Proceedings of the Cambridge Philosophical Society* 24.1 (1928), pp. 89–110.
[101] A. Szabo and N. S. Ostlund. *Modern Quantum Chemistry: Introduction to Advanced Electronic Structure Theory*. First. Dover Publications, Inc., 1982.
[102] M. A. L. Marques and E. K. U. Gross. “Time-Dependent Density Functional Theory”. In: *A Primer in Density Functional Theory*. Ed. by C. Fiolhais, F. Nogueira, and M. A. L. Marques. Springer Berlin Heidelberg, 2003, pp. 144–184.
[103] F. Jensen. *Introduction to Computational Chemistry*. Hoboken, NJ, USA: John Wiley & Sons, Inc., 2006.
[104] E. K. U. Gross and N. T. Maitra. “Introduction to TDDFT”. In: *Fundamentals of Time-Dependent Density Functional Theory*. Ed. by Miguel A.L. Marques et al. Berlin, Heidelberg: Springer Berlin Heidelberg, 2012, pp. 53–99.
[105] E. Runge and E. K. U. Gross. “Density-Functional Theory for Time-Dependent Systems”. In: *Phys. Rev. Lett.* 52 (12 Mar. 1984), pp. 997–1000.

[106] C. A. Ullrich and Z. Yang. "A Brief Compendium of Time-Dependent Density Functional Theory". In: *Brazilian Journal of Physics* 44.1 (Feb. 2014), pp. 154–188.
[107] F. Mauger et al. "Hamiltonian formulation and symplectic split-operator schemes for time-dependent density-functional-theory equations of electron dynamics in molecules". In: *Communications in Nonlinear Science and Numerical Simulation* 129 (2024), p. 107685.
[108] P. Hohenberg and W. Kohn. "Inhomogeneous Electron Gas". In: *Phys. Rev.* 136 (3B Nov. 1964), B864–B871.
[109] W. Kohn and L. J. Sham. "Self-Consistent Equations Including Exchange and Correlation Effects". In: *Phys. Rev.* 140 (4A Nov. 1965), A1133–A1138.
[110] K. A. Hamer et al. "Orbital-resolved calculations of two-center interferences in linear triatomic molecules". In: *Phys. Rev. A* 104 (3 Sept. 2021), p. 033114.
[111] E. J. Baerends and O. V. Gritsenko. "A Quantum Chemical View of Density Functional Theory". In: *The Journal of Physical Chemistry A* 101.30 (1997), pp. 5383–5403.
[112] R. Stowasser and R. Hoffmann. "What Do the Kohn-Sham Orbitals and Eigenvalues Mean?" In: *Journal of the American Chemical Society* 121.14 (1999), pp. 3414–3420.
[113] F. Bloch. "Bemerkung zur Elektronentheorie des Ferromagnetismus und der elektrischen Leitfähigkeit". In: *Zeitschrift für Physik* 57.7 (July 1929), pp. 545–555.
[114] P. A. M. Dirac. "Note on Exchange Phenomena in the Thomas Atom". In: *Mathematical Proceedings of the Cambridge Philosophical Society* 26.3 (1930), pp. 376–385.
[115] M. K. Harbola and V. Sahni. "Quantum-Mechanical Interpretation of the Exchange-Correlation Potential of Kohn-Sham Density-Functional Theory". In: *Phys. Rev. Lett.* 62 (5 Jan. 1989), pp. 489–492.
[116] E. Coccia and E. Luppi. "Time-dependent ab initio approaches for high-harmonic generation spectroscopy". In: *Journal of Physics: Condensed Matter* 34.7 (Nov. 2021), p. 073001.
[117] C. Morassut, E. Coccia, and E. Luppi. "Quantitative performance analysis and comparison of optimal-continuum Gaussian basis sets for high-harmonic generation spectra". In: *The Journal of Chemical Physics* 159.12 (Sept. 2023), p. 124108.
[118] X. Andrade et al. "Time-dependent density-functional theory in massively parallel computer architectures: the octopus project". In: *Journal of Physics: Condensed Matter* 24.23 (May 2012), p. 233202.
[119] M. A. L. Marques et al. "octopus: a first-principles tool for excited electron–ion dynamics". In: *Computer Physics Communications* 151.1 (2003), pp. 60–78.
[120] N. Tancogne-Dejean et al. "Octopus, a computational framework for exploring light-driven phenomena and quantum dynamics in extended and finite systems". In: *The Journal of Chemical Physics* 152.12 (2020), p. 124119.
[121] A. G. Pueyo et al. "Propagators for the Time-Dependent Kohn–Sham Equations: Multistep, Runge–Kutta, Exponential Runge–Kutta, and Commutator Free Magnus Methods". In: *Journal of Chemical Theory and Computation* 14.6 (2018), pp. 3040–3052.

[122] L. Lacombe and N. T. Maitra. "Developing new and understanding old approximations in TDDFT". In: *Faraday Discussions* 224 (2020), pp. 382–401.
[123] J. P. Perdew and A. Zunger. "Self-interaction correction to density-functional approximations for many-electron systems". In: *Phys. Rev. B* 23 (10 May 1981), pp. 5048–5079.
[124] K. Yabana and G. F. Bertsch. "Time-dependent local-density approximation in real time". In: *Phys. Rev. B* 54 (7 Aug. 1996), pp. 4484–4487.
[125] M. A. L. Marques, M. J. T. Oliveira, and T. Burnus. "Libxc: A library of exchange and correlation functionals for density functional theory". In: *Computer Physics Communications* 183.10 (2012), pp. 2272–2281.
[126] C. Legrand, E. Suraud, and P.-G. Reinhard. "Comparison of self-interaction-corrections for metal clusters". In: *Journal of Physics B: Atomic, Molecular and Optical Physics* 35.4 (Feb. 2002), pp. 1115–1128.
[127] I. Ciofini, H. Chermette, and C. Adamo. "A mean-field self-interaction correction in density functional theory: implementation and validation for molecules". In: *Chemical Physics Letters* 380.1 (2003), pp. 12–20.
[128] T. Tsuneda and K. Hirao. "Self-interaction corrections in density functional theory". In: *The Journal of Chemical Physics* 140.18 (2014), 18A513.
[129] A. Castro et al. "octopus: a tool for the application of time-dependent density functional theory". In: *physica status solidi (b)* 243.11 (2006), pp. 2465–2488.
[130] X. Andrade et al. "Real-space grids and the Octopus code as tools for the development of new simulation approaches for electronic systems". In: *Phys. Chem. Chem. Phys.* 17 (47 2015), pp. 31371–31396.
[131] X.-M. Tong et al. "Application of norm-conserving pseudopotentials to intense laser-matter interactions". In: *Phys. Rev. A* 92 (4 Oct. 2015), p. 043422.
[132] S. G. Louie, S. Froyen, and M. L. Cohen. "Nonlinear ionic pseudopotentials in spin-density-functional calculations". In: *Phys. Rev. B* 26 (4 Aug. 1982), pp. 1738–1742.
[133] N. Troullier and J. L. Martins. "Efficient pseudopotentials for plane-wave calculations". In: *Phys. Rev. B* 43 (3 Jan. 1991), pp. 1993–2006.
[134] J. M. Soler et al. "The SIESTA method for *ab initio* order-N materials simulation". In: *Journal of Physics: Condensed Matter* 14.11 (Mar. 2002), pp. 2745–2779.
[135] A. Garcıá. *ATOM User Manual*. Version 4.2.0. ICMAB-CSIC. Jan. 2017. 16 pp.
[136] M. J. T. Oliveira and F. Nogueira. "Generating relativistic pseudo-potentials with explicit incorporation of semi-core states using APE, the Atomic Pseudo-potentials Engine". In: *Computer Physics Communications* 178.7 (2008), pp. 524–534.
[137] C. Hartwigsen, S. Goedecker, and J. Hutter. "Relativistic separable dual-space Gaussian pseudopotentials from H to Rn". In: *Phys. Rev. B* 58 (7 Aug. 1998), pp. 3641–3662.
[138] A. Castro, M. A. L. Marques, and A. Rubio. "Propagators for the time-dependent Kohn–Sham equations". In: *The Journal of Chemical Physics* 121.8 (2004), pp. 3425–3433.
[139] J. G. Muga et al. "Complex absorbing potentials". In: *Physics Reports* 395.6 (2004), pp. 357–426.

[140] Y. P. Li et al. "Wavelength dependence of high-harmonic yield from aligned molecules: roles of structure and electron dynamics". In: *Journal of Physics B: Atomic, Molecular and Optical Physics* 49.7 (Mar. 2016), p. 075603.
[141] M. Labeye et al. "Dynamical distortions of structural signatures in molecular high-order harmonic spectroscopy". In: *Phys. Rev. A* 99 (1 Jan. 2019), p. 013412.
[142] M. Bellini et al. "Temporal Coherence of Ultrashort High-Order Harmonic Pulses". In: *Phys. Rev. Lett.* 81 (2 July 1998), pp. 297–300.
[143] K. J. Schafer et al. "Strong Field Quantum Path Control Using Attosecond Pulse Trains". In: *Phys. Rev. Lett.* 92 (2 Jan. 2004), p. 023003.
[144] J. Biegert et al. "Enhancement of High-Order Harmonic Emission Using Attosecond Pulse Trains". In: *Journal of Modern Optics* 53 (Jan. 2006), pp. 87–96.
[145] C. B. Madsen et al. "Effects of orientation and alignment in high-order harmonic generation and above-threshold ionization". In: *Phys. Rev. A* 76 (3 Sept. 2007), p. 035401.
[146] S. N. Armond, M. B. Gaarde, and K. A. Hamer. "Isotropic Harmonic Spectroscopy using TDDFT".
[147] C. W. Murray, N. C. Handy, and G. J. Laming. "Quadrature schemes for integrals of density functional theory". In: *Molecular Physics* 78.4 (1993), pp. 997–1014.
[148] V. I. Lebedev. "Values of the nodes and weights of ninth to seventeenth order gauss-markov quadrature formulae invariant under the octahedron group with inversion". In: *USSR Computational Mathematics and Mathematical Physics* 15.1 (1975), pp. 44–51.
[149] X. G. Wang and T. Carrington. "Using Lebedev Grids, Sine Spherical Harmonics, and Monomer Contracted Basis Functions to Calculate Bending Energy Levels of HF Trimer". In: *Journal of Theoretical and Computational Chemistry* 02.04 (2003), pp. 599–608.
[150] H. J. Wörner et al. "Controlling the Interference of Multiple Molecular Orbitals in High-Harmonic Generation". In: *Phys. Rev. Lett.* 104 (23 June 2010), p. 233904.
[151] B. K. McFarland et al. "High Harmonic Generation from Multiple Orbitals in N_2". In: *Science* 322 (2008), pp. 1232–1235.
[152] K. Kato, S. Minemoto, and H. Sakai. "Suppression of high-order-harmonic intensities observed in aligned CO_2 molecules with 1300-nm and 800-nm pulses". In: *Phys. Rev. A* 84 (2 Aug. 2011), p. 021403.
[153] J. Heslar, D. Telnov, and S.-I. Chu. "High-order-harmonic generation in homonuclear and heteronuclear diatomic molecules: Exploration of multiple orbital contributions". In: *Phys. Rev. A* 83 (4 Apr. 2011), p. 043414.
[154] A. F. Alharbi et al. "Sensitivity of high-order-harmonic generation to aromaticity". In: *Phys. Rev. A* 92 (4 Oct. 2015), p. 041801.
[155] F. Bedurke, T. Klamroth, and P. Saalfrank. "Many-electron dynamics in laser-driven molecules: wavefunction theory vs. density functional theory". In: *Phys. Chem. Chem. Phys.* 23 (24 2021), pp. 13544–13560.
[156] F. Mauger et al. "High-harmonic spectroscopy of transient two-center interference calculated with time-dependent density-functional theory". In: *Structural Dynamics* 6.4 (2019), p. 044101.

[157] A. Etches, M. B. Gaarde, and L. B. Madsen. "Two-center minima in harmonic spectra from aligned polar molecules". In: *Phys. Rev. A* 84 (2 Aug. 2011), p. 023418.
[158] O. Smirnova et al. "High harmonic interferometry of multi-electron dynamics in molecules". In: *Nature* 460.7258 (Aug. 2009), pp. 972–977.
[159] Z. Chen et al. "Quantitative rescattering theory for laser-induced high-energy plateau photoelectron spectra". In: *Phys. Rev. A* 79 (3 Mar. 2009), p. 033409.
[160] V. Lemierre et al. "Calculation of Ionization Potentials of Small Molecules: A Comparative Study of Different Methods". In: *The Journal of Physical Chemistry A* 109.37 (2005), pp. 8348–8355.
[161] O. V. Gritsenko, Ł. M. Mentel, and E. J. Baerends. "On the errors of local density (LDA) and generalized gradient (GGA) approximations to the Kohn-Sham potential and orbital energies". In: *The Journal of Chemical Physics* 144.20 (2016), p. 204114.
[162] M. E. Casida and D. R. Salahub. "Asymptotic correction approach to improving approximate exchange–correlation potentials: Time-dependent density-functional theory calculations of molecular excitation spectra". In: *The Journal of Chemical Physics* 113.20 (Nov. 2000), pp. 8918–8935.
[163] R. van Leeuwen and E. J. Baerends. "Exchange-correlation potential with correct asymptotic behavior". In: *Phys. Rev. A* 49 (4 Apr. 1994), pp. 2421–2431.
[164] M. Lein. "Attosecond Probing of Vibrational Dynamics with High-Harmonic Generation". In: *Phys. Rev. Lett.* 94 (5 Feb. 2005), p. 053004.
[165] T. T. Gorman et al. "Probing the interplay between geometric and electronic-structure features via high-harmonic spectroscopy". In: *The Journal of Chemical Physics* 150.18 (2019), p. 184308.
[166] C. Vozzi et al. "Controlling Two-Center Interference in Molecular High Harmonic Generation". In: *Phys. Rev. Lett.* 95 (15 Oct. 2005), p. 153902.
[167] T. Kanai, S. Minemoto, and H. Sakai. "Quantum interference during high-order harmonic generation from aligned molecules". In: *Nature* 435.7041 (May 2005), pp. 470–474.
[168] Haessler, S. et al. "Measuring the complex recombination dipole of aligned CO2 molecules in high-order harmonic generation". In: *UVX - Colloque sur les Sources Cohérentes et Incohérentes UV, VUV et X : Applications et développements récents* (2009), pp. 65–70.
[169] E. P. Fowe and A. D. Bandrauk. "Nonlinear time-dependent density-functional-theory study of ionization and harmonic generation in CO_2 by ultrashort intense laser pulses: Orientational effects". In: *Phys. Rev. A* 81 (2 Feb. 2010), p. 023411.
[170] P. V. Abanador. "Theoretical Studies of Ultrafast Electron Dynamics in Atoms and Molecules via High-Order Harmonic Generation". PhD thesis. Louisiana State University, 2018.
[171] D. R. Tuthill et al. "Multidimensional molecular high-harmonic spectroscopy: A road map for charge migration studies". In: *Journal of Molecular Spectroscopy* 372 (2020), p. 111353.
[172] S. De et al. "Field-Free Orientation of CO Molecules by Femtosecond Two-Color Laser Fields". In: *Phys. Rev. Lett.* 103 (15 Oct. 2009), p. 153002.

[173] K. N. Egodapitiya, S. Li, and R. R. Jones. "Terahertz-Induced Field-Free Orientation of Rotationally Excited Molecules". In: *Phys. Rev. Lett.* 112 (10 Mar. 2014), p. 103002.

[174] P. M. Kraus, D. Baykusheva, and H. J. Wörner. "Two-pulse orientation dynamics and high-harmonic spectroscopy of strongly-oriented molecules". In: *Journal of Physics B: Atomic, Molecular and Optical Physics* 47.12 (June 2014), p. 124030.

[175] J. Vos et al. "Orientation-dependent stereo Wigner time delay and electron localization in a small molecule". In: *Science* 360.6395 (2018), pp. 1326–1330.

[176] A. Sissay et al. "Angle-dependent strong-field molecular ionization rates with tuned range-separated time-dependent density functional theory". In: *The Journal of Chemical Physics* 145.9 (2016), p. 094105.

[177] P. Sándor et al. "Angle dependence of strong-field single and double ionization of carbonyl sulfide". In: *Phys. Rev. A* 98 (4 Oct. 2018), p. 043425.

[178] W. Boutu et al. "Coherent control of attosecond emission from aligned molecules". In: *Nature Physics* 4.7 (July 2008), pp. 545–549.

[179] D. R. Tuthill et al. "Investigation of Interferences in Carbon Dioxide through Multidimensional Molecular-Frame High-Harmonic Spectroscopy". In: *The Journal of Physical Chemistry A* 126.46 (2022), pp. 8588–8595.

[180] D. C. Frost, S. T. Lee, and C. A. McDowell. "Photoelectron spectra of OCSe, SCSe, and CSe2". In: *The Journal of Chemical Physics* 59.10 (1973), pp. 5484–5493.

[181] M. V. Frolov et al. "Analytic formulae for high harmonic generation". In: *Journal of Physics B: Atomic, Molecular and Optical Physics* 42.3 (Jan. 2009), p. 035601.

[182] C.-D. Lin et al. "Strong-field rescattering physics—self-imaging of a molecule by its own electrons". In: *Journal of Physics B: Atomic, Molecular and Optical Physics* 43.12 (June 2010), p. 122001.

[183] H. Akagi et al. "Laser Tunnel Ionization from Multiple Orbitals in HCl". In: *Science* 325.5946 (2009), pp. 1364–1367.

[184] X. Zhu et al. "Two-center interference in high-order harmonic generation from heteronuclear diatomic molecules". In: *Optics express* 19 (Jan. 2011), pp. 436–47.

[185] X. Chu and P. J. Memoli. "Role of multiphoton excitation and two-electron effects in high harmonic generation of H_2: A TDDFT calculation". In: *Chemical Physics* 391.1 (2011), pp. 83–87.

[186] A. Rupenyan et al. "Quantum interference and multielectron effects in high-harmonic spectra of polar molecules". In: *Phys. Rev. A* 87 (3 Mar. 2013), p. 031401.

[187] Z. Shu et al. "Channel Coupling Dynamics of Deep-Lying Orbitals in Molecular High-Harmonic Generation". In: *Phys. Rev. Lett.* 128 (18 May 2022), p. 183202.

[188] T. D. Scarborough et al. "Full Characterization of a Molecular Cooper Minimum Using High-Harmonic Spectroscopy". In: *Applied Sciences* 8.7 (2018).

[189] D. J. Tannor. *Introduction to quantum mechanics: a time-dependent perspective.* chapter 17. Sausalito, CA: University Science Books, 2007.

[190] A. D. Dutoi, M. Wormit, and L. S. Cederbaum. "Ultrafast charge separation driven by differential particle and hole mobilities". In: *The Journal of Chemical Physics* 134.2 (2011), p. 024303.

[191] V. Despré and A. I. Kuleff. *Correlation-Driven Charge Migration as Initial Step in the Dynamics in Correlation Bands*. 2021.
[192] D. C. Yost, Y. Yao, and Y. Kanai. "Propagation of maximally localized Wannier functions in real-time TDDFT". In: *The Journal of Chemical Physics* 150.19 (2019), p. 194113.
[193] M. Valiev et al. "NWChem: A comprehensive and scalable open-source solution for large scale molecular simulations". In: *Computer Physics Communications* 181.9 (2010), pp. 1477–1489.
[194] K. Lopata and N. Govind. "Modeling Fast Electron Dynamics with Real-Time Time-Dependent Density Functional Theory: Application to Small Molecules and Chromophores". In: *Journal of Chemical Theory and Computation* 7.5 (2011), pp. 1344–1355.
[195] E. Aprà et al. "NWChem: Past, present, and future". In: *The Journal of Chemical Physics* 152.18 (2020), p. 184102.
[196] A. J. Lichtenberg and M. A. Lieberman. *Regular and Chaotic Dynamics*. Applied Mathematical Sciences. Springer New York, 1992.
[197] J. Masoliver and A. Ros. "Integrability and chaos: the classical uncertainty". In: *European Journal of Physics* 32.2 (Jan. 2011), pp. 431–458.
[198] J. Laskar. "Frequency analysis for multi-dimensional systems. Global dynamics and diffusion". In: *Physica D: Nonlinear Phenomena* 67.1 (1993), pp. 257–281.
[199] W. P. Su, J. R. Schrieffer, and A. J. Heeger. "Solitons in Polyacetylene". In: *Phys. Rev. Lett.* 42 (25 June 1979), pp. 1698–1701.
[200] P. Krause and H. B. Schlegel. "Strong-field ionization rates of linear polyenes simulated with time-dependent configuration interaction with an absorbing potential". In: *The Journal of Chemical Physics* 141.17 (2014), p. 174104.
[201] P. Hoerner and H. B. Schlegel. "Angular Dependence of Strong Field Ionization of CH3X (X = F, Cl, Br, or I) Using Time-Dependent Configuration Interaction with an Absorbing Potential". In: *The Journal of Physical Chemistry A* 121.31 (2017), pp. 5940–5946.
[202] P. Hoerner and H. B. Schlegel. "Angular Dependence of Strong Field Ionization of Haloacetylenes HCCX (X = F, Cl, Br, I), Using Time-Dependent Configuration Interaction with an Absorbing Potential". In: *The Journal of Physical Chemistry C* 122.25 (2018), pp. 13751–13757.
[203] P. Sándor et al. "Angle-dependent strong-field ionization of halomethanes". In: *The Journal of Chemical Physics* 151.19 (2019), p. 194308.
[204] F. Keller and H. Lefebvre-Brion. "Shape resonances in photoionization of diatomic molecules: An example in the *d* inner shell ionization of the hydrogen halides". In: *Zeitschrift für Physik D Atoms, Molecules and Clusters* 4.1 (Mar. 1986), pp. 15–23.
[205] K. Schnorr et al. "Electron Rearrangement Dynamics in Dissociating I_2^{n+} Molecules Accessed by Extreme Ultraviolet Pump-Probe Experiments". In: *Phys. Rev. Lett.* 113 (7 Aug. 2014), p. 073001.
[206] R. Boll et al. "Charge transfer in dissociating iodomethane and fluoromethane molecules ionized by intense femtosecond X-ray pulses". In: *Structural Dynamics* 3.4 (2016), p. 043207.

[207] G. Sansone et al. “Electron localization following attosecond molecular photoionization”. In: *Nature* 465.7299 (June 2010), pp. 763–766.
[208] N. T. Maitra and D. G. Tempel. “Long-range excitations in time-dependent density functional theory”. In: *The Journal of Chemical Physics* 125.18 (2006), p. 184111.
[209] K. J. H. Giesbertz and E. J. Baerends. “Failure of time-dependent density functional theory for excited state surfaces in case of homolytic bond dissociation”. In: *Chemical Physics Letters* 461.4 (2008), pp. 338–342.
[210] S. Raghunathan and M. Nest. “Limits of the Creation of Electronic Wave Packets Using Time-Dependent Density Functional Theory”. In: *The Journal of Physical Chemistry A* 116.33 (2012), pp. 8490–8493.
[211] M. R. Provorse, B. F. Habenicht, and C. M. Isborn. “Peak-Shifting in Real-Time Time-Dependent Density Functional Theory”. In: *Journal of Chemical Theory and Computation* 11.10 (2015), pp. 4791–4802.
[212] J. I. Fuks et al. “Time-Resolved Spectroscopy in Time-Dependent Density Functional Theory: An Exact Condition”. In: *Phys. Rev. Lett.* 114 (18 May 2015), p. 183002.
[213] K. A. Hamer, M. B. Gaarde, and F. Mauger. “Initiation of CM Dynamics using Few-Femtosecond Laser Pulses”.
[214] B. Kaduk, T. Kowalczyk, and T. van Voorhis. “Constrained Density Functional Theory”. In: *Chemical Reviews* 112.1 (2012), pp. 321–370.
[215] N. A. Besley, A. T. B. Gilbert, and P. M. W. Gill. “Self-consistent-field calculations of core excited states”. In: *The Journal of Chemical Physics* 130.12 (2009), p. 124308.
[216] Yu. Liang et al. “Accurate X-Ray Spectral Predictions: An Advanced Self-Consistent-Field Approach Inspired by Many-Body Perturbation Theory”. In: *Phys. Rev. Lett.* 118 (9 Mar. 2017), p. 096402.
[217] P. Ramos and M. Pavanello. “Low-lying excited states by constrained DFT”. In: *The Journal of Chemical Physics* 148.14 (2018), p. 144103.
[218] H. Eshuis and T. van Voorhis. “The influence of initial conditions on charge transfer dynamics”. In: *Phys. Chem. Chem. Phys.* 11 (44 2009), pp. 10293–10298.
[219] A. D. Bandrauk, S. Chelkowski, and H. S. Nguyen. “Attosecond localization of electrons in molecules”. In: *International Journal of Quantum Chemistry* 100.6 (2004), pp. 834–844.
[220] P. M. Kraus et al. “High-Harmonic Probing of Electronic Coherence in Dynamically Aligned Molecules”. In: *Phys. Rev. Lett.* 111 (24 Dec. 2013), p. 243005.
[221] M. Lara-Astiaso et al. “Attosecond Pump–Probe Spectroscopy of Charge Dynamics in Tryptophan”. In: *The Journal of Physical Chemistry Letters* 9.16 (2018), pp. 4570–4577.
[222] Y. Kobayashi, D. M. Neumark, and S. R. Leone. “Theoretical analysis of the role of complex transition dipole phase in XUV transient-absorption probing of charge migration”. In: *Opt. Express* 30.4 (Feb. 2022), pp. 5673–5682.
[223] S. Li et al. “Attosecond coherent electron motion in Auger-Meitner decay”. In: *Science* 375.6578 (2022), pp. 285–290.

[224] D. T. Matselyukh et al. "Decoherence and revival in attosecond charge migration driven by non-adiabatic dynamics". In: *Nature Physics* 18.10 (Oct. 2022), pp. 1206–1213.
[225] H. Yong et al. "Attosecond Charge Migration in Molecules Imaged by Combined X-ray and Electron Diffraction". In: *Journal of the American Chemical Society* 144.45 (2022), pp. 20710–20716.
[226] J. Zhao et al. "Real-Time Observation of Electron-Hole Coherence Induced by Strong-Field Ionization". In: *Chinese Physics Letters* 39.12 (2022), p. 123201.
[227] W. Cheney and D. Kincaid. *Linear Algebra: Theory and Applications*. Jones & Bartlett Learning Inte. Jones & Bartlett Learning, 2012.
[228] J. MacQueen. "Some methods for classification and analysis of multivariate observations". In: *Proc. of the Fifth Berkeley Symposium on Math. Stat and Prob.* Vol. 1. The Regents of the University of California, 1967, pp. 281–297.
[229] N. Dudovich et al. "Measuring and controlling the birth of attosecond XUV pulses". In: *Nature Physics* 2.11 (Nov. 2006), pp. 781–786.
[230] D. Azoury et al. "Self-probing spectroscopy of XUV photo-ionization dynamics in atoms subjected to a strong-field environment". In: *Nature Communications* 8.1 (Nov. 2017), p. 1453.
[231] L. He et al. "Attosecond probing and control of charge migration in carbon-chain molecule". In: *Advanced Photonics* 5.5 (2023), p. 056001.
[232] H. Niikura, D. M. Villeneuve, and P. B. Corkum. "Mapping Attosecond Electron Wave Packet Motion". In: *Phys. Rev. Lett.* 94 (8 Mar. 2005), p. 083003.
[233] A. I. Kuleff and L. S. Cederbaum. "Radiation Generated by the Ultrafast Migration of a Positive Charge Following the Ionization of a Molecular System". In: *Phys. Rev. Lett.* 106 (5 Jan. 2011), p. 053001.
[234] B. Kaufman et al. "Long-Lived Electronic Coherences in Molecules". In: *Phys. Rev. Lett.* 131 (26 Dec. 2023), p. 263202.
[235] G. Grell et al. "Effect of the shot-to-shot variation on charge migration induced by sub-fs x-ray free-electron laser pulses". In: *Phys. Rev. Res.* 5 (2 May 2023), p. 023092.
[236] K. Chordiya et al. "Distinctive onset of electron correlation in molecular tautomers". In: *Phys. Rev. A* 105 (6 June 2022), p. 062808.
[237] J. T. O'Neal and P. Bucksbaum. *Tracking Charge Migration with Attosecond X-Ray Pulses from a Free-Electron Laser*. Stanford University, 2022.
[238] N. Huang et al. "Features and futures of X-ray free-electron lasers". In: *The Innovation* 2.2 (2021).
[239] K. Nagaya et al. "Femtosecond charge and molecular dynamics of I-containing organic molecules induced by intense X-ray free-electron laser pulses". In: *Faraday Discuss.* 194 (0 2016), pp. 537–562.

Vita

Kyle Alexander Hamer, born in Lafayette, Louisiana, has always been fascinated by physics. After receiving his bachelor's degree in physics at Louisiana State University, he felt that there were still stones left unturned, and potential left untapped. So, he decided to pursue a doctorate at LSU. He now has an anticipated graduation date of May 2024, after which he will continue to pursue research in academia.